ISSN Print: 2518-4245
ISSN Online: 2518-4253
Vol. 62(1), March 2025

PROCEEDINGS
OF THE PAKISTAN ACADEMY OF SCIENCES:
A. Physical and Computational Sciences

PAKISTAN ACADEMY OF SCIENCES
ISLAMABAD, PAKISTAN

Proceedings of the Pakistan Academy of Sciences: Part A Physical and Computational Sciences

President: Kauser Abdullah Malik
Secretary General: M. Aslam Baig
Treasurer: Saleem Asghar

Proceedings of the Pakistan Academy of Sciences A. Physical and Computational Sciences is the official flagship, the peer-reviewed quarterly journal of the Pakistan Academy of Sciences. This open-access journal publishes original research articles and reviews on current advances in the field of Computer Science (all), Materials Science (all), Physics and Astronomy (all), Engineering Sciences (all), Chemistry, Statistics, Mathematics, Geography, Geology in English. Authors are not required to be Fellows or Members of the Pakistan Academy of Sciences or citizens of Pakistan. The journal is covered by Print and Online ISSN, indexed in Scopus, and distributed to scientific organizations, institutes and universities throughout the country, by subscription and on an exchange basis.

Editor-in-Chief:

M. Javed Akhtar, Pakistan Academy of Sciences, Islamabad, Pakistan; editor@paspk.org

Managing Editor:

Ali Ahsan, Pakistan Academy of Sciences, Islamabad, Pakistan; editor@paspk.org

Discipline Editors:

Chemical Sciences: Guo-Xin Jin, Inorganic Chemistry Institute, Fudan University, Shanghai, China
Chemical Sciences: Haq Nawaz Bhatti, Department of Chemistry University of Agriculture, Faisalabad, Pakistan
Geology: Peng Cui, Key Laboratory for Mountain Hazards and Earth Surface Process, CAS, Institute of Mountain Hazards & Environment, CAS Chengdu, Sichuan, People's Republic of China
Computer Sciences: Sharifullah Khan, Faculty of Electrical, Computer, IT & Design(FECID), Pak-Austria Fachhochschule: Institute of Applied Sciences and Technology (PAF-IAST), Mange, Haripur, Pakistan
Engineering Sciences: Akhlesh Lakhtakia, Evan Pugh University Professor and The Charles G. Binder (Endowed), Engineering Science and Mechanics, Pennsylvania State University, University Park, USA
Mathematical Sciences: Ismat Beg, Department of Mathematics and Statistical Sciences, Lahore School of Economics, Lahore, Pakistan
Mathematical Sciences: Jinde Cao, Department of Mathematics, Southeast University Nanjing, P. R. China
Physical Sciences: Asghari Maqsood, Department of Physics, E-9, PAF Complex Air University, Islamabad
Physical Sciences: Niemela J. Joseph, The Abdus Salam International Center for Theoretical Physics (ICTP-UNESCO), Trieste- Italy

Editorial Advisory Board:

Saeid Abbasbandy, Department of Mathematics, Imam Khomeini International University Ghazvin, 34149-16818, Iran
Muazzam Ali Khan Khattak, Department of Computer Science, Quaid-i-Azam University, Islamabad, Pakistan
Muhammad Sharif, Department of Mathematics, University of the Punjab, Lahore, Pakistan
Faiz Ullah Shah, Department of Civil, Environmental and Natural Resources Engineering, Lulea University of Technology, Luleå, Sweden
Kashif Nisar, Lecturer of Computer Science, School of Arts and Sciences, The University of Notre Dame, Australia
Guoqian Chen, Laboratory of Systems Ecology and Sustainability Science, College of Engineering, Peking University, Beijing, China
Bhagwan Das, Department of Electronic Engineering, Quaid-e-Awam University of Engineering, Science and Technology Nawabshah, Sindh, Pakistan
Muhammad Sadiq Ali Khan, Department of Computer Science, University of Karachi, Pakistan

Annual Subscription: **Pakistan:** Institutions, Rupees 8000/-; Individuals, Rupees 4000/- (Delivery Charges: Rupees 300/-)
Other Countries: US$ 200.00 (includes air-lifted overseas delivery)

© *Pakistan Academy of Sciences.* Reproduction of paper abstracts is permitted provided the source is acknowledged. Permission to reproduce any other material may be obtained in writing from the Editor.
The data and opinions published in the *Proceedings* are of the author(s) only. The *Pakistan Academy of Sciences* and the *Editors* accept no responsibility whatsoever in this regard.

HEC Recognized; Scopus Indexed

Published by **Pakistan Academy of Sciences**, 3 Constitution Avenue, G-5/2, Islamabad, Pakistan
Email: editor@paspk.org; **Tel:** 92-51-920 7140 & 921 5478; **Websites:** www.paspk.org/proceedings/; www.ppaspk.org

Printed at **Graphics Point.,** Office 3-A, Wasal Plaza, Fazal-e-Haq Road Blue Area Islamabad.
Ph: 051-2806257, **E-mail:** graphicspoint16@gmail.com

PROCEEDINGS OF THE
PAKISTAN ACADEMY OF SCIENCES: PART A
Physical and Computational Sciences

CONTENTS

Volume 62, No. 1, March 2025 **Page**

Research Articles

Instructions for Authors

Submission of Manuscripts: Manuscripts may be submitted as an e-mail attachment at editor@paspk.org or submit online at http://ppaspk.org/index.php/PPASA/about/submissions. Authors must consult the ***Instructions for Authors*** at the end of this issue or at the Website: www.paspk.org/proceedings/ or www.ppaspk.org.

Proceedings of the Pakistan Academy of Sciences: A Physical and Computational Sciences 62(1): 1-10 (2025)
Copyright © Pakistan Academy of Sciences
ISSN (Print): 2518-4245; ISSN (Online): 2518-4253
http://doi.org/10.53560/PPASA(62-1)855

Pakistan Academy of Sciences

Research Article

GIS Based Modelling of Soil Erosion in Panjkora River Basin Using Revised Universal Soil Loss Equation (RUSLE)

Uzair Ahmad[1,2*], Fazli Amin Khalil[3], Muhammad Kaleem[1], and Zahid Khan[4]

[1]Agriculture Department, Government of Khyber Pakhtunkhwa, Peshawar, Pakistan
[2]PMAS, Arid Agriculture University, Rawalpindi, Pakistan
[3]Department of Electronics, University of Peshawar, Peshawar, Pakistan
[4]Department of Geomatics and Geography, University of Peshawar, Peshawar, Pakistan

Abstract: Research work was conducted to identify the effect of soil errosion on agriculture practices in Panjkora river basin, Khyber Pakhtunkhwa, Pakistan. It is situated in the Eastern Hindu Kush mountain of Pakistan, with an area of 5905 km^2. Geo-informatics strategies (GIS) and Revised Universal Soil Loss Equation (RUSLE) were collectively applied to investigate soil degredation. The outcomes reveal that the R factor was in the range of 38.83 to 111.9 MJ mm/ha/h/year, with the minimum values in the Southeastern part, and maximum values in the northern-western part of the basin. For the entire basin, the Topographic Factor (LS) went from 1.34 to 31.20. Besides, the precarious developed slopes are isolated by groove-formed valleys and fundamentally contribute to the sediment supply in the Panjkora River Basin. The review confirms that a high pace of erosion (1-5 ton/ha/yr) is found near the riverbank which reveals that water caused excessive erosion, adversely affecting the land productivity in the agricultural area. It is suggested that viable management methodologies such as terracing, and stream banks stablization are necessary, to decrease the erosion rate in the area where the people mainly relied on agricultural activities for their livelihood.

Keywords: GIS, Remote Sensing, RUSLE, Soil Erodibility Factor, Panjkora River Basin.

1. INTRODUCTION

Globally, land degradation and soil erosion are very critical issues [1-3]. Besides, it is among the very troublesome natural issues that has expanded during the twentieth (20th) century [4, 5]. A Large number of land degradation is recorded in the Asia, Africa and south America, with a typical 30-40 ton/ha/yr making gigantic loss to the worldwide economy and agricultral productivity [6]. This phenomenan is commonly situtated more, where soil is sloping and shallow, for example the highland of Ethiopian [7]. This can prompt an irreversible loss of soil and land debasement. Not withstanding other natural issues looked by ranchers in Pakistan, the land and soil erosion are of primary concern. Moreover, the soil erosion might adversely affect the soil fertility. These issues are noted for the most part in farming area in tropical and semi dry nations. It is likewise a danger to maintainable farming creation and water quality in the region. Pakistan is dominatingly a dry-land country where 80% of its property region is dry or semi-dry and around 12% is dry sub-moist while the excess 8% is humid [8]. Around 16 million hectares (Mha) of land - 20%, in Pakistan is impacted by soil erosion while its 70% (around 11.2 Mha) is by water erosion [9]. There are different factors that largely affects soil erosion, as they are connected to land use, vegetation type, soil properties and topography etc. The flooding unfavorably affects soil fertility that subsequently eliminates the nutrient rich surface of soil, in result decreases the plant development rate. Furthermore, the more penetrable earth layers are set off to increase run off, in outcome low accessibility of water for plants development. Consequently, observing of soil erosion is significant to evaluate and assess various issue [10].

Received: April 2024; Revised: February 2025; Accepted: March 2025
* Corresponding Author: Uzair Ahmad <uzairahmedsparc770@gmail.com>

Geographic information system (GIS) is considered to be a fundamental tool which can gives spatial soil erosion model. The previously mentioned model shows quantitative soil loss in light of erosion plots though; have a few limits like expense, representativeness, and sureness of the resultant data. This model couldn't give a spatial scattering of soil erosion loss because of the limitation of restricted samples in multifaceted conditions for a geospatial investigation of natural intricacy, possibility and unconventionality [11].

Further, utilizing these traditional techniques to evaluate the soil erosion is practically a tedious work. A number of numerical procedures and models have been attempted to estimate the soil loss [12]. Most normal and generally utilized conditions are Revised Universal Soil Loss Equation (RUSLE) and the Universal Soil Loss Equation (USLE) [13]. The RUSLE gauges that how the environment, soil, topography and land use will influence the inter-rill and rill soil erosion brought about by raindrop effect and surface overflow [14]. It has been broadly used to evaluate assess the soil erosion hazards and soil erosion loss while guide the development and protection of projects to relieve soil erosion under different land-cover circumstances [15]. Meanwhile, utilizing conventional methodologies, it is practically difficult to evaluate soil erosion at the watershed scale. While, the current methodologies for finding soil erosion regions depend on physical surveys, which are costly and time-consuming to complete projects of small scale. Soil erosion and land degradation evaluation is a complicated course of geology that requires multidisciplinary and long-term knowledge. Considering its convenience in application and closeness the digital elevation model (DEM), remote sensing data and detailed evaluation of erosion risks can be examined by utilizing GIS effectively [16]. The most recent advances in spatial information technology have expanded the applicability of current techniques. It has given efficient strategies for monitoring, management, and analysis of earth resources [15].

The primary focal point of this study is to predict the probability of soil erosion inside the Panjkora basin utilizing the Revised Universal Soil Loss Equation (RUSLE); it addresses the method for working out soil erosion for a given site by utilizing five main factors. Various parameters can be utilized to estimate the soil erosion at a specific place. In this manner, the results from the RUSLE address long-term averages more unequivocally. Because of applying GIS, we had the option to map different RUSLE parameters, which were then used to forecast the intensity of soil erosion in the basin. Moreover, a novel evaluation of soil erosion is adopted in the Panjkora River Basin for 2023 using the RUSLE model within a GIS framework. In previous research work Nasir *et al.* [17] the same area has been explored however, it has low precision due to coarse resolution data (30 meter DEM, global land cover satellite imagery), missing rainfall data for one metrological station from 1995 to 2007, and considering the onward data from 2008 to 2016 in comparison with other station's data from 1995-2016. It also neglects the integral soil erosion assessment while selecting the Equation for rainfall erosivity factor for Köppen climate classification. Moreover, the study was conducted for the year 2016 and concluded that annual soil loss in the region ranges from 0 to 3,290 tons/ha/year; however, as per the report if the topsoil is considered 15 cm then there is a maximum of 2000 tons/ha soil available [18-20], which is beyond the maximum limit of the soil available in 1 hectare. Furthermore, Raymond *et al.* [21] elaborated that the top 15 cm (approximately 6 inches) of soil in one hectare weigh around 2,000,000 kilograms (2,000 metric tons) of the maximum soil in one hectare according to Soil Bulk Density using the formula (1).

$$\mathrm{Weight(kg)} = \mathrm{Area(m^2)} \times \mathrm{Depth(m)} \times \mathrm{Bulk\ density}\left(\frac{\mathrm{kg}}{\mathrm{m^3}}\right) \quad (1)$$

Therefore, the results of Nasir *et al.* [17] seem to be ambiguous. Furthermore, the work on national-scale studies [22], suffers from coarse resolution (500 meter for land cover and 1 km resampled resolution for other parameters) that is unsuitable for the basin's hilly terrain. In contrast, this research employs high-resolution satellite imagery (10 meters spatial resolution) and a finer DEM (2.5 meter) for a more precise analysis. Unlike the previous study, it incorporates the Köppen climate classification for rainfall erosivity using Equation (2) Jain *et al.* [23].

$$R = 81.5 + 0.3P \quad (2)$$

It validates the model's results with detailed field surveys and data collected for sediment discharge at Zulüm Bridge. This focus on high-resolution data, detailed climate considerations, and field validation provides a more accurate and localized assessment of soil erosion in the Panjkora River Basin compared to previous studies.

1.1. Study Area

This study is conducted in the Mountainous Range of Hindukush, in the North-West of Pakistan, that covers an area of 5905 km^2. It stretches at the North Latitude 34°39′30″ to 35°47′17″ and 71°13′8″ to 72°22′13″East longitude. Panjkora River is a significant tributary of the Swat River, a narrow gorge prompts Khal, where it streams toward the south. Nonetheless, downstream from Khal, the stream enters a wide valley. The river passes from the centre of "Dir Valley". The name Panjkora is a blend of two words, "Panj" and "Khwar" that implies to five streams. The name Panjkora is given to the river since it is a blend of five significant streams to be specific, the Barawal stream, Sheringal, Gwaldai, and Kohistan streams. The Panjkora River is joined by a somewhat larger drainage region than the Swat River. Indeed, the stream makes a sharp twist toward the south and enters a little canyon. After arriving at Munda Head Works, it disperses across the plains of the Peshawar Basin. The records of Amandara gauge station suggest a typical summer release of 4,488 cusecs while a colder time of year release of 932 cusecs. The geology of the basin is overwhelmed by the hill and mountains that are the portion of the reaches/part of the Hindu-Kush. The mountain ranges, have some high peaks in the basin where it exceeds than 7,690 meters in level.

The central area elevation varies from 3,000 to 2,000 meters in height. In the south, at the juncture of the Panjkora and Swat streams, the height declines rapidly to about 600 meters. The ranges have mostly been cut by the Panjkora River and its tributaries. It is these narrow gorges that most people reside in and raise agriculture. There is plenty of water in the rivers and nallahs, but is not calm to use for irrigation because the mountains are on either side of the river banks. The majority of the area is rugged. The farming occurs on mound slopes and in the gorges. Wheat, maize, and rice are the principal crops grown in the Basin. Fruits and vegetables of many varieties are also grown. The weather of the basin in the summer is mild and warm during the day and cold during the night in the north of the basin. June and July are very hot months in the central and southern areas of the basin. In June, the mean limit and extreme temperature were recorded at 32.52 °C and 15.67 °C, respectively. During the spring season, the hurricane from Lowari Top known as Badama, emerges in the evening making the weather hard and unendurable. The colder season is cold and unadorned. The temperature quickly decreases in November and onward. December, January, and February are freezing months when the temperature decreases near or below to freezing point with 3 to 11 feet of snowfall on high mountains. The mean limit and extreme temperature in January were noted as –10 °C to 11.22 °C. The study area is highlighted in Figure 1.

The purpose of this research is the Spatio-temporal analysis of soil erosion in the Panjkora River Basin. To identify its effect on farming practices in the study area and to limit its effects. In the future, it would provide insight for government and non-government organizations dealing with soil erosion, particularly in Khyber Pakhtunkhwa.

More than 80 percent of the global agricultural land experiences moderate to severe erosion, leading to productivity loss, as well as an array of environmental concerns [24]. This erosion has also been proven as a danger to sustainable agriculture production as well as water quality. Determining the extant of soil erosion problems requires a quantitative evaluation to develop appropriate management styles.

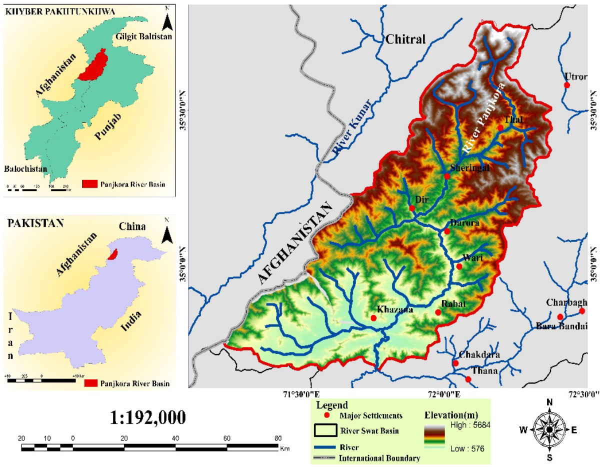

Fig. 1. Study area map (Panjkora River Basin).

2. MATERIALS AND METHODS

2.1. Data Set

Data collected from primary as well as secondary data sources were exported to the ArcGIS Platform for RUSLE model parameters, that are LS factor (Steepness Factor and Slop Length), R factor (the rainfall-runoff erosivity factor), K factor (soil erodibility factor), C factor (cover-management factor) and P factor (support practice factor). DEM (digital elevation model) was generated from Google Earth. The slope for the study area was generated from DEM. Flow direction and flow accumulation were generated through DEM for the extraction of the LS factor. The slope was converted to a vector; grid codes were merged, based on % slope values of the P factor [25] to obtain the P factor Map. Rainfall data from PMD (Pakistan Metrological Department) was obtained from the metrological station within the river basin and the R factor was generated. K factor was calculated from Digital Soil Map of World (DSMW) Food and Agriculture Organization, United Nations. The classified imagery was converted to polygon, gird codes of each land use class were merged to 9 grid codes as per land use classes, and a Cover management factor was generated.

2.2. RUSLE Parameters

By manual digitization and control passage, the data and their associated properties for the model were input into ArcGIS. With a grid cell design data sources were coordinated into ArcGIS. Each portrayed cell (pixel) had a unique region, in space fixed on by grid orientation. To process the review region of the potential erosion rate for the area-weighted mean, the zonal statistical tool was utilized. In the following segment subtleties on processing strategies and on data under particular (RUSLE) factors are given.

Topographic Factor (LS): also known as Steepness Factor (LS) and Slope Length, mirrors the influence of geography on soil erosion. Higher overland stream speed is caused by the incline length and a rising slope, consequently increasing the soil erosion [26]. The detail is shown pictorialy in Figure 2. The LS factor was developed as follows using Equation (3) in raster calculator:

$$\text{LS} = (\text{Flow Accumulation} \times 1.375)^{0.5} \times (0.065 + 0.045 \times \text{Slope} + 0.0065 \times (\text{Slope} \times \text{Slope})) \quad (3)$$

In this study a consistent (m) of 0.5 was utilized in above Equation, because of the mean slope more noteworthy than 25% (15°) noticed for the survey area [27].

Support Practice Factor (P): it refers to the soil Conservation Practices carried out to lighten soil erosion. Contour cultivating, terracing, and strip trimming are the ordinarily indexed and archived control measures (Table 1) [28]. It range from 0 to 1, 0 addresses a generally excellent human-centered erosion resistance facility, and one demonstrates a non-human-centered resistance erosion facility. The P factor is illustrated in Figure 3.

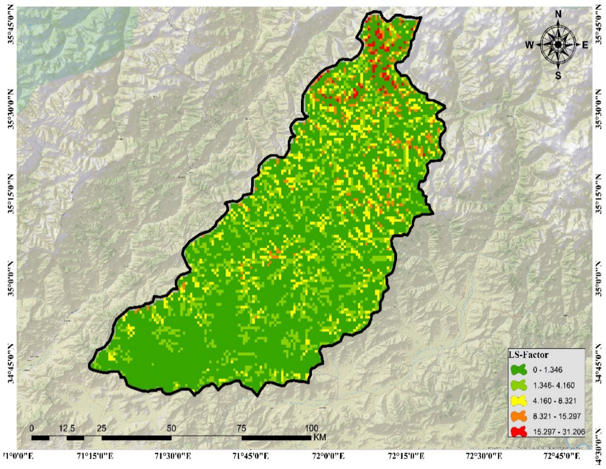

Fig. 2. Slope length and steepness LS-factor of Panjkora River Basin.

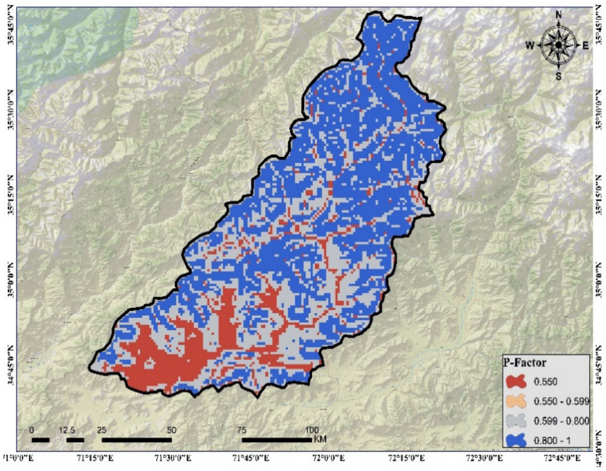

Fig. 3. Shows support practice (P-Factor) of Panjkora River Basin.

Table 1. Support practice factor values as per soil conservation practice [28].

Slop (percent)	Strip cropping	Contour cropping	Terrace cropping	
			Bench	Croad-based
0-7.0	0.27	0.55	0.10	0.12
7.0-11.3	0.30	0.60	0.10	0.12
11.3-17.6	0.40	0.80	0.10	0.16
17.6-26.8	0.45	0.90	0.12	0.18
>26.8	0.50	1.00	0.14	0.20

Cover Management Factor (C): it addresses the soil erosion proportion from land tillaged under specific circumstances. It concludes how normal vegetation or yield cover reduces precipitation energy and overflow or captures precipitation energy and increments penetration. It is the second most critical element near precipitation erosivity and topography that controls the threat of soil erosion [29]. The Figure 4 shows Land Use Land Cover map of the study area while the Figure 5 illustrates C factor map for the study area.

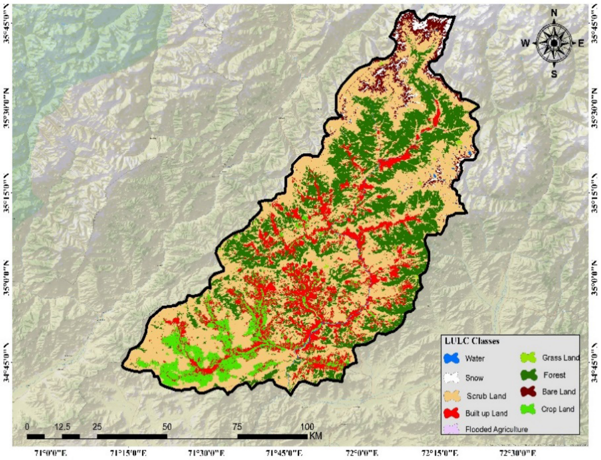

Fig. 4. Land use/land cover distribution.

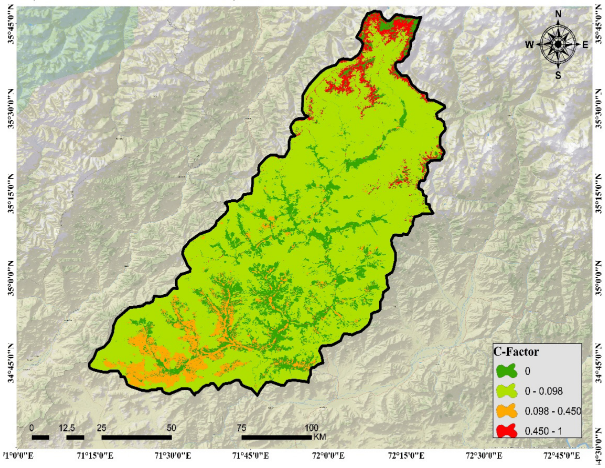

Fig. 5. Cover management (C factor) of Panjkora River Basin.

Table 2. Cover management factor.

S. No.	Land use	C Factor
1	Forest	0.03
2	Shrubland	0.03
3	Grassland	0.01
4	Agricultural Land	0.21
5	Barren Land	0.45
6	Built-up	0.00
7	Snow Glacier	0.00
8	Water body	0.00

Rainfall Runoff Erosivity Factor (R): Rainfall Erosivity Factor "R" considers how much rainfall to introduce the peak intensity sustained over a lengthy period, showing the expected capacity for rainfall to causes soil loss. It depicts the idea of rainfall erosivity as a collaboration between the kinetic energy of raindrops and the soil surface [30]. R factor essentially affects soil loss [31] as shwon in Figure 6. The R factor is calculated using Equation (4):

$$R = 81.5 + 0.38P \tag{4}$$

Where,
R addresses the Rainfall Erosivity Factor,
P is the Mean Annual Rainfall in mm.

Soil Erodibility Factor (K): it is alluded to as the defenselessness of a soil molecule type to erosion by precipitation and overflow. All small parts of the topsoil layer comprise organic carbon, silt, sand, and clay which makes the soil erodibility factor (Figure 7) expected to estimate the K factor utilized by the following numerical relations depicted in [3]. Numerous researchers consider the topsoil layer to compute the K factor since it is impacted directly by the raindrop energy. The K factor values for the DSMW soil layers of the study area were acquired using the following Equations (5), (6), (7), (8), and (9), based on which the soil layers are developed as a K factor map.

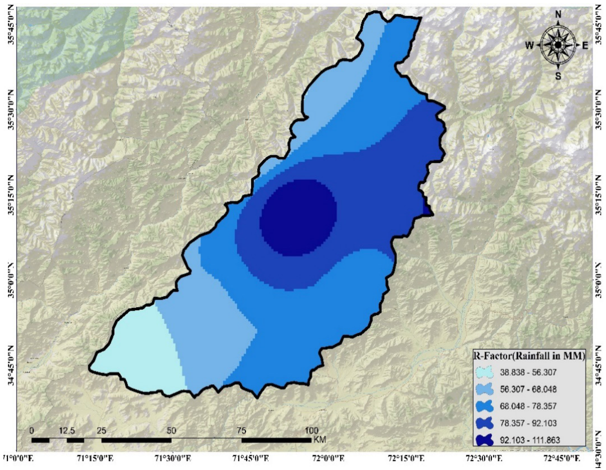

Fig. 6. Rainfall-runoff erosivity (R Factor) of Panjkora River Basin.

$$K_{Factor} = f_{Sand} \times f_{Clay} \times f_{OrgC} \times f_{Silt} \times 0.1317 \quad (5)$$

$$f_{Sand} = \left(0.2 + 0.3 \times \exp\left[-0.256 \times m_{Sand}\left(1 - \frac{m_{Silt}}{100}\right)\right]\right) \quad (6)$$

$$f_{Clay} = \left(\frac{m_{Silt}}{m_{Clay}+m_{Silt}}\right)^{0.3} \quad (7)$$

$$f_{Orgc} = \left(1 - \frac{0.0256.OrgC}{Orgc+\exp[3.72-2.95.OrgC]}\right) \quad (8)$$

$$f_{Silt} = \left(1 - \frac{0.7\left(1-\frac{m_{Sand}}{100}\right)}{\left(1-\frac{m_{sand}}{100}\right)+\exp\left[-5.51+22.9.\left(1-\frac{m_{Sand}}{100}\right)\right]}\right) \quad (9)$$

The proposed study is conducted step wise using the following methodology. Firstly, data was collected from Sentinel-2A Multi Spectral Instrument (MSI) and Climate data repository. DEM is obtained from google earth. The C factor and R-Factor were obtained from satellite and climate data while LS and P factor were obtained from DEM data respectively. Moreover, K factor was obtained using DSMW, detail is shown in Figure 8. Finally, the developed RUSLE model is executed in model builder of ArcGIS version 10.8.

3. RESULTS AND DISCUSSIONS

All the layers were combined in Raster Calculator according to the Equation (10) as mentioed by Koirala *et al*. [29].

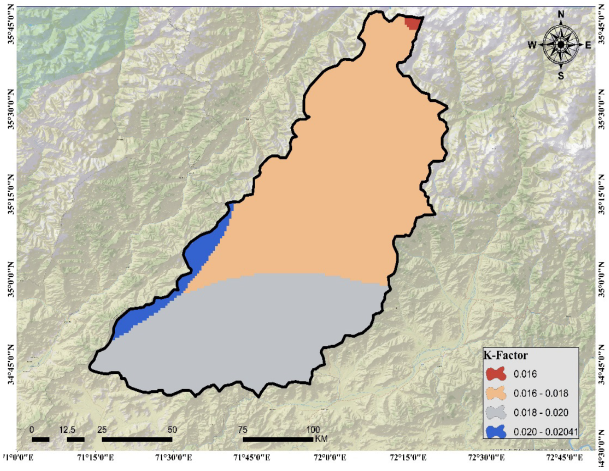

Fig. 7. Soil erodibility (K Factor) of Panjkora River Basin.

$$A = R \times LS \times K \times C \times P \quad (10)$$

The erosion was classified into five classes Low Erosion (>0), Moderate Erosion (1-5), High Erosion (5-10), Very High Erosion (10-20) and Severe Erosion (20-37.43). The Study reveals that the maximum area near the Panjkora River is under moderate erosion ranging from 0 to 5 tons/ha/yr in 2021. Residents of the area live near the Panjkora River as the rest of the area is mountainous and agriculture practices are affected by the erosion leading to a loss in productivity and food quality. It is also identified that the maximum erosion in the study area is by water as shown in Figure 9.

RUSLE-calculated land degradation annauly in the Panjkora basin is presented in Figure 9 through regional distribution. The yearly soil loss falls into five graded classes starting from low erosion through very high erosion to severe erosion. The examined territory experiences yearly soil loss between 0 -37.43 tons per hectare annually. Figure 9 illustrates the extent of land under each soil erosion severity rank in the research area. Research findings demonstrate that soil loss effectiveness presents greater sensitivity to barren lands combined with high-altitude bare granite slopes in comparison to vegetation-covered areas. Panjkora basin presents moderate soil erosion as its primary form (78%) yet high to severe erosion exists in certain upper north areas (5%) and the remaining sections with low erosion make up (17%). The annual sediment output originates from 4.51 million tons of soil that

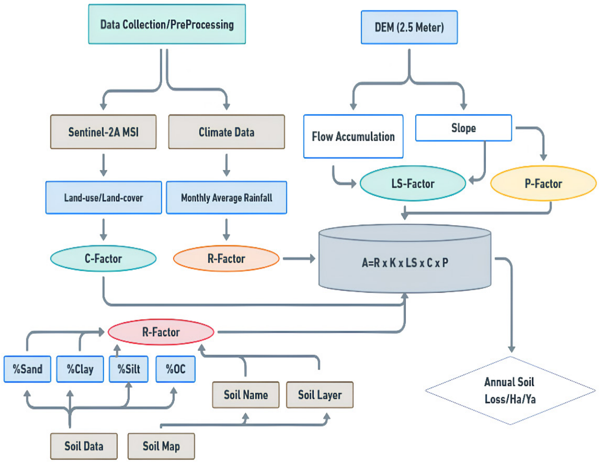

Fig. 8. Flow chart of the proposed study.

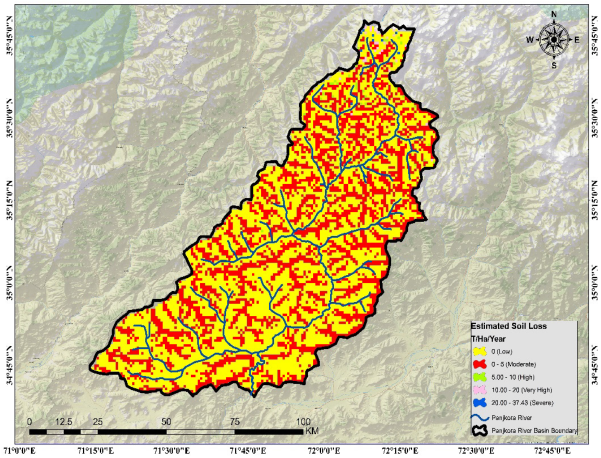

Fig. 9. Annual soil loss in Panjkora River Basin.

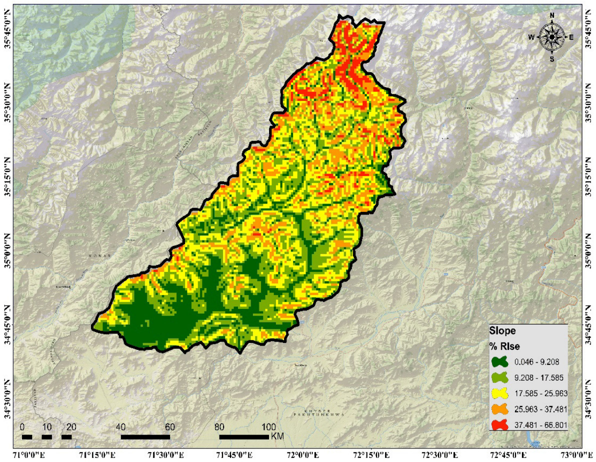

Fig. 10. Shows the slope map for the study map.

exists within coniferous and alpine forest terrain extending from 1,000 - 4,000 m and 4,000+ m mean sea level. The Panjkora basin exhibits steep slopes that mainly exist in its north and northeastern part of the basin shown in Figure 10. When granite feldspar encounters rainwater it transforms into white clay material known as kaolinite due to hydrolysis. The hydrolytic process transforms both biotite and muscovite mica types into kaolinite [31]. Soil erosion risk is high because the area contains steep slopes representing 64 percent of the total space while P-factor reaches 0.599 (Figure 3). This area features slopes exceeding 8.321% that result in these conditions. According to Phinzi *et al.* [32] the annual rate at which soil erosion is happening was strongly correlated with the LS-factor. Also, the panjkora basin suffer from extremely high soil erosion where agriculture is carried out on the apron parts of alluvial fans that extend into the pediments of mountains. The current study predicted a 5.94 million tons sediment output, compared to hydrological station data (5.5 million tons) situted at Zulam bridge, Timargara. The C factor of different parts of the Panjkora basin in terms of vulnerability to soil erosion is depicted in Figure 4. The results show that 78% of the entire area has a moderate soil erosion. The high, very high and severe erosion class comprises of only 5% of the total area of Panjkora basin. These regions are mostly sandy shallow soils and badly eroded steep slopes clad with little vegetation coupled with poor crop and soil conservation practices.

The quantity of annual losses throughout Potohar region reached 97.81 million tons/ha/year according to multiple studies [34, 35]. A 58 tons/ha/year rate of soil loss was determined through research performed on the Chitral river basin. The calculated total yearly erosion rate of soil amounts to 31 million tons per year. The annual soil erosion in Pakistan was estimated in [23] through RUSLE model analysis. The research establishes soil deficit rates for different administrative areas across Pakistan during one year. The research demonstrates that Khyber Pakhtunkhwa experiences annual soil deterioration at a level of 12.84 ± 39.897 tons/ha/yr [22]. The present study adds information to existing knowledge databases through field measurements as it uses high-resolution data while applying RUSLE model. Soil erosion measurements achieved by this methodology define a specific measurement of 37.43 tons/ha/yr for the Panjkora Basin area. The provincial estimate by Gilani *et al.* [22] supports the validity of the proposed study results conducted in Panjkora Basin.

High sediment deposition significantly hinder water resources storage, primarily by decreasing dam storage capacity and causing deposition within water distribution networks. Dutta [33] reported that the current water-holding capacity of major dams in Asia and the Middle East is approximately 1450 x 10^9 m^3, with siltation leading to an annual reduction of 0.8%. Consequently, sediments occupy 40% of the initial capacity in Asian dams, highlighting the substantial negative impacts on the region's long-term sustainability [34]. Notably, the Terbela Dam's anticipated a yearly sediment inflow of 325 million tons [35]. However, sediment accumulation has significantly reduced the reservoir capacity, from an initial 14.34 billion cubic meters to the current 10.04 billion cubic meters. This excessive sedimentation has considerably diminished the water storage and power generation capacity of major dams in pakistan, including Terbela, Warsak, and Mangla.

4. CONCLUSIONS

The proposed study was conducted in Panjkora basin to estiamate land degradation. The result demonstrates that the target area have intermediate vulnerability to soil erosion. Furthermore, the results also depicts that slope exceeding 8.321% with C factor values above 0.450 shows an attentive distribution pattern that leads to high erosion levels. The RUSLE model demonstrates that agricultural regions penetrating the foothills have moderate amounts of soil loss. It also calculates that the annual soil loss from the basin amounts 5.94 million tons. The obtained data will provide essential information that enables planners and policymakers to develop better land management practices. The research findings provide useful data to both land and water resource management authoraties to take proper soil conservation measures, including suitable crop management systems and construction of check dams and streambank stabilization structures. Spatial representations of soil erosion rates, through the generation of soil risk maps, can effectively identify critical erosion hotspots. By pinpointing such areas, efforts and resources can be strategically targeted to mitigate further erosion. The identification of these erosion-prone zones constitutes the initial step towards developing effective soil and water conservation plans, a crucial aspect in addressing food scarcity concerns, particularly within the Panjkora River Basin.

5. ACKNOWLEDGEMENTS

We acknowledge the support of Remote Sensing & GIS Research Lab, Crop Reporting Services, Agriculture Department, Khyber Pakhtunkhwa for provision of data and state of the art research tools like, ArcGIS v10.8 (licensed), workstation PC for analysis and technical staff for field visit.

6. CONFLICT OF INTEREST

Authors declare no conflict of interest.

7. REFERENCES

1. O. Fistikoglu and N.B. Harmancioglu. Integration of GIS with USLE in assessment of soil erosion. *Water Resource Management* 16(6): 447-467 (2002).
2. A. Pandey, A. Mathur, S.K. Mishra, and B.C. Mal. Soil erosion modeling of a Himalayan watershed using RS and GIS. *Environment Earth Science* 59(02): 399-410 (2009).
3. N. Hoyos. Spatial modeling of soil erosion potential in a tropical watershed of the Colombian Andes. *Catena* 63(1): 85-108 (2005).
4. S.D. Angima, D.E. Stott, M.K. O'Neill, C.K. Ong, and G.A. Weesies. Soil erosion prediction using RUSLE for central Kenyan highland conditions. *Agricultre Ecosystem Environment* 97(1-3): 295-308 (2003).
5. S.W. Trimble and P. Crosson. U.S. soil erosion rates - Myth and reality. *Science* 289(5): 248-250 (2000).
6. J. Ananda and G. Herath. Soil erosion in developing countries: A socio-economic appraisal. *Journal of Environmental Management* 68(4): 343-353 (2003).
7. L. Tamene and P.L.G. Vlek. Assessing the potential of changing land use for reducing soil erosion and sediment yield of catchments: A case study in the highlands of northern Ethiopia. *Soil Use Management* 23(1): 82-91 (2007).
8. K.M. Azeem, M. Ahmad, and H.H. Shah. Review of Available Knowledge on Land Degradation in Pakistan. *International Center for Agricultural Research in the Dry Areas*. OASIS Country Report 3 (2012). https://mel.cgiar.org/reporting/downloadmelspace/hash/jQCsHC7L/v/5187b5f97f4ae1968c47768e7817e61b.
9. A. Nasir, K. Uchida, M. Shafiq, and M. Khan. Monitoring Soil Erosion in a Mountainous Watershed under high rainfall zone in Pakistan. *Journal of Rural Enviroment Engineering* 43(1): 23-30 (2006).

10. C.K. Dissanayake, P. Mahawatte, K. Abeynayake, and T.S.B. Weerasekera. Use of Caesium-137 technique for the assessment of soil erosion in two selected sites in Uma Oya Catchment in Sri Lanka. *19th World Congress of Soil Science, Soil Solutions for a Changing World (1st-6th August 2010), Brisbane, Australia* (2010).
11. D. Simandan. Kinds of environments- a framework for reflecting on the possible contours of a better world. *Canadian Geographies* 55(3): 383-386 (2011).
12. W. Wischmeier and D. Smith. Predicting rainfall erosion losses: a guide to conservation planning. *U.S. Department Agriculture Handbook* 537: (1978).
13. D.D. Wischmeier and W.C. Smith. Predicting rainfall erosion losses. A guide to conservation planning. The USDA Agricultural Handbook No. 537. *Maryland, USA* (1978). https://www.ars.usda.gov/ARSUserFiles/60600505/RUSLE/AH_537%20Predicting%20Rainfall%20Soil%20Losses.pdf.
14. K. Renard, G. Foster, G. Weesies, D. McCool, and D. Yoder. Predicting soil erosion by water: a guide to conservation planning with the Revised Universal Soil Loss Equation (RUSLE). Agriculture Handbook No. 703. *United States Department of Agriculture, USA* (1997). https://www3.epa.gov/npdes/pubs/ruslech2.pdf.
15. A.A. Millward and J.E. Mersey. Adapting the RUSLE to model soil erosion potential in a mountainous tropical watershed. *Catena* 38(2): 109-129 (1999).
16. Y.Q. Xu, X.M. Shao, X.B. Kong, P. Jian, and Y.L. Cai. Adapting the RUSLE and GIS to model soil erosion risk in a mountains karst watershed Guizhou Province China. *Environment Monitering Assessment* 141(3): 275-286 (2008).
17. M.J. Nasir, S. Alam, W. Ahmad, S. Bateni, J. Iqbal, M. Almazroui, and B. Ahmad. Geospatial soil loss risk assessment using RUSLE model: a study of Panjkora River Basin, Khyber Pakhtunkhwa, Pakistan. *Arabian Journal of Geosciences* 16(7): 440 (2023).
18. D. Murphy, V. Gonzalez-Quinones, and A. Wherrett**.** Bulk Density - On Farm Use. (2024). https://www.soilquality.org.au/factsheets/bulk-density-on-farm-use.
19. G. Sela. Units on the Soil Test Report (2024). https://cropaia.com/blog/soil-test-units/.
20. CitizenMaths. Online Website (2024). https://citizenmaths.com/area-density/grams-per-hectare-to-tonnes-per-hectare.
21. R.R. Weil and N.C. Brady (Eds.). The Nature and Properties of Soils (15th ed.). *Pearson Education, New York, USA* (2017).
22. H. Gilani, A. Ahmad, I. Younes, S. Abbas, and H. Gilani. Estimation of annual soil erosion dynamics (2005-2015) in Pakistan using Revised Universal Soil Loss Equation (RUSLE). *Authorea* 33(1): 204-217 (2021).
23. M.K. Jain and D. Das. Estimation of sediment yield and areas of soil erosion and deposition for watershed prioritization using GIS and remote sensing. *Water Resources Management* 24(10): 2091-2112 (2010).
24. D. Pimentel and M. Burgess. Soil erosion threatens food production. *Agriculture* 3(3): 443-463 (2013).
25. G.J. Shin. The analysis of soil erosion analysis in watershed using GIS. Ph.D. Thesis. *Kangwon National University, Chuncheon, South Korea* (1999).
26. A. Maqsoom, B. Aslam, U. Hassan, Z.A. Kazmi, M. Sodangi, R.F. Tufail, and D. Farooq. Geospatial assessment of soil erosion intensity and sediment yield using the Revised Universal Soil Loss Equation (RUSLE) model. *ISPRS International Journal of Geo-Information* 9(6): 365 (2020).
27. K. Renard, G. Foster, G. Weesies, D. McCool, and D. Yoder. Predicting soil erosion by water: a guide to conservation planning with the Revised Universal Soil Loss Equation (RUSLE). Agriculture Handbook No. 703. *Agricultural Research Services, United States Department of Agriculture, USA* (1997). https://www.tucson.ars.ag.gov/unit/publications/PDFfiles/717.pdf.
28. M.H. Pesaran and Y. Shin. An autoregressive distributed lag modelling approach to cointegration analysis. *Department of Applied Economics, University of Cambridge,* Cambridge, *UK* (1995). https://citeseerx.ist.psu.edu/document?repid=rep1&type=pdf&doi=743dc1e8cf7eea4a2ac9bc58907f2ce08a1f5d90.
29. P. Koirala, S. Thakuri, S. Joshi, and R. Chauhan. Estimation of Soil Erosion in Nepal using a RUSLE modeling and geospatial tool. *Geosciences* 9(4): 147-180 (2019).
30. K. Fidele, C. Zhang, F. Ndayisaba, H. Shao, A. Kayiranga, X. Fang, L. Nahayo, E. M. Nyesheja, and G. Tian. Extent of cropland and related soil erosion risk in Rwanda. *Sustainability* 8(7): 609-615 (2016).
31. M.K. Jain and D. Das. Estimation of sediment yield and areas of soil erosion and deposition for

watershed prioritization using GIS and remote sensing. *Water Resourceses Management* 24(10): 2091-2112 (2010).

32. K. Phinzi, N.S. Ngetar, and O. Ebhuoma. Soil erosion risk assessment in the Umzintlava catchment (T32E), Eastern Cape, South Africa, using RUSLE and random forest algorithm. *South African Geographical Journal* 103(2): 139-162 (2021).
33. S. Dutta. Soil erosion, sediment yield and sedimentation of reservoir: a review. *Modeling Earth System and Environment* 2: 123 (2016).
34. D.E. Walling. Human impact on the sediment loads of Asian rivers. *Sediment Problems and Sediment Management in Asian River Basins* 349: 37-51 (2011).
35. M.U. Rashid, A.S. Shakir, and N.M. Khan. Evaluation of Sediment Management Options and Minimum Operation Levels for Tarbela Reservoir, Pakistan. *Arab Journal Science and Engineering* 39(4): 2655-2668 (2014).

Proceedings of the Pakistan Academy of Sciences: A Physical and Computational Sciences 62(1): 11-19 (2025)

ISSN (Print): 2518-4245; ISSN (Online): 2518-4253
http://doi.org/10.53560/PPASA(62-1)873

Pakistan Academy of Sciences

Research Article

Numerical Simulation of Nonlinear Equations by Modified Bisection and Regula Falsi Method

Inderjeet and Rashmi Bhardwaj*

Nonlinear Dynamics Research Lab, University School of Basic and Applied Sciences, Guru Gobind Singh Indraprastha University, Dwarka, 110078, Delhi, India

Abstract: The study of nonlinear equations and their effective numerical solutions is crucial to mathematical research because nonlinear models are prevalent in nature and require thorough analysis and solution. Many methodologies have been developed to obtain the roots of nonlinear equations, which have significant applications in several areas, especially engineering. However, all of these methods have certain challenges. The development of efficient and effective iterative methods is, therefore, very important and can positively impact the task of finding numerical solutions to many real-world problems. This paper presents a thorough analysis of a numerical approach for solving nonlinear equations using a recently proposed technique, which is a modification of the Regula-Falsi and Bisection numerical methods. The purpose of this work is to provide a novel and effective approach to solving nonlinear equations. The iterative technique for solving nonlinear equations, which has been examined in many scientific and technical domains, is based on the conventional Bisection and Regula-Falsi methods. The proposed approach for finding roots of nonlinear equations achieves second-order convergence. The performance of the newly developed technique was compared with conventional Bisection, Regula-Falsi, Steffensen, and Newton-Raphson methods, and its convergence was validated using several benchmark problems with different iterations. The results showed that, in terms of iterations, the newly developed method performed better than the traditional Bisection, Regula-Falsi, Steffensen, and Newton-Raphson approaches. This supports the credibility of the recently developed method and offers promise for future studies aimed at further refinement. MATLAB R 2021a is used for numerical results. Besides this, the newly developed technique also has certain limitations. For instance, it cannot cover all possible types of nonlinear equations. Further testing on a broader range of functions, particularly those arising from specific scientific and engineering applications, would be valuable. Additionally, our current study focuses on one-dimensional root finding. Extending the approach to systems of nonlinear equations is an important direction for future research.

Keywords: Error Analysis, Convergence Order, Iterations, Numerical Examples.

1. INTRODUCTION

Mathematical equations that model real-world situations are often either linear or nonlinear in nature. The solution to the given problem can be found in the roots of these equations. Since obtaining an accurate solution is essential for problem-solving, an efficient numerical technique for root-finding problems is crucial in mathematical computations. The "root-finding problem" is to identify root of the equation $f(x) = 0$, where f is a function of single variable. Finding root is challenging problem in many fields, such as engineering, chemistry, agriculture, biosciences. This is because formulas for problems involving real-world issues will always include unknown variables. Solving challenges related to identifying an object's equilibrium position, a field's potential surface, and the quantized energy level of a confined structure are pertinent scenarios in the subject of physics [1].

In reality, root-finding problems arise when determining an unknown variable that appears

---

Received: September 2024; Revised: February 2025; Accepted: March 2025
* Corresponding Author: Rashmi Bhardwaj <rashmib@ipu.ac.in>

implicitly in scientific or engineering formulas, as reported by Ahmad [2]. The development of optimal eighth-order derivative-free methods for multiple roots of nonlinear equations was discussed by Sharma *et al*. [3]. Several numerical techniques exist for solving root-finding problems, including the Regula-Falsi method, Bisection method, Secant method, Newton-Raphson method, and fixed-point iteration. These methods exhibit various convergence rates, such as linear and quadratic, with higher-order methods converging more quickly, as discussed by Ehiwario and Agnamie [4]. The solution of nonlinear models in engineering using a new sixteenth-order scheme and their basin of attraction was examined by Jamali *et al*. [5].

Numerous studies have been conducted to identify the most effective methods for solving root-finding problems. For example, Frontini and Sormani [6] explored this topic extensively. Similarly, Noor *et al.* [7] analyzed the Secant, Newton-Raphson, and Bisection methods before the research by Ehiwario and Agnamie [4] to determine which approach required fewer iterations when solving a nonlinear equation with a single variable, as noted by Srivastava and Srivastava [8]. Previous research has employed various numerical techniques, such as fixed-point iteration and Regula-Falsi methods, to address root-finding problems, as shown in the studies by Ebelechukwu *et al.* [9] and Issac *et al.* [10]. Additionally, Behl *et al.* [11] discussed a new higher-order optimal derivative-free scheme for multiple roots.

Mathematicians and engineers often struggle to find precise solutions to most real-world problems due to their nonlinear nature [12, 13]. Over the past two decades, several techniques have been proposed or applied in this context [13-19]. Since solving nonlinear equations analytically is highly challenging, iterative procedures based on numerical methods provide the only viable approach to obtaining approximate solutions. Several numerical techniques, including Secant, Bisection, Newton-Raphson, Regula-Falsi, and Muller's methods, are available in the literature for finding approximate roots of nonlinear equations. Cordero *et al.* [20] discussed Steffensen-type methods for solving nonlinear equations.

Many polynomial equations of the form $f(x) = a_0 x^r + a_1 x^{r-1} + a_2 x^{r-2} + \cdots + a_r$ where $a_i{}'s$ are constants, $a_0 \neq 0$ are studied in mathematics. An equation that is transcendental is $f(x) = 0$ if $f(x)$ is constant for certain other functions, such as logarithmic, exponential, trigonometric, etc. A common difficulty in scientific and technological activity is finding root of an equation of the form $f(x) = 0$ [21]. If $f(\omega) = 0$, then any number ω is root of $f(x) = 0$. If $f(x) = (x - \omega)^q\, g(x)$, where $g(x)$ is bounded at ω and $g(\omega) \neq 0$, then a root of f is said to have multiplicity q. A multiple zero is ω if $q > 1$, and a simple zero if $q = 1$ [22]. By utilizing the classical Regula-Falsi (R-F) approach, Naghipoor *et al.* [23] developed an improved R-F method and demonstrated that the proposed approach was more effective than the classical R-F method. Shaw and Mukhopadhyay [24] introduced an enhanced predictor-corrector form of the R-F approach in their study, showing that it converges significantly faster than the earlier R-F method. Kodnyanko [25] proposed an improved bracketing parabolic method for the numerical solution of nonlinear equations. Additionally, Jamali *et al.* [26] discussed a new two-step optimal approach for solving real-world models and analyzing their dynamics.

To find the roots of nonlinear equations, Parida and Gupta [27] proposed a hybrid approach that combines the standard Regula-Falsi (R-F) method with Newton-like methods. Experiments on multiple examples demonstrate the superiority of this novel strategy over some existing methods for solving similar problems. Li and Chen [28, 29] introduced a technique for finding single roots that integrates the higher-order convergence of the classical R-F approach with specific parameters of the exponential R-F technique. The proposed strategy exhibits good asymptotic quadratic convergence. Qureshi *et al.* [30] discussed the quadratic convergence of iterative algorithms based on the Taylor series for solving nonlinear equations. Numerical analysis research on estimating a single root of nonlinear functions is crucial, as its applications span various fields in both applied and pure sciences. These applications have been discussed within the general framework of nonlinear problems [31-33], such as the nonlinear equation:

$$f(x) = 0 \tag{1}$$

Due to the significance of equation (1), one of the fundamental methodologies, such as the Bisection technique, is used for estimating the root of nonlinear functions.

$$m = \frac{a+b}{2} \tag{2}$$

The technique (2) is a slow yet robust convergence method, known as the Bisection technique [34]. The Bisection technique is guaranteed to converge for a continuous function on an interval $[a, b]$ where $f(a)f(b) < 0$. Alternatively, the Regula-Falsi technique is another root-finding method used for solving nonlinear problems.

$$x = \frac{a\,f(b)-b\,f(a)}{f(b)-f(a)} \tag{3}$$

The technique (3) is the fast-converging Regula-Falsi method, assessed in comparison to the Bisection technique. Both techniques have linear convergence; however, the Regula-Falsi method occasionally experiences slow convergence. The drawback of the Regula-Falsi technique is mitigated by the Illinois method, as reported by Golbabai and Javidi [35]. Furthermore, a modification of the Newton method was introduced by Chun [36].

Numerous numerical techniques have been proposed, including the quadrature formula, the homotopy perturbation method and its variations, the Taylor series, the divided difference method, the decomposition method, and others [37-41]. Likewise, some two-point algorithms have been developed in the literature to solve nonlinear equations. A similar study, reported by Allame and Azad [42] and Hussain *et al*. [43], integrated the well-known Bisection method, Regula-Falsi method, and Newton-Raphson method to propose a more accurate approach for predicting a single root of nonlinear problems. In this study, a Modified Bracketing technique has been proposed, which combines classical two-point methods. Within the predefined interval, the Modified Bracketing approach performs well in solving nonlinear problems. The proposed method is free of common pitfalls and quickly converges to the root. Moreover, the Modified Bracketing approach is more straightforward and easier to use.

2. METHODOLOGY

In numerical analysis, the Bisection and Regula-Falsi techniques are root-finding methods. Through successive approximation, they use a recursive approach to locate polynomial roots. Let $y = f(x)$ be the graph of an arbitrary function f. Let x_0 and x_1 be an initial approximation of roots of $f(x)$. Let $(x_0, f(x_0))$ and $(x_1, f(x_1))$ be two points on curve $y = f(x)$. Now we draw tangent by joining these two points and x_2 is x-axis intersection of tangent line of function f combining both $(x_0, f(x_0))$ and $(x_1, f(x_1))$ as shown in Figure 1. Equation of line in slope–intercept form joining $(x_0, f(x_0))$ & $(x_1, f(x_1))$ from the Figure 1 is given by:

$$y = \frac{f(x_1)-f(x_0)}{x_1-x_0}(x-x_0)+f(x_0) \tag{4}$$

Equation (4) has a root when y = 0.

$$\rightarrow 0 = \frac{f(x_1)-f(x_0)}{x_1-x_0}(x-x_0)+f(x_0) \tag{5}$$

We have solved this equation with respect to x as follows:

$$x = x_o - \frac{x_1-x_0}{f(x_1)-f(x_0)}\,f(x_0) \tag{6}$$

Equation (6) is known as the Regula-Falsi method. The newly created technique is derived by modifying the Regula-Falsi method formula, utilizing both the Bisection and Regula-Falsi techniques. To modify Equation (6), we first use the Bisection method. The Bisection technique is one method for solving the equation $f(x) = 0$. Assume that f is a continuous function defined on the interval $[a, b]$, and that $f(a)f(b) < 0$. Using this technique, the interval $[a, b]$ is divided in half to select a subinterval that satisfies the Intermediate Value Theorem. The selected subinterval is then

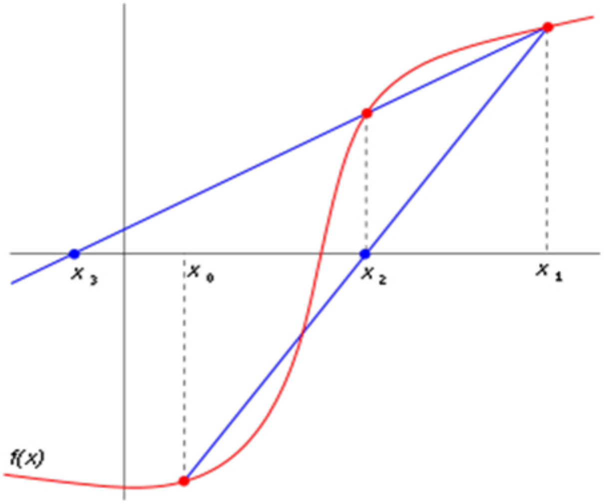

Fig. 1. Geometrical representation of the Regula Falsi method.

extended at both ends and divided in half again. Repeating this process continuously results in an error bound that decreases with each iteration, becoming as small as the interval between successive steps.

So, for first iteration $x_1 = \frac{a+b}{2}$ where $[a, b]$ is an interval in which $f(x)$ has root with $f(a)f(b) < 0.$ For better approximation, we refine the interval $[a, b]$ into the smaller subinterval $[a, \frac{a+b}{2}]$ ensuring that $f(a).f(\frac{a+b}{2}) < 0$

$$x_1 = \frac{a+\frac{a+b}{2}}{2} \tag{7}$$

$$x_1 = \frac{3a+b}{4} \tag{8}$$

Also, we know that $f(x_n) = \Delta(x_n) = b - a = h$ with $b = a + f(a)$ and $x_1 = a + 0.3\,f(a)$. Where a is an initial approximation so we can write as $a = x_0$ and $x_1 = x_0 + 0.3\,f(x_0)$. Substituting this expression for $x_1 = x_0 + 0.3\,f(x_0)$ in Equation (6) and solving, we obtain:

$$x = x_0 - \frac{0.3\,[f(x_0)]^2}{f[x_0 + 0.3f(x_0)] - f(x_0)} \tag{9}$$

In general, the recursive formula is:

$$x_{n+1} = x_n - \frac{0.3\,[f(x_n)]^2}{f[x_n + 0.3f(x_n)] - f(x_n)} \qquad n = 0,1,2,3 \tag{10}$$

Hence, Equation (10) represents the proposed modified technique, which integrates the Bisection and Regula-Falsi methods.

3. CONVERGENCE ANALYSIS OF THE MODIFIED TECHNIQUE

Theorem: Let $\alpha\ \varepsilon$ I be simple zero of sufficiently differentiable function $f : I \subseteq R \to R$ of an open interval I. If x_0 is sufficiently close to α , then technique defined by (8) is of second order and satisfied error equation $e_{n+1} = {e_n}^2[\,0.5\frac{f''(a)}{f'(a)} + 0.15\,f''(a)]$

Proof: Let α be simple zero of f, $e_n = x_n - \alpha$. Using Taylor expansion around $x = \alpha$ up - to second order terms and

$f(\alpha) = 0$, we obtained:

$$f(x_n) = f(e_n + \alpha) = f(\alpha) + e_n f'(\alpha) + \frac{{e_n}^2}{2!} f''(\alpha) = e_n f'(\alpha) + \frac{{e_n}^2}{2!} f''(\alpha)$$

$$[f(x_n)]^2 = {e_n}^2\,[f'(a)]^2 + {e_n}^3\,f'(a)f''(a)$$

$$0.3[f(x_n)]^2 = 0.3{e_n}^2[f'(a)]^2 + 0.3{e_n}^3\,f'(a)f''(a)$$

$$x_n + 0.3f(x_n) = e_n + \alpha + 0.3\,e_n f'(\alpha) + 0.3\,\frac{{e_n}^2}{2!}\,f''(\alpha)$$

$$x_n + 0.3f(x_n) = e_n + \alpha + 0.3\,e_n f'(\alpha) + 0.15\,{e_n}^2\,f''(\alpha)$$

$$f[x_n + 0.3f(x_n)] = f[e_n + \alpha + 0.3\,e_n f'(\alpha) + 0.15\,{e_n}^2\,f''(\alpha)]$$

$$f[x_n + 0.3f(x_n)] =$$

$$[e_n + 0.3e_n f'(a) + 0.15{e_n}^2 f''(a)]f'(a) + [e_n + 0.3e_n f'(a) + 0.15{e_n}^2 f''(a)]^2\frac{f''(a)}{2!}$$

$$f[x_n + 0.3f(x_n)] = e_n f'(a) + 0.3e_n[f'(a)]^2 + 0.45\quad {e_n}^2 f'(a)f''(a) + \quad {e_n}^2\,\frac{f''(a)}{2!} \quad + 0.045$$

$$e_n{}^2[f'(a)]^2\, f''(a)$$

$$f[x_n + 0.3f(x_n)] - f(x_n) = e_n f'(a) + 0.3e_n[f'(a)]^2 + 0.45e_n{}^2 f'(a)f''(a) + e_n{}^2\,\frac{f''(a)}{2!} + 0.045\, e_n{}^2[f'(a)]^2\, f''(a) - e_n f'(a) - e_n{}^2\,\frac{f''(a)}{2!}$$

$$f[x_n + 0.3f(x_n)] - f(x_n) = 0.3e_n[f'(a)]^2 + 0.45e_n{}^2 f'(a)f''(a) + 0.045\, e_n{}^2\,[f'(a)]^2\, f''(a)$$

Substituting values of $x_{n+1}, x_n, 0.3\,[f(x_n)]^2, f[x_n + 0.3f(x_n)] - f(x_n)]$ in (6), we obtained:

$$e_{n+1} + a = e_n + a - \frac{0.3e_n{}^2\,[f'(a)]^2 + 0.3e_n{}^3\, f'(a)f''(a)}{0.3e_n[f'(a)]^2 + 0.45e_n{}^2 f'(a)f''(a) + 0.045\, e_n{}^2\,[f'(a)]^2\, f''(a)}$$

$$e_{n+1} = e_n - \frac{0.3\, e_n[f'(a)]^2[e_n + e_n{}^2\frac{f''(a)}{f'(a)}]}{0.3\, e_n[f'(a)]^2[1 + 1.5e_n\frac{f''(a)}{f'(a)} + 0.15e_n f''(a)}$$

$$e_{n+1} = e_n - \frac{[e_n + e_n{}^2\frac{f''(a)}{f'(a)}]}{[1 + 1.5e_n\frac{f''(a)}{f'(a)} + 0.15e_n f''(a)]}$$

$$e_{n+1} = e_n - [e_n + e_n{}^2\,\frac{f''(a)}{f'(a)}][1 + 1.5e_n\,\frac{f''(a)}{f'(a)} + 0.15e_n f''(a)]^{-1}$$

$$e_{n+1} = e_n - [e_n + e_n{}^2\,\frac{f''(a)}{f'(a)}][1 - \{1.5e_n\,\frac{f''(a)}{f'(a)} + 0.15e_n f''(a)\} + \{1.5e_n\,\frac{f''(a)}{f'(a)} + 0.15e_n f''(a)\}^2] + \cdots$$

$$e_{n+1} = e_n - [e_n + e_n{}^2\,\frac{f''(a)}{f'(a)}]$$

$$[1 - 1.5e_n\,\frac{f''(a)}{f'(a)} - 0.15e_n f''(a) + 2.25e_n{}^2\left[\frac{f''(a)}{f'(a)}\right]^2 + 0.0225\, e_n{}^2[f''(a)]^2 + 0.45\, e_n{}^2\,\frac{[f''(a)]^2}{f'(a)}]$$

$$e_{n+1} = e_n - [e_n - 1.5e_n{}^2\,\frac{f''(a)}{f'(a)} - 0.15e_n{}^2\, f''(a) + e_n{}^2\,\frac{f''(a)}{f'(a)} + \ldots]$$

$$e_{n+1} = e_n - e_n + 1.5e_n{}^2\,\frac{f''(a)}{f'(a)} + 0.15e_n{}^2\, f''(a) - e_n{}^2\,\frac{f''(a)}{f'(a)} + \ldots$$

$$e_{n+1} = 0.5e_n{}^2\,\frac{f''(a)}{f'(a)} + 0.15\, e_n{}^2\, f''(a)$$

$$e_{n+1} = e_n{}^2[\,0.5\,\frac{f''(a)}{f'(a)} + 0.15\, f''(a)]$$

Since the error term satisfies the quadratic form $e_{n+1} = Ce_n{}^2$, the method has second-order convergence. Thus, the equation defined by (10) exhibits quadratic convergence.

4. EFFICIENCY INDEX

The formula for the efficiency index is given by $E = \omega^{1/\alpha}$ where α represents the number of function evaluations required per iteration, and ω denotes the order of convergence of the technique. In this context, the efficiency index of the modified methodology for solving nonlinear equations is 1.189207115. The efficiency indices of the modified methodology and other methods are presented in Table 1 below.

5. RESULTS AND DISCUSSION

For the performance evaluation of the proposed modified method and some existing methods, several nonlinear equations have been considered, as listed in Table 2 along with their test conditions. The well-known Regula Falsi method, Bisection method, Steffensen's method, and Newton-Raphson method are used to compare the proposed modified technique with practical instances of algebraic and transcendental equation analysis. It has been observed that some existing methods have drawbacks and converge slowly, whereas, in certain cases, the proposed method converges more quickly and has no such limitations. By applying these existing approaches to solve nonlinear functions, both the theoretical impact of the proposed method and its experimental validation can be demonstrated. Based on the results, it can be inferred that the modified algorithm operates more efficiently than previously established approaches. Furthermore, the following data representation justifies the number of iterations required by the improved technique in comparison with existing sectioning methods.

Table 1. Efficiency indices for nonlinear equations and systems of the discussed methods.

Methods	Order of Convergence	Total Evaluations in an Iterations	Efficiency Index
Bisection	1	1	1
Regula Falsi	1	2	1
Proposed Modified Method	2	4	1.189207115
Newton Raphson	2	2	1.4142
Steffensen Method	2	3	1.2311

Table 2. Comparison of iteration counts for different root-finding methods.

Function	Root	Interval	Number of Iteration Required				
			BM	RFM	SM	NRM	PM
$e^x - 5x$	0.259171	[0,0.5]	40	9	8	8	7
$x^3 + 4x - 10$	1.55677326439	[1.5,3]	39	26	23	19	13
$\sin x - x + 1$	1.93456	[0,1.5]	39	7	7	7	4
$x \sin x - 1$	1.11415714084	[1,1.5]	35	10	9	7	7
$xe^x - 1$	0.5671432904	[0,1]	37	23	11	8	7
$x^3 + \ln x$	0.7047094901	[0.5,1]	32	14	7	7	7
$x^3 - 9x + 1$	0.11126415759	[0,1]	38	8	5	5	4
$\cos x - 3x + 1$	0.60710164811	[0.60,0.61]	28	13	12	7	5
$x^3 - x - 1$	1.32471795724	[1,2]	36	28	17	11	11
$x^3 - x - 2$	1.5213797	[1,2]	22	15	8	6	4
$x \log x - 1.2$	2.74064609596	[2,3]	38	11	11	7	6

In this study, we present a modified technique for numerically approximating the roots of nonlinear equations. The proposed method enhances the efficiency and convergence rate of the traditional Bisection and Regula-Falsi methods. Theoretical analysis and convergence results demonstrate that the modified method achieves a convergence rate of order 2, which is faster than the traditional Bisection and Regula-Falsi methods.

We proceed with the interpretation of our numerical methods for approximating solutions to nonlinear equations based on the results obtained. The Regula-Falsi, Bisection, Steffensen, Newton-Raphson, and Modified Proposed Methods are used to solve these problems. Table 2 presents the approximations of roots obtained using these methods for nonlinear algebraic and transcendental equations.

The results indicate that, compared to the Regula-Falsi, Bisection, Steffensen, and Newton-Raphson methods, the modified proposed method yields better results while requiring fewer iterations. Additionally, graphical analysis confirms that the proposed method outperforms the Regula-Falsi, Bisection, Steffensen, and Newton-Raphson techniques. Hence, the modified approach presented in this paper offers a powerful and efficient numerical algorithm for solving nonlinear equations.

6. CONCLUSIONS

An iterative, mathematically integrated approach for obtaining the roots of nonlinear equations has been developed and presented in this work. The proposed technique is a modification of the Bisection and Regula-Falsi methods. After comparing the results of this study with those of the Bisection and Regula-Falsi methods, it can be concluded that the proposed modified technique performs quite effectively. This modified method is free of impediments and rapidly converges to the root. Moreover, compared to the Bisection, Regula-Falsi, Steffensen, and Newton-Raphson methods, the proposed modified approach yields superior results in terms of accuracy and iteration count. However, the computational cost of each iteration in the newly suggested method is slightly higher than that of the Bisection and Regula-Falsi methods.

7. ACKNOWLEDGEMENT

Authors are thankful to University Grant Commission and Guru Gobind Singh Indraprastha University for financial support and research facilities.

8. CONFLICT OF INTEREST

The authors declare no conflict of interest.

9. REFERENCES

1. T.M. Adegoke, G.K. Adegoke, A.M. Yahya, and H.K. Oduwole. Comparative study of some numerical iterations using zero truncated poisson distribution. *Professional Statisticians Society of Nigeria. Proceedings of 2nd International Conference* 2: 313-317 (2018).
2. A.G. Ahmad. Comparative study of bisection and newton-raphson methods of root-finding problems. *International Journal of Mathematics Trends and Technology* 19: 121-129 (2015).
3. J.R. Sharma, S. Kumar, and I.K. Argyros. Development of optimal eight order derivative – free methods for multiple roots of nonlinear equations. *Symmetry* 11: 766 (2019).
4. J.C. Ehiwario and S.O. Aghamie. Comparative study of bisection, newton-raphson and secant methods of root- finding problems. *IOSR Journal of Engineering (IOSRJEN)* 4(4): 1-7 (2014).
5. S. Jamali, Z.A. Kalhoro, A.W. Shaikh, M.S. Chandio, A.O. Rajput, and U.K. Qureshi. Solution of nonlinear models in engineering using a new sixteenth order scheme and their basin of attraction. *VFAST Transactions on Mathematics* 12(1): 1-15 (2024).
6. M. Frontini and F. Sormani. Third-order methods from quadrature formulae for solving systems of nonlinear equations. *Applied Mathematics and Computation* 149: 771-782 (2004).
7. M.A. Noor, K.I. Noor, W.A. Khan, and F. Ahmad. On iterative methods for nonlinear equations. *Applied Mathematics and Computation* 183: 128-133 (2006).
8. R.B. Srivastava and S. Srivastava. Comparison of numerical rate of convergence of bisection, newton-raphson's and secant methods. *Journal of Chemical, Biological and Physical Sciences (JCBPS)* 2(1): 472-479 (2011).
9. O.C. Ebelechukwu and B.O. Johnson, A.I. Michael, and A.T. Fidelis. Comparison of some iterative methods of solving nonlinear equations.

International Journal of Theoretical and Applied Mathematics 4(2): 22-28 (2018).

10. A. Isaac, A. Golbert, and D. Louis. Comparative study of numerical methods for solving non-linear equations using manual computations. *Mathematics Letters* 5(4): 41-46 (2019).
11. R. Behl, A. Cordero, and J.R. Torregrosa. A new higher order optimal derivative free scheme for multiple roots. *Journal of Computational and Applied Mathematics* 404: 113773 (2022).
12. R.G. Gottlieb and B.F. Thompson. Bisected direct quadratic regula-falsi. *Applied Mathematics and Science* 4(15): 709-718 (2010).
13. J.R. Sharma and R.K. Goyal. Fourth order derivative methods for solving nonlinear equations. *International Journal of Computer Mathematics* 83(1): 101-106 (2006).
14. W. Wu and H. Wu. On a class of quadratic convergence iteration formula without derivatives. *Applied Mathematics and Computers* 107: 77-80 (2000).
15. X. Wu, Z. Shen, and X. Jianlin. An improved Regula Falsi method with quadratic convergence of both diameter and point for enclosing simple zeros of non-linear equations. *Applied Mathematics and Computers* 144: 381-8 (2003).
16. V.K. Mamta, V.K. Kukreja, and S. Singh. On some third-order iterative methods for solving nonlinear equations. *Applied Mathematics and Computation* 171: 272-280 (2005).
17. M.A. Noor and F. Ahmad. Numerical comparison of iterative methods for solving nonlinear equations. *Applied Mathematics and Computation* 180: 167-172 (2006).
18. M.A. Noor, F. Ahmad, and S. Javeed. Two-step iterative methods for nonlinear equations. *Applied Mathematics and Computation* 181(2): 1068-1075 (2006).
19. S. Thota and V.K. Srivastav. Interpolation based hybrid algorithm for computing real root of non-linear transcendental functions. *International Journal of Computer Mathematics* 2(11): 729-35 (2014).
20. A. Cordero, H.L. Jose, M. Eulalia, and T.R. Juan. Steffensen type methods for solving nonlinear equations. *Journal of Computational and Applied Mathematics* 236: 3058-3064 (2012).
21. J.B. Dixit (Ed.). Numerical Methods. *University Science Press, New Delhi, India* (2010).
22. B. Ram (Ed.). Numerical Methods. *Pearson Education, India* (2010)
23. J. Naghipoor, S.A. Ahmadian, and A.R. Soheili. An improved regula falsi method for finding simple zeros of nonlinear equations. *Applied Mathematical Sciences* 2(8): 381-386 (2008).
24. S. Shaw and B. Mukhopadhyay. An improved Regula Falsi method for finding simple roots of nonlinear equations. *Applied Mathematics and Computation* 254: 370-374 (2015).
25. V. Kodnyanko. Improved bracketing parabolic method for numerical solution of nonlinear equations. *Applied Mathematics and Computation* 400: 125995 (2021).
26. S. Jamali, Z.A. Kalhoro, A.W. Shaikh, M.S. Chandio, A.O. Rajput, and U.K. Qureshi. A new two-step optimal approach for solution of real-world models and their dynamics. *Journal of Xi'an Shiyou University*, *Natural Science* 19: 1197-120 (2023).
27. P.K. Parida and D.K. Gupta. An improved regula falsi method for enclosing simple zeros of nonlinear equations. *Applied Mathematics and Computation* 177(2): 769-776 (2006).
28. W. Li and J. Chen. An exponential regula falsi method for solving nonlinear equations. *Numerical Algorithms* 41: 327-38 (2006).
29. W. Li and J. Chen. An improved exponential regula falsi methods with quadratic convergence of both diameter and point for solving nonlinear equations. *Applied Numerical Mathematics* 57: 80-88 (2007).
30. U.K. Qureshi, Z.A. Kalhoro, R.A. Malookani, S. Dehraj, S.H. Siyal, and E.A. Buriro. Quadratic convergence iterative algorithms of taylor series for solving nonlinear equations. *Quaid-e-Awam University Research Journal of Engineering Science Technology* 18: 150-156 (2020).
31. C.N. Iwetan, I.A. Fuwape, M.S. Olajide, and R.A. Adenodi. Comparative study of the bisection and newton methods in solving for zero and extremes of a single-variable function. *Journal of the Nigerian Association of Mathematical Physics (NAMP)* 21: 173-176 (2012).
32. G. Dalquist and A. Bjorck (Eds.). Numerical Methods in Scientific Computing. Volume 1. *Society for Industrial and Applied Mathematics, Philadelphia* (2008).
33. A. Golbabai and M. Javidi. A third-order newton type method for nonlinear equations based on modified homotopy perturbation method. *Applied Mathematics and Computation* 191: 199-205 (2007).
34. N.D. Biswa and S. Vadim. A solution of the affine quadratic inverse eigen value problem. *Linear Algebra and it's Applications* 434(7): 1745-1760

(2011).

35. A. Golbabai and M. Javidi. New iterative methods for nonlinear equations by modified homotopy perturbation method. *Applied Mathematics and Computation* 191: 122-127 (2007).
36. C. Chun. Iterative methods improving newtons method by the decomposition method. *Computer and Mathematics with Application* 50: 1559-1568 (2005).
37. C. Solanki, P. Thapliyal, and K. Tomar. Role of bisection method. *International Journal of Computer Applications Technology and Research* 3(8): 535-535 (2014).
38. M. Dowell and D. Jarratt. A modified regula-falsi method for computing the root of an equation. *BIT Numerical Mathematics* 11: 168-174 (1971).
39. M. Frontini and E. Sormani. Modified newton's method with third-order convergence and multiple roots. *Journal of Computational and Applied Mathematics* 156: 345-54 (2003).
40. S. Abbasbandy. Improving newton raphson method for nonlinear equations by modified adomian decomposition method. *Applied Mathematics and Computation* 145: 887-893 (2003).
41. E. Babolian and J. Biazar. Solution of nonlinear equations by adomian decomposition method. *Applied Mathematics and Computation* 132: 167-172 (2002).
42. M. Allame and N. Azad. On Modified Newton Method for Solving a Nonlinear Algebraic Equations by Mid-Point. *World Applied Sciences Journal* 17(12): 1546-1548 (2012).
43. S. Hussain, V.K. Srivastav, and S. Thota. Assessment of interpolation methods for solving the real-life problem. *International Journal of Mathematical Sciences and Applications* 5(1): 91-95 (2015).

Proceedings of the Pakistan Academy of Sciences: A Physical and Computational Sciences 62(1): 21-30 (2025)
Copyright © Pakistan Academy of Sciences
ISSN (Print): 2518-4245; ISSN (Online): 2518-4253
http://doi.org/10.53560/PPASA(62-1)874

Pakistan Academy of Sciences

Research Article

Entropy Generation Analysis for the Peristaltic Motion of Ree-Eyring Fluid through a Porous Symmetric Channel under Slip Constraints

Zaheer Abbas, Muhammad Yousuf Rafiq, Salita Yaqoob, and Hafiz Shahzad*

Department of Mathematics, the Islamia University of Bahawalpur, 63100, Bahawalpur, Pakistan

Abstract: Peristaltic-driven flows play a critical role in many natural biological processes and have inspired numerous applications in engineering, medicine, and environmental technology. By mimicking the efficient movement and control of peristaltic, scientists and engineers can develop innovative solutions for a wide range of challenges. Therefore, this article delves into the peristaltic flow of electrically conducting Ree-Eyring fluid in a non-uniform symmetric conduit with entropy generation. Slip constraints and radiative impacts are also deliberated. The lubrication theory hypothesis is utilized to compress the normalized equations. Closed-form outcomes are derived and exhibited graphically to depict the distributions of velocity, entropy generation, temperature, and pressure optimization. The outcomes of this investigation showed that the liquid velocity is demoted by improving the Ree-Eyring and slip parameters. Further, the liquid temperature is boosted by augmenting the values of the Ree-Eyring fluid parameter and Brinkman number.

Keywords: Peristaltic Flow, Slip Conditions, Ree-Eyring Fluid, Entropy Generation, Thermal Radiation, Exact Solution.

1. INTRODUCTION

Peristalsis insinuates the synchronized, periodic contraction and relaxation of muscles responsible for propelling constituents through tubular organs like the esophagus, stomach, intestines, or various segments of the digestive system. This elaboration is essential for moving food, liquids, and other substances throughout the gastrointestinal tract. Within the digestive system, peristalsis aids in transporting ingested material from one segment to another, thereby facilitating digestion and absorption processes. Peristalsis is a process that involves muscle contractions creating a wave-like motion to push the contents forward. It helps move swallowed food from the mouth to the stomach in the esophagus. This process occurs mechanically and involuntarily, without conscious effort. The autonomic nervous system plays a crucial role in regulating peristalsis to ensure that it happens in a coordinated and efficient manner. The mechanical properties of peristalsis were first studied by Latham [1]. The movement of fluids by a peristaltic pump was examined in this work. In a non-uniform conduit, Vaidya *et al.* [2] discovered the stimulus of viscosity and heat conductivity fluctuations on the peristaltic behavior of Rabinowitsch liquid while considering convective surface conditions and wall characteristics. The peristaltic passage has been extensively studied, with several studies examining hypothetical and applied features. In the entropy generation study, Akbar and Abbasi [3] observed at the consequences of mixed convection, thermophoresis, variable viscosity, Brownian motion, and peristaltic-driven nanofluid movement in an asymmetric channel. The diffusion impacts on the blood flow of nanomaterials in an asymmetric conduit with the lubrication hypothesis were studied by Asha and Sunitha [4]. Rafiq and Abbas [5] researched into the results of heat radiation and viscous dissipation on the peristaltic flow of Rabinowitsch liquid in an unevenly sloped conduit. Through the use of a lubrication hypothesis, the influences of velocity slip and entropy production on the MHD peristaltic flow of an incompressible fluid in a diverging duct were predicted by Abbas *et*

Received: February 2024; Revised: February 2025; Accepted: March 2025

* Corresponding Author: Hafiz Shahzad <shahzad.gulzarr@gmail.com>

al. [6]. Using Rosseland's approximation, Farooq and Hussain [7] discussed the radiative blood flow of Williamson liquid over the esophagus. Priam and Nasrin [8] deliberated the thermally radiative peristaltic movement of time-dependent Casson liquid over a conduit having sinusoidal sides. Devakar *et al.* [9] provided a description of how a magnetic field affects the peristaltic activity of a non-Newtonian liquid inside an endoscope. Nadeem *et al.* [10] acquired critical effects for the flow fields by scrutinizing the sinusoidal flow of viscous liquid in an elliptic conduit. Numerous substantial studies concerning peristaltic flow in diverse geometries have been deliberated in previous studies [11-15].

Numerous models have been established to illustrate the comportment of non-Newtonian liquids due to their widespread usage in a variety of sectors, including engineering and industry. The Ree-Eyring model is one such model that is used in rheology to clarify the flow performance of non-Newtonian liquids, particularly those that include viscoelastic characteristics. This model works very well for relating the performance of biological liquids, polymer solutions, and other complicated materials where shear-thinning and viscoelasticity are important. The performance of Ree-Eyring liquids in several settings has been examined by numerous researchers. A general theory of non-Newtonian flow is established on Eyring's theory of rate progressions in Glasstone *et al.* [16]. After some time, this theory has been developed by Ree and Eyring [17]. Bou-Chakra *et al.* [18] used the Ree-Eyring theory to scrutinize the effects of the heterogeneous flow from coated layer surfaces on the frictional reaction and the structure of molecules in the interface region. In their study of the flow of Ree-Eyring liquid between two infinitely matching plates, Ramesh and Eytoo [19] took into account magnetic fields, radiation, heat transfer, slip boundary conditions, and porous materials. While velocity falls as the Hartmann number grows, their study revealed that temperature upsurges with greater Ree-Eyring liquid, temperature, radiation, and slip parameters. Consuming the Cattaneo–Christov model of heat movement, Abbas *et al.* [20] scrutinized the behavior of an electrically conducting Eyring–Powell liquid in a semipermeable bent conduit. Al-Mdallal *et al.* [21] scrutinized the Ree-Eyring liquid move between two stretchy turning disks packed with nanoparticles using water-base fluid by using the Runge-Kutta-Felberg technique. Tanveer and Malik [22] examined the impact of MHD and nanoparticles in a conduit using the Ree-Eyring model as a base fluid. In order to get mathematical formulas for velocity profiles and other pertinent factors, they used the lubrication technique. Rao *et al.* [23] examined the radiative characteristics of the dissipative bioconvective movement of Ree-Eyring NF over a sloping plate. Shah *et al.* [24] analyzed heat transmission properties, considering high thermal resistance and including viscous dissipation, using the Cattaneo-Christov model for Ree-Eyring NF surge across a widening sheet. The two-wave sinusoidal cilia beating inside a tubular conduit exhibit peristaltic rheology, as described by Turkyilmazoglu [25].

Entropy, which is widely used to describe the degree of disorder in a system, is a property of an irretrievable method in which the heat energy produced cannot be transformed into productive activity. Several variables, such as Joule heating, viscous dissipation, and sudden thermal radiation, affect this process. Bejan [26] was one of the pioneers in identifying entropy generation in heat transformation exploration. Akbar [27] observed elevated entropy summaries near a vertical duct while studying the peristaltic behavior of a suspension nanofluid containing carbon nanotubes (CNTs). Rashidi *et al.* [28] scrutinized entropy in peristaltically stimulated blood circulation under the influence of Lorentz force, disregarding inertial effects. Asha and Deepa [29] investigated the peristaltic circulation of blood, considered as a magneto-micropolar liquid, in a non-uniform conduit, focusing on the influences of heat radiation and entropy. Bibi and Xu [30] modeled the peristaltic flow of Jeffrey nanofluid in a symmetric conduit influenced by a magnetic field, demonstrating entropy control through various parameter estimations. The study addresses endoscopic and homogeneous-heterogeneous effects in the magnetohydrodynamic peristalsis of Ree-Eyring liquid by Hayat *et al.* [31]. Rajashekhar *et al.* [32] studied the peristaltic flow of a Ree–Eyring liquid over a uniform compliant duct, incorporating the impacts of variable viscosity and thermal conductivity in their modeling. Balachandra *et al.* [33] improved a model that includes variations in viscosity and thermal conductivity, which play a crucial role in scrutinizing blood moves in tapered arteries Shoaib *et al.* [34] explored the Optimization of entropy generation in the dissipative surge of a

Ree-Eyring liquid model, incorporating a quartic autocatalytic chemical reaction between two rotating disks. The study utilized an artificial neural systems model, which was back-propagated using the Bayesian Regularization procedure. Zafar *et al.* [35] recently studied entropy creation in the Darcy-Forchheimer Ree-Eyring nanoparticles with bioconvection flow over an elastic surface, providing a detailed exploration of the topic. Several key studies relevant to this investigation have been conducted previously [36-41].

This work covers the noted research gap and tackles real-world applications by the features of entropy production that occur when Ree-Eyring fluid peristaltically moves within a horizontal symmetric divergent channel while taking viscous and thermally radiative dissipation into consideration. Analyzing the risk of cardiac illnesses and studying hemodynamics need an understanding of how blood circulates via a horizontal symmetric diverging channel. Nonetheless, since the governing mathematical equations are extremely nonlinear, such investigations are intrinsically complicated. Ree-Eyring fluid peristaltically moves within a horizontal symmetric divergent channel, exhibit superior viscous and thermally radiative dissipation, rendering them extremely pertinent to applications in biomedicine. The complexity of the equations governing the movement of the Ree-Eyring fluid is reduced by utilizing the lubrication approximation. These results are especially important for designing curved geometries in medical implants and flow control devices. In light of this, the main goal of this research is to examine how Ree-Eyring fluid behaves as it peristaltically travels through a horizontally symmetric diverging channel. Approximate findings for heat transfer, pressure gradient, and velocity are obtained using the perturbation approach. To examine the changes in various stream characteristics under a range of important circumstances, graphical representations are used. This study is highly relevant to endoscopy, an essential diagnostic instrument for assessing the condition of internal organs. Additionally, understanding the variations in pressure gradients is crucial for regulating flow rates, especially during the insertion of catheters into arteries. Using 2D graphs, the impacts of important factors on temperature distribution and axial velocity are thoroughly analyzed, and Table 1 highlights the novel aspects of the problem.

2. MATHEMATICAL ANALYSIS

Consider the two-dimensional thermally radiative flow of Ree-Eyring fluid through a symmetric channel having wavy boundaries occupied by a porous medium. The generated flow is peristaltic. The mathematical expression in Equation (1) describes the vertical margins of the conduit [28].

$$H(\bar{x},\bar{t}) = \bar{a}\, sin \frac{2\pi}{\lambda}(\bar{x} - \bar{c}\bar{t}) + b(\bar{x}) \tag{1}$$

where $b(\bar{x}) = b_0 + K_0\bar{x}$ and $K_0 \ll 1$ is constant and b_0 indicates the semi-width at the cove of the irregular conduit, b indicates semi-width as a role of axial distance $\bar{x}$, $\bar{a}$ indicates the amplitude of the peristaltic wave, λ indicates the wavelength of the peristaltic wave, and $\bar{t}$ indicates time as shown in Figure 1.

Table 1. Novel aspects of the present problem.

Ref. No.	**[3]**	**[34]**	**[28]**	**[38]**	**Present**
Peristaltic Flow	✓	✓	✓	✓	✓
Ree-Eyring Fluid	×	✓	✓	✓	✓
Entropy generation	✓	×	✓	✓	✓
Thermal radiation	×	×	×	×	✓
Slip Conditions	×	✓	×	×	✓
Porosity	×	×	×	×	✓

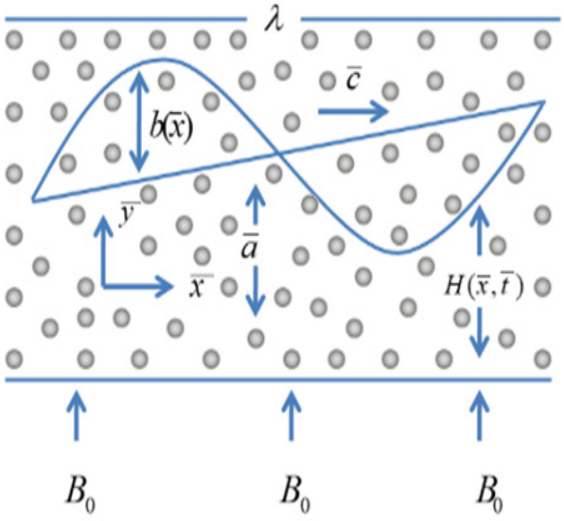

Fig. 1. Horizontal wavy porous channel.

The following Equations define the physical description of the current problems [28, 34, 38]:

$$\frac{\partial \bar{v}}{\partial \bar{y}} + \frac{\partial \bar{u}}{\partial \bar{x}} = 0 \tag{2}$$

$$\rho\left[\frac{\partial \bar{u}}{\partial \bar{t}} + \bar{v}\frac{\partial \bar{u}}{\partial \bar{y}} + \bar{u}\frac{\partial \bar{u}}{\partial \bar{x}}\right] = -\frac{\partial \bar{p}}{\partial \bar{x}} + \frac{\partial}{\partial \bar{x}}\tau_{\bar{x}\bar{x}} + \frac{\partial}{\partial \bar{y}}\tau_{\bar{x}\bar{y}} - \frac{\mu}{k}\bar{u} - \sigma B_0^2 \bar{u} \tag{3}$$

$$\rho\left[\frac{\partial \bar{v}}{\partial \bar{t}} + \bar{v}\frac{\partial \bar{v}}{\partial \bar{y}} + \bar{u}\frac{\partial \bar{v}}{\partial \bar{x}}\right] = -\frac{\partial \bar{p}}{\partial \bar{y}} + \frac{\partial}{\partial \bar{x}}\tau_{\bar{y}\bar{x}} + \frac{\partial}{\partial \bar{y}}\tau_{\bar{y}\bar{y}} - \sigma B_0^2 \bar{v} - \bar{v}\frac{\mu}{k} \tag{4}$$

$$C_p\left[\frac{\partial T}{\partial \bar{t}} + \bar{v}\frac{\partial T}{\partial \bar{y}} + \bar{u}\frac{\partial T}{\partial \bar{x}}\right] = \frac{k}{\rho}\left(\frac{\partial^2 T}{\partial \bar{x}^2} + \frac{\partial^2 T}{\partial \bar{y}^2}\right) - \frac{\partial q_r}{\partial y} + \frac{\tau_{\bar{x}\bar{y}}}{\rho}\left(\frac{\partial \bar{u}}{\partial \bar{y}}\right) \tag{5}$$

The stress tensor of the Ree-Eyring liquid model is:

$$\tau_{ij} = \mu\frac{\partial \bar{V}_i}{\partial \bar{x}_j} + \frac{1}{\bar{B}} sinh^{-1}\left(\frac{1}{\bar{C}}\frac{\partial \bar{V}_i}{\partial \bar{x}_j}\right) \tag{6}$$

As $s\imath n\bar{h}^{-1} x = \bar{x}$ for $|\bar{x}| \leq 1$, the upstairs Equation can be rewritten as:

$$\tau_{ij} = \mu\frac{\partial \bar{V}_i}{\partial \bar{x}_j} + \frac{1}{\bar{B}}\left(\frac{1}{\bar{C}}\frac{\partial \bar{V}_i}{\partial \bar{x}_j}\right) \tag{7}$$

where, $\bar{B}$ and $\bar{C}$ represent the material coefficients and σ denotes the electrical conductivity. The dimensionless variables are:

$$x = \frac{\bar{x}}{\lambda}, \quad y = \frac{\bar{y}}{b_0}, \quad u = \frac{\bar{u}}{c}, \quad v = \frac{\bar{v}}{\delta c}, \quad t = \frac{c\bar{t}}{\lambda}, \quad \delta = \frac{b_0}{\lambda}, \quad h = \frac{H}{b_0},$$

$$p = \frac{b_0 \bar{p}}{\lambda \mu c}, \phi = \frac{\bar{a}}{b_0}, \quad Re = \frac{\rho c b_0}{\mu}, \quad M = \sqrt{\frac{B_0^2 b_0^2 \sigma}{\mu}}, \quad q_r = -\frac{4\sigma^*}{3k^*}\frac{\partial T^4}{\partial \tilde{y}},$$

$$\theta = \frac{T - T_0}{T_1 - T_0}, \quad Pr = \frac{\nu C_p \rho}{k}, Ec = \frac{c^2}{C_p(T_1 - T_0)}, B_r = Pr\, Ec, \quad \zeta = \frac{1}{\mu \bar{B}\, \bar{C}}$$

Where, δ stands for wave number, ϕ stands for amplitude ratio, θ stands for non-dimensional temperature, Re stands for Reynolds number, M stands for Hartmann number, q_r is the radiative heat flux, Ec stands for Eckert number, Pr represents for Prandtl number, B_r stands for Brinkmann number, and ζ stands for Ree-Eyring fluid parameter.

The dimensionless form of Equations (2), (3), (4), and (5) are:

$$Re\,\delta\left(\frac{\partial u}{\partial t} + u\frac{\partial u}{\partial x} + v\frac{\partial u}{\partial y}\right) + \frac{\partial p}{\partial x} = (1+\zeta)\left(\delta^2\frac{\partial^2 u}{\partial x^2} + \frac{\partial^2 u}{\partial y^2}\right) - M^2 u - Dau\; Re\,\delta\left(\frac{\partial u}{\partial t} + u\frac{\partial u}{\partial x} + v\frac{\partial u}{\partial y}\right) + \frac{\partial p}{\partial x} = (1+\zeta)\left(\delta^2\frac{\partial^2 u}{\partial x^2} + \frac{\partial^2 u}{\partial y^2}\right) - M^2 u - Dau \tag{8}$$

$$Re\,\delta^3\left(\frac{\partial v}{\partial t} + u\frac{\partial v}{\partial x} + v\frac{\partial v}{\partial y}\right) + \frac{\partial p}{\partial y} = \delta^2(1+\zeta)\left(\delta^2\frac{\partial^2 v}{\partial x^2} + \frac{\partial^2 v}{\partial y^2}\right) - \delta^2 M^2 v - Dau\; Re\,\delta^3\left(\frac{\partial v}{\partial t} + u\frac{\partial v}{\partial x} + v\frac{\partial v}{\partial y}\right) + \frac{\partial p}{\partial y} = \delta^2(1+\zeta)\left(\delta^2\frac{\partial^2 v}{\partial x^2} + \frac{\partial^2 v}{\partial y^2}\right) - \delta^2 M^2 v - Dau \tag{9}$$

$$RePr\,\delta\left(\frac{\partial\theta}{\partial t}+v\frac{\partial\theta}{\partial y}+u\frac{\partial\theta}{\partial x}\right)=\left(\frac{\partial^2\theta}{\partial y^2}+\delta^2\frac{\partial^2\theta}{\partial x^2}\right)+Ec\,Pr(1+\zeta)\left(\frac{\partial u}{\partial y}\right)^2+Rd\frac{\partial^2\theta}{\partial y^2}RePr\,\delta\left(\frac{\partial\theta}{\partial t}+v\frac{\partial\theta}{\partial y}+u\frac{\partial\theta}{\partial x}\right)=\left(\frac{\partial^2\theta}{\partial y^2}+\delta^2\frac{\partial^2\theta}{\partial x^2}\right)+Ec\,Pr(1+\zeta)\left(\frac{\partial u}{\partial y}\right)^2+Rd\frac{\partial^2\theta}{\partial y^2} \tag{10}$$

Per lubrication theory, Equations (8-10) can be reformulated as:

$$\frac{\partial p}{\partial x}=(1+\zeta)\frac{\partial^2 u}{\partial y^2}-M^2u-\frac{1}{Da}u \tag{11}$$

$$\frac{\partial p}{\partial y}=0 \tag{12}$$

$$\frac{\partial^2\theta}{\partial y^2}=-B_r(1+\zeta)\left(\frac{\partial u}{\partial y}\right)^2-Rd\frac{\partial^2\theta}{\partial y^2} \tag{13}$$

The boundary constraints can be described as:

$$\frac{\partial u}{\partial y}=0,\theta=0,aty=0 \tag{14}$$

$$\beta(1+\zeta)\frac{\partial u}{\partial y}+u=0,\theta=1,aty=h \tag{15}$$

2.1. Entropy Generation

The entropy generation can be described as:

$$s_{Gen}^{m}=\frac{\kappa}{T_0^2}\left(\frac{\partial T}{\partial\tilde{y}}\right)^2+\frac{1}{T_0}\left(\mu\tau_{\tilde{x}\tilde{y}}\left(\frac{\partial\tilde{u}}{\partial\tilde{y}}\right)+\sigma B_0^2\tilde{u}^2\right) \tag{16}$$

The Equation (16) defines entropy generation through four terms, accounting for thermal heat transfer irreversibility, the magnetic field and viscous dissipation. In its dimensionless form, Equation (16) expresses the ratio of volumetric entropy generation, s_{Gen}^{m}, to the characteristic entropy generation, s_{G}^{m}.
In the Equation (16), entropy generation is defined using four terms, accounting for thermal heat transfer irreversibility, the magnetic field and viscous dissipation. The dimensionless form of Equation (16) are:

$$N_s=\frac{s_{Gen}^{'''}}{s_G}=(1+R)\left(\frac{\partial\theta}{\partial y}\right)^2+\Lambda B_r(1+\zeta)\left(\frac{\partial u}{\partial y}\right)^2+\Lambda B_r M^2u^2 \tag{17}$$

2.2. Solution Procedure

The result of Equations (13) and (14) with boundary conditions of Equation (15), we have [15, 25]:

$$u=\frac{1}{M^2}\frac{dp}{dx}\left[-1+Cosh\left(\frac{My}{\sqrt{1+\zeta}}\right)Sech\left(\frac{hM}{\sqrt{1+\zeta}}\right)\right] \tag{18}$$

$$\theta=\frac{1}{8hM^4}\begin{bmatrix}4M^4y-B_rP\frac{dp^2}{dx}(-1+2hM^2y-\zeta)(h-y)+y\left(4M^4+B_r\frac{dp^2}{dx}(1+\zeta)\right)\\ C\,osh\left(\frac{2hM}{\sqrt{1+\zeta}}\right)-B_rh\frac{dp^2}{dx}(1+\zeta)\,Cosh\left(\frac{2My}{\sqrt{1+\zeta}}\right)\left\{Sech\left(\frac{hM}{\sqrt{1+\zeta}}\right)^2\right\}\end{bmatrix} \tag{19}$$

The pressure gradient term obtained through instantaneous mean flow rate which is characterized as:

$$Q=-\frac{1}{M^3}hM\frac{dp}{dx}+\frac{dp}{dx}\sqrt{1+\zeta}\,Tanh\left(\frac{hM}{\sqrt{1+\zeta}}\right) \tag{20}$$

$$\frac{dp}{dx}=-\frac{M^3Q}{hM-\sqrt{1+\zeta\,Tanh\left(\frac{hM}{\sqrt{1+\zeta}}\right)}} \tag{21}$$

3. RESULTS AND DISCUSSION

This section provides a graphical analysis of the impact of various parameters on pressure, velocity, heat transfer, and entropy generation. The solution and graphics of the system can be found by consuming the DSolve command in Mathematica. A valuable approach to verifying the validity of the current findings is to conduct a comparative analysis with the previous study [38]. The accuracy and reliability of the present results, as illustrated in the graphs, are validated by the strong agreement between this study's findings and existing literature. Figure 2(a) shows how the velocity distribution is affected by the magnetic field parameter “*M*”, depicting a reduction in the central region while increasing near the boundaries. Figure 2(b) illustrates the impact of the Ree-Eyring fluid parameter “ζ” on velocity, potentially emphasizing non-Newtonian characteristics. Figure 2(c) demonstrates how the porous medium parameter “*S*” affects the flow, highlighting resistance due to the porous structure. Figure 2(d) elucidates the effect of the slip parameter “β”, showcasing variations in boundary behavior and improved flow due to slip conditions.

Figure 3(a) depicts the variation of pressure with wavelength “ΔP_{λ}”, showing an overall increase in pressure as “ΔP_{λ}” rises. Figure 3(b) examine the influence of the Ree-Eyring liquid parameter “ζ” on pressure, illustrating a noticeable increase in pressure with higher “ζ” values due to non-Newtonian effects. Figure 3(c) explore the role of the porous medium parameter “*s*”, revealing that increasing “*S*” leads to a reduction in pressure, indicating higher resistance to flow. Figure 3(d) investigate the impact of the slip parameter “*β*” and the Hartmann number “*M*” on pressure, highlighting a decrease in pressure for increasing “*β*”, while a higher “*M*” results in increased pressure due to electromagnetic effects. The results of the present study are in good agreement with the results available in a previous study [21].

Figure 4(a) illustrates the upshot of the magnetic field parameter “*M*” on the temperature distribution, showing variations in heat distribution due to electromagnetic forces. Figure 4(b) shows the effect of the Ree-Eyring liquid parameter “ζ” on the temperature, identifying its role in thermal diffusion. Figure 4(c) explains the behavior of the temperature profile concerning the radiation parameter “*R*”, highlighting its impact on heat transfer mechanisms. Figure 4(d) demonstrates how the Brinkman number “*Br*” affects temperature variation, emphasizing its significance in convective heat transfer. Thus, we come to know that an increment in the “*Br*” raises the heat augment in the system. A similar behavior is observed by Rafiq *et al.* [5].

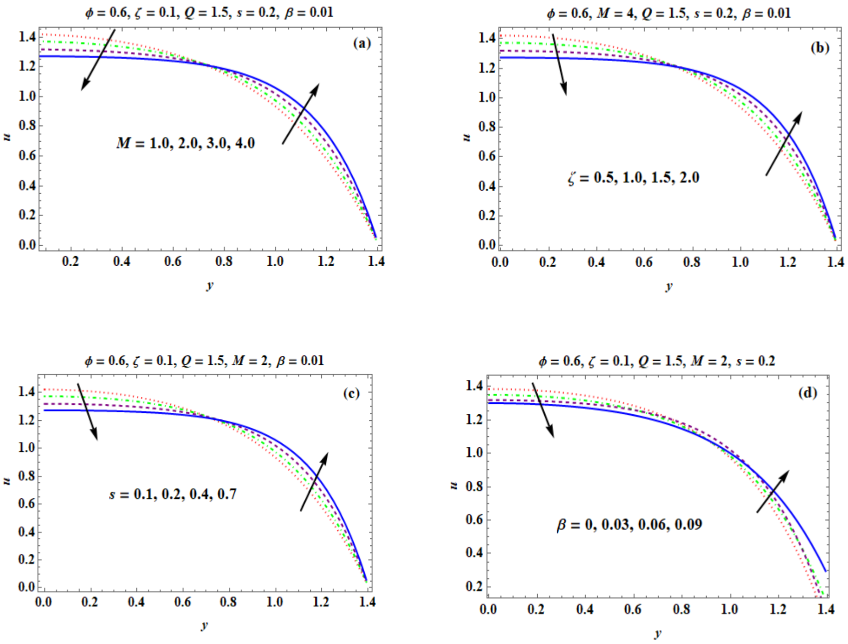

Fig. 2. Alteration of u for variation of M (a), ζ (b), s (c), and β (d).

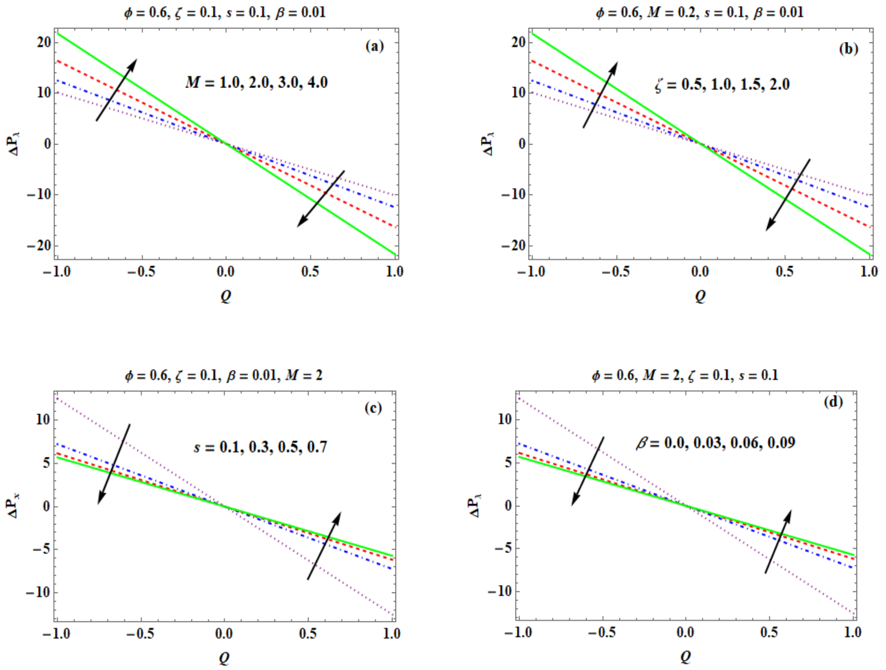

Fig. 3. Alteration of ΔP_λ for variation of M (a), ζ (b), s (c), and β (d).

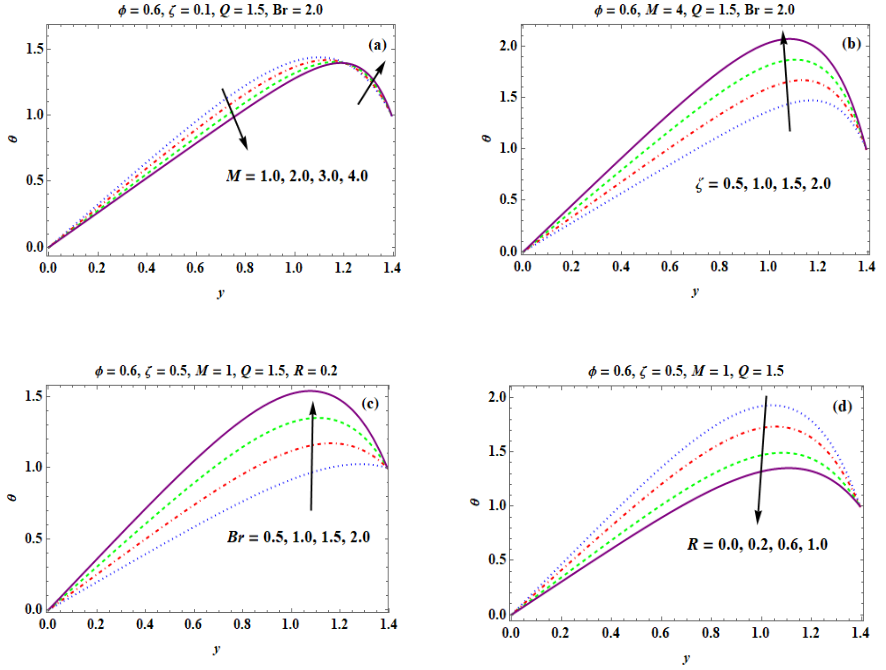

Fig. 4. Alteration of θ for variation of M (a), ζ (b), Br (c), and R (d).

Figure 5(a) demonstrates how the entropy generation changes with variations in the Ree-Eyring parameter "ζ". A decreasing trend is observed, indicating that increasing "ζ" reduces entropy production in the system. Figure 5(b) elucidates the outcome of the Brinkman number "*Br*" on entropy generation. The results reveal a continuous decline, suggesting that increasing viscous dissipation reduces entropy generation. Figure 5(c) shows the impact of the Hartmann number "*M*". As M increases, entropy generation also rises, which aligns with findings by Shoaib *et al.* [35], indicating that the presence of a stronger magnetic field improves irreversibility. Figure 5(d) displays the upshot of the wave number "*δ*" on entropy generation. A continuous upsurge in

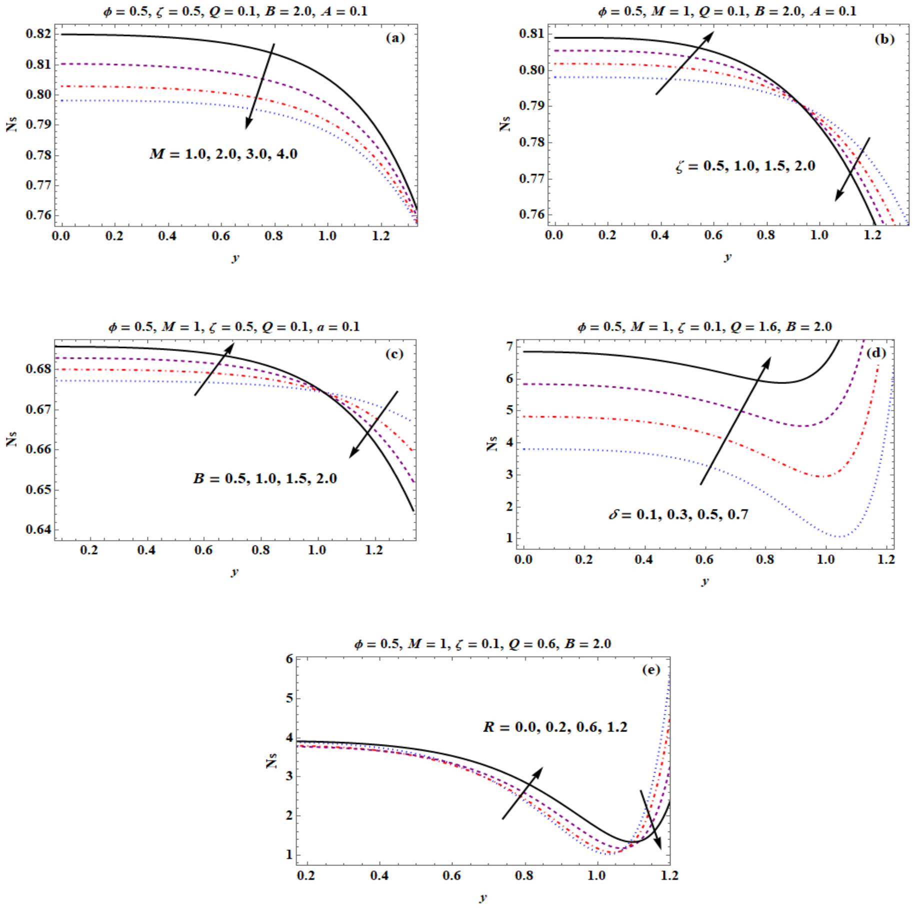

Fig. 5. Alteration of Ns for variation of M (a), ζ (b), Br (c), δ (d), and R (e).

entropy generation is observed as "δ" increases, highlighting the influence of wave characteristics on system disorder. Figure 5(e) shows the behavior of thermal radiation "R". Initially, entropy generation increases, but after reaching a threshold value (~1.1), it starts to decline. This non-monotonic trend suggests that thermal radiation has a complex effect on entropy generation.

4. CONCLUSIONS

This research investigates the behavior of Ree-Eyring liquid within a permeable medium in a symmetric tapered conduit, emphasizing the influence of thermal boundary conditions on the temperature profile and entropy generation. This study enhances our understanding of fluid flow behavior in a symmetric tapered conduit, paving the way for optimizing flow dynamics and reducing resistance. Future research can expand on this work by incorporating additional models such as the Ree-Eyring fluid model and the Oldroyd-B fluid model, along with factors like mixed convection and bioconvection. The analysis reveals that fluid velocity diminishes as the Ree-Eyring and slip parameters increase. Additionally, pressure variations show that the Ree-Eyring parameter and Hartmann number lead to a rise in the retrograde region, while a contrasting trend is observed in the co-pumping region. The Brinkman number significantly influences the system, as its increase results in greater heat inflow, elevating the liquid temperature. The temperature is also shown to rise with growing values of both the Brinkman number and thermal radiation. Furthermore, entropy generation is particularly pronounced near the channel boundaries, intensifying with higher wave number and thermal radiation values. These findings are supported by graphical representations that highlight the effects of the evolving parameters on the system.

5. ACKNOWLEDGEMENTS

We are thankful to The Islamia University of Bahawalpur for providing the research facilities to conduct this work.

6. CONFLICT OF INTEREST

The authors declare no conflict of interest.

7. REFERENCES

1. T.W. Latham. Fluid motions in a peristaltic pump. Doctoral Dissertation. *Massachusetts Institute of Technology, USA* (1966).
2. H. Vaidya, C. Rajashekhar, M. Gudekote, K.V. Prasad, O.D. Makinde, and S. Sreenadh. Peristaltic motion of non-newtonian fluid with variable liquid properties in a convectively heated nonuniform tube: Rabinowitsch fluid model. *Journal of Enhanced Heat Transfer* 26(3): 277-294 (2019).
3. Y. Akbar and F.M. Abbasi. Impact of variable viscosity on peristaltic motion with entropy generation. *International Communications in Heat and Mass Transfer* 118: 104826 (2020).
4. S.K. Asha and G. Sunitha. Thermal radiation and Hall effects on peristaltic blood flow with double diffusion in the presence of nanoparticles. *Case Studies in Thermal Engineering* 17: 100560 (2020).
5. M.Y. Rafiq and Z. Abbas. Impacts of viscous dissipation and thermal radiation on Rabinowitsch fluid model obeying peristaltic mechanism with wall properties. *Arabian Journal for Science and Engineering* 46: 12155-12163 (2021).
6. Z. Abbas, M.Y. Rafiq, A.S. Alshomrani, and M.Z. Ullah. Analysis of entropy generation on peristaltic phenomena of MHD slip flow of viscous fluid in a diverging tube. *Case Studies in Thermal Engineering* 23: 100817 (2021).
7. N. Farooq and A. Hussain. Peristaltic analysis of Williamson blood flow model with solar biomimetic pump. *International Communications in Heat and Mass Transfer* 138: 106305 (2022).
8. S.S. Priam and R. Nasrin. Numerical appraisal of time-dependent peristaltic duct flow using Casson fluid. *International Journal of Mechanical Sciences* 233: 107676 (2022).
9. M. Devakar, K. Ramesh, and K. Vajravelu. Magnetohydrodynamic effects on the peristaltic flow of couple stress fluid in an inclined tube with endoscope. *Journal of Computational Mathematics and Data Science* 2: 100025 (2022).
10. S. Nadeem, S. Akhtar, F.M. Alharbi, S. Saleem, and A. Issakhov. Analysis of heat and mass transfer on the peristaltic flow in a duct with sinusoidal walls: Exact solutions of coupled PDEs. *Alexandria Engineering Journal* 61(5): 4107-4117 (2022).
11. Z. Abbas, A. Shakeel, M.Y. Rafiq, S. Khaliq, J. Hasnain, and A. Nadeem. Rheology of peristaltic flow in couple stress fluid in an inclined tube: Heat and mass transfer analysis. *Advances in Mechanical Engineering* 14(11): 1-14 (2022).
12. S. Akhtar, S. Almutairi, and S. Nadeem. Impact of heat and mass transfer on the Peristaltic flow of non-Newtonian Casson fluid inside an elliptic conduit: Exact solutions through novel technique. *Chinese Journal of Physics* 78: 194-206 (2022).
13. N.M. Hafez, A.M. Abd-Alla, and T.M.N. Metwaly. Influences of rotation and mass and heat transfer on MHD peristaltic transport of Casson fluid through inclined plane. *Alexandria Engineering Journal* 68: 665-692 (2023).
14. J. Iqbal, F.M. Abbasi, M. Alkinidri, and H. Alahmadi. Heat and mass transfer analysis for MHD bioconvection peristaltic motion of Powell-Eyring nanofluid with variable thermal characteristics. *Case Studies in Thermal Engineering* 43: 102692 (2023).
15. M. Turkyilmazoglu. Corrections to long wavelength approximation of peristalsis viscous fluid flow within a wavy channel. *Chinese Journal of Physics* 89: 340-354 (2024).
16. S. Glasstone, K.J. Laidler, and H. Eyring (Eds.). The theory of rate processes: the kinetics of chemical reactions, viscosity, diffusion and electrochemical phenomena. *McGraw Hill, New York, USA* (1941).
17. T. Ree and H. Eyring. Theory of non-newtonian flow. I. solid plastic system. *Journal of Applied Physics* 26(7): 793-800 (1955).
18. E. Bou-Chakra, J. Cayer-Barrioz, D. Mazuyer, F. Jarnias, and A. Bouffet. A non-Newtonian model based on Ree-Eyring theory and surface effect to predict friction in elastohydrodynamic lubrication. *Tribology International* 43(9): 1674-1682 (2010).
19. K. Ramesh and S.A. Eytoo. Effects of thermal radiation and magnetohydrodynamics on Ree-Eyring fluid flows through porous medium with slip boundary conditions. *Multidiscipline Modeling in Materials and Structures* 15(2): 492-507 (2018).
20. Z. Abbas, M.Y. Rafiq, and M. Naveed. Analysis of Eyring-Powell liquid flow in curved channel with Cattaneo-Christov heat flux model. *Journal of the Brazilian Society of Mechanical Sciences and Engineering* 40(1): 390 (2018).
21. Q.M. Al-Mdallal, A. Renuka, M. Muthtamilselvan, and B. Abdalla. Ree-Eyring fluid flow of Cu-water nanofluid between infinite spinning disks with an effect of thermal radiation. *Ain Shams Engineering Journal* 12(3): 2947-2956 (2021).
22. A. Tanveer and M.Y. Malik. Slip and porosity

effects on peristalsis of MHD Ree-Eyring nanofluid in curved geometry. *Ain Shams Engineering Journal* 12(1): 955-968 (2021).

23. D.P.C. Rao, S. Thiagarajan, and V.S. Kumar. Significance of quadratic thermal radiation on the bioconvective flow of Ree-Eyring fluid through an inclined plate with viscous dissipation and chemical reaction: Non-Fourier heat flux model. *International Journal of Ambient Energy* 43(1): 6436-6448 (2022).
24. Z. Shah, N. Vrinceanu, M. Rooman, W. Deebani, and M. Shutaywi. Mathematical modelling of Ree-eyring nanofluid using Koo-kleinstreuer and Cattaneo-Christov models on chemically reactive AA 7072-AA 7075 alloys over a magnetic dipole stretching surface. *Coatings* 12(3): 391 (2022).
25. M. Turkyilmazoglu. Long wavelength analysis amendment on the cilia beating assisted peristalsis in a tube. *Theoretical and Computational Fluid Dynamics* 39(1): 3 (2025).
26. A. Bejan. A study of entropy generation in fundamental convective heat transfer. *Journal of Heat Transfer* 101(4): 718-725 (1979).
27. N.S. Akbar. Entropy generation analysis for a CNT suspension nanofluid in plumb ducts with peristalsis. *Entropy* 17(3): 1411-1424 (2015).
28. M.M. Rashidi, M.M. Bhatti, M.A. Abbas and M.E.S. Ali. Entropy generation on MHD blood flow of nanofluid due to peristaltic waves. *Entropy* 18(4): 117 (2016).
29. S.K. Asha and C.K. Deepa. Entropy generation for peristaltic blood flow of a magneto-micropolar fluid with thermal radiation in a tapered asymmetric channel. *Results in Engineering* 3: 100024 (2019).
30. A. Bibi and H. Xu. Entropy generation analysis of peristaltic flow and heat transfer of a Jeffery nanofluid in a horizontal channel under magnetic environment. *Mathematical Problems in Engineering* 2019: 2405986 (2019).
31. T. Hayat, J. Akram, A. Alsaedi, and H. Zahir. Endoscopy and homogeneous-heterogeneous reactions in MHD radiative peristaltic activity of Ree-Eyring fluid. *Results in Physics* 8: 481-488 (2018).
32. C. Rajashekhar, F. Mebarek-Oudina, H. Vaidya, K.V. Prasad, G. Manjunatha, and H. Balachandra. Mass and heat transport impact on the peristaltic flow of a Ree-Eyring liquid through variable properties for hemodynamic flow. *Heat Transfer* 50(5): 5106-5122 (2021).
33. H. Balachandra, C. Rajashekhar, F. Mebarek-Oudina, G. Manjunatha, H. Vaidya, and K.V. Prasad Slip effects on a ree-eyring liquid peristaltic flow towards an inclined channel and variable liquid properties. *Journal of Nanofluids* 10(2): 246-258 (2021).
34. M. Shoaib, G. Zubair, K.S. Nisar, M.A.Z. Raja, M.I. Khan, R.P. Gowda, and B.C. Prasannakumara. Ohmic heating effects and entropy generation for nanofluidic system of Ree-Eyring fluid: Intelligent computing paradigm. *International Communications in Heat and Mass Transfer* 129(1): 105683 (2021).
35. S.S. Zafar, A. Zaib, F. Ali, F.S. Alduais, A.A. Bossly, and A. Saeed. Second law analysis on Ree-Eyring nanoliquid and Darcy Forchheimer flow through a significant stratification in the gyrotactic microorganism. *International Journal of Numerical Methods for Heat & Fluid Flow* 34(2): 494-519 (2024).
36. M. Turkyilmazoglu. Eyring–Powell fluid flow through a circular pipe and heat transfer: full solutions. *International Journal of Numerical Methods for Heat & Fluid Flow* 30(11): 4765-4774 (2020).
37. K. Abuasbeh, B. Ahmed, A.U.K. Niazi, and M. Awadalla. Entropy generation for MHD peristaltic transport of non-Newtonian fluid in a horizontal symmetric divergent channel. *Symmetry* 15(2): 359 (2023).
38. A. Fayyaz, Z. Abbas, and M.Y. Rafiq. Analysis of Radiatively Peristaltic Flow of Ree-Eyring Fluid Through an Annulus Region Between Two Flexible Tubes with Entropy Generation. *Arabian Journal for Science and Engineering* 1-14 (2024).
39. H. Shahzad, Z. Abbas, and M.Y. Rafiq. Rheological behavior of two immiscible hybrid nanofluids with modified thermal conductivity models through a heated curved pipe. *Alexandria Engineering Journal* 122: 318-333 (2025).
40. M. Turkyilmazoglu. Slip flow between corotating disks with heat transfer. *International Journal of Numerical Methods for Heat & Fluid Flow* 35(1): 257-276 (2025).
41. A. Naeem, Z. Abbas, and M.Y. Rafiq. Study of chemical properties of hybrid nanofluid flow between two permeable disks with suspension of carbon nanotubes using Yamada Ota and Xue models. *International Journal of Thermofluids* 26: 101075 (2025).

Proceedings of the Pakistan Academy of Sciences: A Physical and Computational Sciences 62(1): 31-40 (2025)

ISSN (Print): 2518-4245; ISSN (Online): 2518-4253
http://doi.org/10.53560/PPASA(62-1)875

Pakistan Academy of Sciences

Research Article

Design and Development of Intelligent Visual Simulator for Fault Detection, Identification and Diagnosis in PWR Nuclear Power Plant

Arshad Habib Malik[1*], Feroza Arshad[2], Aftab Ahmad Memon[3], and Raheela Laghari[4]

[1]Faculty of Engineering, Information and Technology, Sindh Institute of Management and Technology, Karachi, Pakistan
[2]Department of Information System Division, Karachi Nuclear Power Generating Station, Pakistan Atomic Energy Commission, Karachi, Pakistan
[3]Faculty of Electrical, Electronic and Computer Engineering, Mehran University of Engineering and Technology, Jamshoro, Sindh, Pakistan
[4]Faculty of Architecture, Mehran University of Engineering and Technology, Jamshoro, Sindh, Pakistan

Abstract: In this research, the AP600 Pressurized Water Reactor (PWR)-type Nuclear Power Plant (NPP) is studied due to its large number of components and complex, diversified systems. Operating a reliable and economical PWR NPP without malfunctions is desirable, with maximum safety as the primary goal. A Personal Computer Transient Analyzer (PCTRAN) is used as a data-driven source for AP600 PWR NPP, enabling simulations of both normal and abnormal operations. A state-of-the-art, fully automated, intelligent fault detection, identification, and diagnosis software (AI-FDID-PCTRAN) is designed and developed in Visual Basic to address various safety concerns and enhance the reliability and availability of AP600 PWR NPP systems. AI-FDID-PCTRAN is formulated, programmed, and configured based on unsupervised machine learning using Principal Component Analysis (PCA), a fully Automated Multivariate Statistical Process Control Technique (AMSPCT). The proposed PCA-based technique is a purely software-driven, systematically structured, and fully automated approach, developed specifically for the AP600 PWR nuclear industry. This specialized software offers capabilities not found in highly expensive, commercially available alternatives. FDD-PCTRAN has been tested against benchmark normal and abnormal transients available in AP600 PCTRAN and has proven to be highly reliable and accurate in fault detection and diagnosis.

Keywords: Automated System, Fault Detection and Diagnosis, Unsupervised Machine Learning, AP600, Abnormal Operation, PWR.

1. INTRODUCTION

Nuclear power plants are inherently designed with high level of engineering technology and safety. Safety is the prime concern in nuclear industry because the energy source in nuclear power plants is nuclear fission i.e. the production of radiation and ultimate release of nuclear energy. Pressurized Water Reactor (PWR) type nuclear power plants are far safer than other types of nuclear power plants. The PWR type nuclear power plants are basically built on the concept of negative temperature coefficients of reactivity. Nuclear power plants operate around its set-points and sufficient design control bands are provided for transient operation. Plants can cope small, large and even severe transient. However, fault conditions are designed associated with different systems of nuclear power plant and are required to detect and identify timely and accordingly the corrective actions are designed as mitigated actions after proper diagnosis of faults. A detailed literature review is conducted to

---

Received: September 2024; Revised: February 2025; Accepted: March 2025
* Corresponding Author: Arshad Habib Malik <engr.dr.arshad.habib.malik@gmail.com>

study various fault detection, identification and diagnosis techniques in nuclear power plants. A detailed technical review is conducted to study different fault detection and diagnosis methods used in nuclear power plants by Ma and Jiang [1]. Another detailed review is conducted to study different supervised and unsupervised data driven machine learning techniques used for condition monitoring in nuclear power plants by Hu *et al.* [2]. Fault detection in PWR type nuclear power plant components is addressed by Maio *et al.* [3] using statistical techniques. An online fault detection and isolation technique is established for PHWR type nuclear power plant using PCA technique by Yellapu *et al.* [4]. The research is explored for detection and identification of faults in PWR NPP instruments using Principal Component Method (PCA) by Ma and Jiang [5] while similar research is conducted for multiple faults in PWR sensors by Yu *et al.* [6]. A multi physics informed neural network (PIN) and deep neural network (DNN) based fault detection in regulating valves of nuclear power plants is explained by Lai *et al.* [7]. An entirely different approach is identified by Gallo and Capozzi [8] for pattern classification and feature selection using nonlinear PCA. Similar research is conducted for fault detection in dynamic time varying systems by Kazemi *et al.* [9] using neural network based PCA. A Simulink based reactor power control system is designed for PWR type nuclear power plant using Westinghouse Personal Computer Transient Analyzer (PCTRAN) by Ihrayz [10]. PCTRAN is used as virtual simulator of PWR dynamics. A fault diagnosis system is developed for CPR1000 3-loop PWR type nuclear power plant using deep neural network by Liu *et al.* [11]. Research is further explored for CPR1000 3-loop PWR type nuclear power plant by Ren *et al.* [12] in which Convolutional Neural Network-Long Short-Term Memory (CNN-LSTM) based model is constructed for fault diagnosis in normal and abnormal operating conditions. These scenarios are designed in specific CPR1000 PCTRAN. This research is further extended by Zhang *et al.* [13] in which fault diagnosis for CPR1000 PCTRAN is accomplished using sparrow search algorithm optimized CNN LSTM neural network. A PCA and Support Vector Machine (SVM) based fault diagnosis system is established for Main Steam Line Break (MSLB) accidental condition in CPR1000 PCTRAN by Xin *et al.* [14]. An investigation is performed for prediction of time series of nuclear power plant parameters using Backpropagation (BP) artificial neural network (ANN) by Liu *et al.* [15]. This research is carried out for Advanced Pressurized Water Reactor of 600 MWe rating (AP600) nuclear power plant. Another similar investigation is performed by Yong-kuo *et al.* [16] in which signed directed graph (SDG), PCA and ANN based cascaded fault diagnostic technique is developed for similar AP600 NPP. A PCA based fault detection and diagnosis methodology is designed for selected AP600 NPP fault conditions of primary and secondary systems by Elshenawy *et al.* [17]. Current methods with commercially available software are not intelligent and automated in their functionality. Methods other than PCA such as deep learning are time consuming, complex and mathematically stiff.

In the present study, a dedicated PCTRAN developed specially for AP600 PWR NPP in Visual Basic is integrated with a newly designed fully Automated Intelligent Fault Detection, Identification and Diagnosis software (AI-FDID) developed in Visual Basic. The integrated AI-FDID-PCTRAN is a state-of-the-art dedicated software for AP600 PWR nuclear power plant designed and configured based on data-driven unsupervised machine learning technology. The software is highly robust, intelligent and smartly detects normal and abnormal operations of AP600 PWR nuclear power plant. A dedicated software database is designed and PCA is addressed computationally and simulation experiments prove the effectiveness of proposed scheme.

2. MATERIALS AND METHODS

2.1. AP600 PCTRAN

PCTRAN is a computer code specially designed for PWR type nuclear power plants. PCTRAN program is a generic software covers light water reactor technology [10]. It is a Westinghouse design with thermal output power about 1800 MW_{th} (i.e., 600 MWe). PWR simulators are available for different power ratings and variants. Parameters of AP600 PCTRAN are tuned for 600 MWe.

In a Pressurized Water Reactor's design, reactor coolant is light water which also acts like moderator. The reactor has vertical reactor core filled with fuel, coolant and control rods. Reactor coolant is a pressurized water and its quality and chemistry is maintained. Reactor coolant is passed through the tubes of steam generator while feed water is passed through the shell structure of steam generators. High quality steam is produced and passed through the steam turbines. Steam turbines generate mechanical energy that in turn rotates the electrical generator and thereby the electrical energy is produced. All the systems work together and form a PWR power generating station [12]. The AP600 PCTRAN Simulator interface is shown in Figure 1.

2.2. Unsupervised Machine Learning: PCA

Machine learning techniques are widely used in system identification and pattern identification. Principal Components Analysis (PCA) is one of the very popular unsupervised machine learning technique. The basic design of PCA is established on statistical analysis. This technique is well suited for detecting the precursors responsible for changes in data. The core idea behind the PCA is to estimate and formulate the variance in process data [4]. Now-a-days, PCA is used extensively used in all areas of sciences, engineering and computing for statistical analysis to produce useful information for process and its health conditions.

In model based approach, first principle problem modeling is adopted for which very accurate and insightful knowledge of the process physics is required [5]. This modeling approach is governed on physical laws. Therefore, sometimes, it becomes very difficult to precisely model the process. In order to cater this problem, a data-driven approach is adopted. That's why data-driven PCA methodology is very popular for pattern identification. This method is further classified into statistical methods and non-statistical or signal based methods. PCA is a multivariate algorithms based technique and uses data driven approach which captures nonlinear patterns of datasets very well, so it is well suited for nuclear power plant applications in a much better and easier way then nonlinear techniques such as neural networks etc. That is why nonlinear techniques are not adopted due to complex structure and difficult configuration of software.

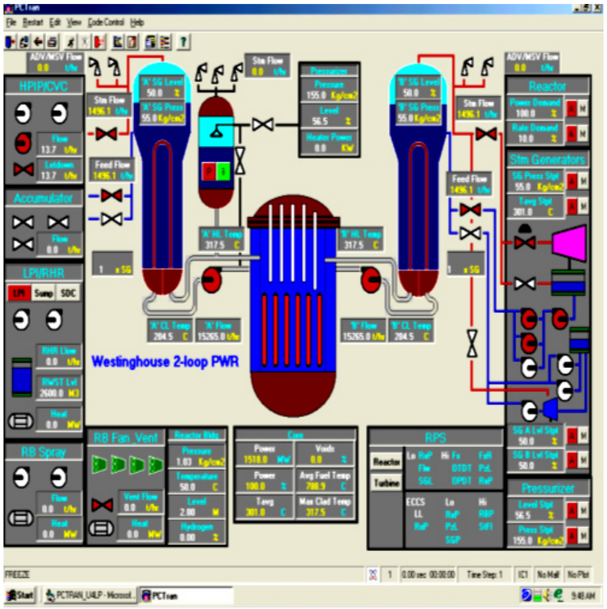

Fig. 1. AP600 PCTRAN simulator interface.

The task of PCA is then, given a sample of *n* objects with *m* measured quantities for each, i.e. *m* variables, x_j ($j = 1, 2, ..., m$), find a set of *m* new, orthogonal (i.e. independent) variables, $t_1, \dots\dots, t_i, \dots\dots\ t_m$, each one a formulation of actual variables, x_j as:

$$t_i = a_{i1}x_1 + \dots\dots + a_j x_j + \dots\dots + a_{in} x_m \qquad (1)$$

Where, constants a_{ij} are determined such that the smallest number of new set of variables is observed with maximum possible variance present in the data. The t_i dimension is called principal component and each value of t_i is known as score. The feature matrix *P* is known as loadings, which is constructed by taking the eigenvectors in the columns. The variation in the measurement domain covered by the loading vectors coupled with smallest eigenvalues. Eigenvectors are computed either from covariance matrix or SVD [3]. For covariance, output data from the process is standardized. Covariance is $m \times m$ symmetric matrix which shows the linear dependence of one dimension on another dimension. Then eigenvalues and eigenvectors will be calculated numerically. Cumulative Percentage Variance (CPV) test is performed to find out the number '*a*' for reduced dimensions. After finding out the '*a*', loading matrix is selected by using first '*a*' dimension, as it captures the most of information represented by data. The new variables scores will be produced from loadings and scaled data, which represent the data in reduced order. By using eigenvectors and scores, original observed data can be reproduced with little bit error.

Whereas another technique which is associated with matrix representation called Singular Value Decomposition (SVD). SVD deals with orthogonal matrix U and diagonal matrix W of singular values and the transpose of an m x m orthogonal matrix V^T. Eigenvalues are the square of these singular values while eigenvectors can be calculated by taking the transpose of V^T.

Eigenvectors can be computed by using either covariance matrix or SVD which are then sorted by their magnitude. At this step, it is decided to neglect the values of least importance. By doing so, some information will be lost but there will be no loss in case of smaller eigenvalues. If some components are ignored, then the final data set contains fewer dimensions than the original [17]. To be precise, if originally have m dimensions in data, then m eigenvectors and eigenvalues are calculated, and then only the first eigenvector is chosen, later the final data set has 'a' dimension. This can be done by using CPV method. In this method, 'a' is computed using the smallest number of loading vectors required to cater CPV.

2.3. T^2 and Q-Statistics Tests

PCA technique is used to decompose the original data into two or more orthogonal subspaces which independently provide unique information about the health of the plant. The model subspace is derived by choosing the first k principal components which provides information about parameters that shows greater changes in variation. The residual subspace, orthogonal to the model subspace provides the inverse information which describes what happens behind the scenes. The Q statistic is used to quantify the inverse information from the residual subspace and helps to overcome the masking concerns of faulty parameters that does not exhibit large changes in variation. The detection of changes in the simulation scenarios accomplishes independently through the Hotelling T^2 and square prediction error (SPE) or Q-statistics respectively. A combined discriminant that uses both the T^2 and SPE is used, which is capable of improved diagnosis based on assign weight. Contribution plots are used to examine the contribution of each parameter to the T^2 and SPE statistics respectively. From the contribution plots, it gives an idea that which parameter is causing the changes or fault. The computations are based on the matrix algebra of the singular value decomposition of the data correlation matrix. This is found to be very useful because it simplifies and reduces the number of processing steps required to complete the algorithm.

First, data is scaled then PCA is applied for fault detection. Proper scaling the data is very essential in PCA. Then T^2 and Q statistics are applied to draw control charts using calculated upper limits for fault detection. When an out-of-control signal is detected by T^2 or Q statistics control charts, then its identification is very essential. Fault diagnosis is a very critical function as generally while assessing variables, some variables of course move beyond very quickly during persistence of fault conditions. So, this information helps to further diagnose an actual cause of the fault. For this purpose, contribution plots can be used by using T^2 and Q statistics. For illustration purposes, a case study is selected to verify and validate the computations performed by software developed using MS Visual Basic 6.0. For this purpose, each of feature parameter, whole 150 observations data of Iris Flower are Scaled using mean and standard deviation and then 'Fault Detection' wizard in the software is applied to whole standardized data. The Fisher's Iris flowers dataset is designed consisting of data observations for three species. Four features are measured from each sample. Depending on mix of four features, a model is developed for analysis purposes. The plot of first three components of the dataset under consideration in 3D is shown in Figure 2.

Three principal components captures 99.5% of total deviation. Therefore, it mimics the maximum

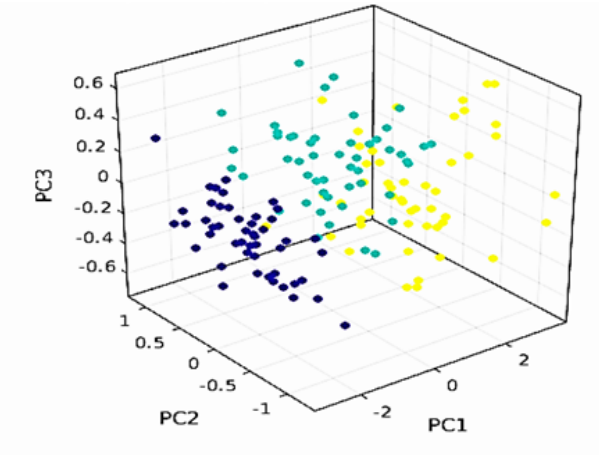

Fig. 2. Plots for first three principal components.

features through dimension reduction process. This proves the effectiveness and successful realization of the principal component analysis methodology adopted in extracting the features.

First two eigenvectors are selected in loading matrix for dimension reduction. The plot of scores computed by software for first two principal components is shown below in Figure 3.

The process in which fault is detected and then process variable is identified that contribute to fault which result in out-of-control status. In the present study, fault diagnosis is accomplished by categorizing different faults into different fault classes. Combined discriminant based on T^2 and Q statistics using Euclidean distance is used as a first choice for fault diagnosis, which is a pattern classification technique. Loading is stored into the database to measure the similarity between the two faults. The diagnosis results cover the similarity index and Euclidean distance calculated during match with each class stored in database. The statistical design data of PCA is summarized in Table 1.

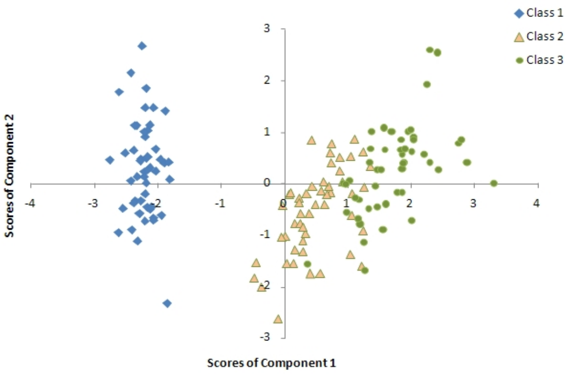

Fig. 3. Score plots for first two principal components.

Table 1. Statistical design data of PCA.

Statistical Design Parameters	Values
Total Observations	150
T_α	6.6447
T_β	4.9518
Similarity Index for Fault Class-1	0.5024
Similarity Index for Fault Class-2	0.9312
Similarity Index for Fault Class-3	1.0001
Euclidean Distance for Fault Class-1	0.1092
Euclidean Distance for Fault Class-2	0.0208
Euclidean Distance for Fault Class-3	0

2.4. Software Tool Design: AI-FDID-PCTRAN

In AI-FDID-PCTRAN design cycle, the first step is the design. In the present study, structural design approach is adopted. Its goal is to produce a model or representation of an entity that is decided to build. For this fault detection and diagnosis system classical structural design approach is used.

Modules are collection of functions, which perform same functionalities collectively and coherently. Module is described by its purpose and complete specification of functions included in it. In fault detection and diagnosis system two major modules are designed, which are fault detection training module and fault diagnosis testing module. These two modules share different functions. As both the modules constitute FDD system collectively, therefore, the common functions can be re-used from other module. Fault detection training module includes the functions which detect and identify fault in data.

Firstly, the data is gathered from the process then this data is scaled using mean and standard deviation. Also, data is classified into different fault classes based on faults for fault detection and diagnosis. Therefore, for each class initially principal component analysis is performed and then T^2 and Q statistics are calculated. The last task in this module is to calculate combined discriminant of class for which training is in progress and then store loadings, eigenvalues, eigenvectors, combined discriminant and fault information into the database. So, this module allows the FDD system to be trained for normal as well as different fault conditions, and to be used for fault diagnosis in next stage.

Fault diagnosis testing module mirrors the fault detection architecture, it includes the functions which diagnose the type of fault. After analyzing the given data, it is compared with fault classes which are already stored in database. Whichever fault class has the closest match is basically the desired category of fault.

This module performs principal component analysis, compute T^2 and Q statistics on given set of data for which fault diagnosis process is initiated, therefore, it shares many functions of fault detection module. After performing analysis, it diagnoses fault by matching combined discriminant with already stores combined discriminant of fault classes. It also computes similarity measure by making use of loading of given test case and loadings are already stored in the database for different fault classes. Whichever fault class already stored has the closest match is basically the desired category of fault. Fault diagnosis module shares almost all the functions of fault detection module except functions used for fault identification purpose using T^2 and Q statistics. In this study relational database design is used.

3. RESULTS AND DISCUSSION

In the present study, the AI-FDID-PCTRAN software design interface, performance analysis of AI-FDID-PCTRAN software in normal and abnormal conditions are investigated. Obstacles exist for using the proposed model across different types of nuclear reactor designs are the variations of parameters, configuration of parameters and system loops, etc.

3.1. AI-FDID-PCTRAN Software GUI

The AI-FDID-PCTRAN software is a systematic and fully automated intelligent application program. Rapid Application Development (RAD) environment i.e. Visual Basic 6.0 is used in the development and evaluation of User Interfaces (UIs). Visual Basic is used as it is user friendly and it is adopted because Pakistan Nuclear Regulatory Authority (PNRA) already using Visual Basic for all type of simulators and software development. PNRA has licensed Visual Basic software that can updated and modules could be improved for specific requirements. Multiple Document Interface Design Style (MDIDS) are used to make it easier to work with system. The computational tools are made available in AI-FDID-PCTRAN software and embedded in GUI tabs. The software qualifies the compliance and regulatory adherence of PNRA, which is necessary for using the software in the nuclear industry. It meets the requirements of PNRA and tested against benchmark data.

3.2. Performance Analysis of AI-FDID-PCTRAN in Normal Operating Conditions

Now, the testing and validation of fault detection, identification and diagnosis system is carried out using a case study in which principal component analysis is performed using T^2 and Q statistics for PCTRAN Simulator for 600 MWe PWR type nuclear power plant Data. In order to detect, identify and diagnose faults, following classes are considered in this case study:

1. Normal operation
2. Loss of coolant accident at hot leg for 95% break
3. Main steam line break for 95%
4. Main feed water pump failure

Four above mentioned associated fault scenarios are chosen due to space limitation and scope of this research study.

The process variables, i.e., parameters under consideration are:

1. Primary pressure: P (Kg/cm^2)
2. Average temperature: T_{avg} (°C)
3. Hot leg temperature: THA (°C)
4. Cold leg temperature: TCA (°C)

For each class 3000 observations/samples are collected in 3000 seconds through PCTRAN simulator. Then for each class, software is trained through fault detection wizard to store loading and combined discriminant into database for similarity measure and Euclidean distance computation in diagnosis phase respectively.

Initially, when simulator starts there may be some fluctuations for a certain time. After some time, simulator starts to operate in normal condition under steady state. The values for variables under consideration in normal operation are mentioned in Table 2.

Eigenvalues and eigenvectors are computed for normal operation of AI-FDID-PCTRAN for parametric variation from steady state to fault conditions as shown in Tables 3 and 4, respectively. It means this data is the representation of variation from normal operating conditions to transient conditions capturing the deviation dynamics.

In Table 4, component 1 through component 4 are the first four principal components. Eigenvectors are direction cosines for principal components, while eigenvalues are the variance in the principal components. Sum of all eigenvalues

Table 2. Normal operation parametric values of variables.

Parameters	Values
P (Kg/cm^2)	154.96
Tavg (°C)	300.93
THA (°C)	320.43
TCA (°C)	281.42

Table 3. Eigenvalues computed by AI-FDID-PCTRAN for normal plant operation data.

Parameters	Eigenvalues	Difference
Component 1 (C-1)	3.1584	2.3882
Component 2 (C-2)	0.7702	0.7061
Component 3 (C-3)	0.0641	0.0568
Component 4 (C-4)	0.0073	-

Table 4. Eigenvectors computed by AI-FDID-PCTRAN for normal plant operation data.

Parameters	(C-1)	(C-2)	(C-3)	(C-4)
P (Kg/Cm^2)	0.3183	0.9389	-0.1292	-0.0228
Tavg (°C)	-0.5529	0.1947	-0.0895	0.8052
THA (°C)	-0.5366	0.2719	0.7159	-0.3546
TCA (°C)	-0.5523	0.0821	-0.6803	-0.4747

is equal to the sum of variances which are on the diagonal of the variance-covariance matrix.

Eigenvectors are the vectors indicating the direction of the axes along which the data varies the most. Each eigenvector has a corresponding eigenvalue, quantifying the amount of variance captured along its direction. PCA involves selecting eigenvectors with the largest eigenvalues.

The largest eigenvalues with positive sign and their corresponding eigenvectors is crucial in PCA because they capture the most significant patterns in the data, reducing dimensionality while retaining most of the variability in plant dynamics. The change in eigenvalue shows the variation in eigenvalue due to the difference between steady state and fault conditions of plant.

Fault detection in AI-FDID-PCTRAN software is carried out by using T^2 and Q statistics control charts. In both control charts, before AP600 NPP reaches its steady state, there are some faults at the start. But after reaching steady state, no faults are observed using these statistics. T^2 and Q statistics are applied to draw control charts using calculated upper limits for fault detection. The threshold values are chosen using known plant normal and abnormal fault conditions for selected scenarios using computational schemes mentioned by Elshenawy *et al.* [17].

The threshold values computed for T^2 and Q statistics are 6.0015 and 0.4456 respectively. The resultant plots for fault detection using these statistics are shown in Figures 4 and 5 respectively. The results are generated using Microsoft Visual Basic software and found graphically systematic and visually unique in nature as compared to results observed previously [1-6].

Through fault identification contribution of each variable in faults is calculated by using T^2 and Q statistics contribution plots. As T^2 statistic and Q statistic detect and identify different type of faults,

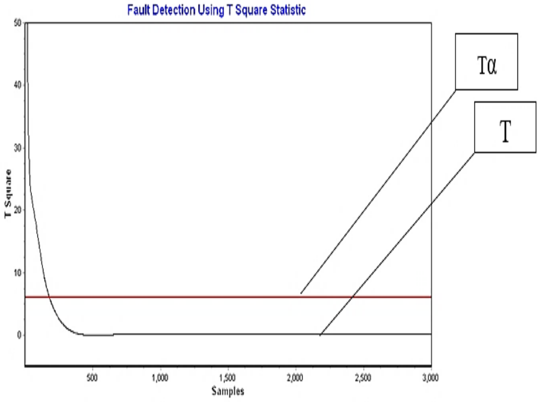

Fig. 4. Fault Detection through T^2 Statistics using Normal Plant Operation of AI-FDID-PCTRAN.

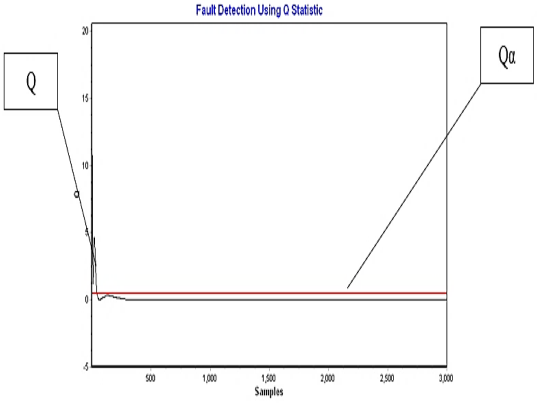

Fig. 5. Fault Detection through Q Statistics using Normal Plant Operation of AI-FDID-PCTRAN.

therefore, in this case study, it is observed that T^2 statistics are more sensitive to pressure surges than temperature surges whereas Q-statistic is sensitive to temperature changes. So, using T^2 statistic, it is observed that initial faults before achieving steady state condition are mainly due to pressure changes while fault detected by Q-statistics are mainly due to hot leg temperature changes. The contribution plots for fault identification using T^2 and Q statistics are shown in Figures 6 and 7 respectively. The normal operation plant data is successfully diagnosed from all other fault classes with similarity measure as 1.001 and Euclidean distance as 0.

3.3. Performance Analysis of AI-FDID-PCTRAN in Abnormal Operating Conditions

Realistic applications of AI-FDID-PCTRAN are Different abnormal conditions of plant and here in this research work as case study a scenario such as MSLB has been chosen for its specific usage.

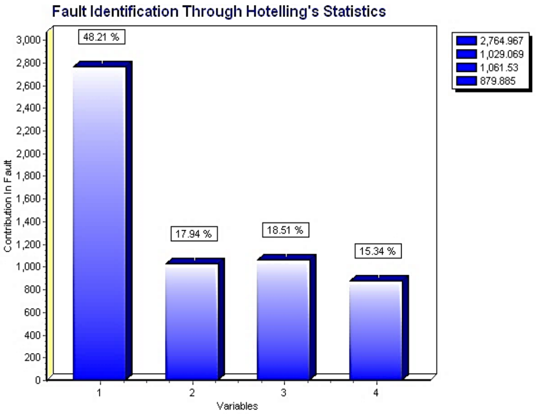

Fig. 6. Fault Identification through T^2 Statistics using Normal Plant Operation of AI-FDID-PCTRAN.

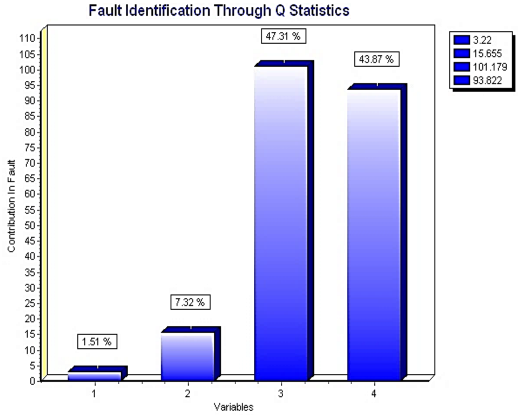

Fig. 7. Fault Identification through Q Statistics using Normal Plant Operation of AI-FDID-PCTRAN.

In abnormal operation, MSLB case is considered as typical scenario and presented in this study. When main steam line break occurs, initially T_{avg} is increased. This initial increment is due to the fact that steam flow rate is increased, and then reactor coolant system (RCS) temperature deceases as temperature difference increases in steam generator. Therefore, positive reactivity arises in the system, therefore temperature is increased due to increased fission rate. Initially at 100% reactor power T_{avg} is 302 °C. As turbine trips, neutron flux becomes zero due to the absorption of thermal neutrons in control rods. In other words, heat generation is stopped. The increment in the RCS temperature reduces the density of coolant. Therefore, water level of coolant in the pressurizer increases. This level increment produces small peak of pressure rise in coolant. As a result, the reactor is tripped, and RCS temperature continues to decrease further. This decrement in temperature reduces the system pressure.

Eigenvalues and eigenvectors are computed for MSLB introduced in AP600 PCTRAN using AI-FDID-PCTRAN for parametric variation from steady to fault conditions are mentioned in Tables 5 and 6 respectively.

Eigenvalues and eigenvectors are computed for abnormal operation of AI-FDID-PCTRAN for parametric variation from steady state to fault conditions as shown in Tables 5 and 6 respectively. It means this data is the representation of variation from abnormal operating conditions to transient conditions capturing the deviation dynamics.

In Table 5, the difference is calculated numerically by considering the eigenvalues at steady state and abnormal plant conditions at faults. The reference data or benchmark is the plant design data and design conditions describing plant normal operating conditions and fault condition as mentioned in plant design document available with PNRA.

The change in eigenvalues drops from first principal component through fourth principal component as the impact of plant dynamics reduces from first through fourth principal component. Table 6 has the similar interpretation for abnormal operation of plant as that of Table 4 discussed earlier.

Table 5. Eigenvalues computed by AI-FDID-PCTRAN for abnormal plant operation data (MSLB).

Parameters	Eigenvalues	Difference
Component 1 (C-1)	2.993	1.9884
Component 2 (C-2)	1.0046	1.0022
Component 3 (C-3)	0.0024	0.0024
Component 4 (C-4)	0	-

Table 6. Eigenvectors computed by AI-FDID-PCTRAN for abnormal plant operation (MSLB) data.

Parameters	(C-1)	(C-2)	(C-3)	(C-4)
P (Kg/Cm^2)	-0.0534	0.9934	-0.1011	-0.0011
Tavg (°C)	0.5775	0.0404	0.1005	-0.8091
THA (°C)	0.575	0.097	0.644	0.4952
TCA (°C)	0.577	-0.0452	-0.7516	0.3163

Fault detection in AI-FDID-PCTRAN software is carried out using T^2 and Q statistics control charts and only PCA method has been adopted for this study due to computational ease, unsupervised learning and flexibility of usage in visual software. T^2 statistics is more sensitive to pressure surges so when main steam line break occurs. The pressure fluctuation is observed not severe enough to be uncontrollable, so after that pressure begins to increase towards 155kg/cm^2. After some time, pressure again starts to decrease which is indicated by the rising trend at the end of scenario. The threshold value computed for T^2 statistic is 6.0015 while Q-statistic is more sensitive to detect temperature changes. As main steam line break occurs, initially temperature rises and then starts decreasing. The threshold value for Q-statistic computed by AI-FDID-PCTRAN software is 0.0158. Through fault identification contribution of each variable in faults is calculated by using T^2 and Q statistics. As T^2 statistic and Q statistic detect and identify different type of faults, therefore, in this case study, it is observed that T^2 statistics are more sensitive to pressure surges than temperature surges whereas Q-statistic is sensitive to temperature changes. So, using T^2 statistic, it is observed that faults are mainly due to pressure changes while fault detected by Q-statistics are mainly due to cold leg temperature changes. The main steam line break data is successfully diagnosed from all other fault classes with similarity measure as 0.9999 and Euclidean distance as 0. Alternative methods such as deep learning, SVM, or hybrid models with commercially available software are not intelligent and automated in their functionality. Hence, methods other than PCA are time consuming, complex, mathematically stiff as reported previously [7-15] and are beyond the scope of this research work. The case studies or scenarios presented in this study are unique and precise with great degree of reliability as compared to results reported by Ren *et al*. [12].

4. CONCLUSIONS

AP600 PWR nuclear power plant is attempted to extract the parametric innovative operational data using dedicated PCTRAN. PCA technique is used as unsupervised machine learning technique to decompose the original plant data into two or more orthogonal subspaces which independently provided unique information about the health of the plant. Fault detection is carried out using Q statistics while fault identification is accomplished through T^2 and Q statistics and fault diagnosis is established from designated fault classes. The performance of the proposed design scheme is tested for normal and abnormal plant operating conditions. Simulation experiments proves that the designed and developed AI-FDID-PCTRAN software is robust and fully automated as valid for normal and abnormal conditions with demonstrated variations in scenarios having entirely different plant conditions. The AI-FDID-PCTRAN software is intelligent and capable enough to predict the health monitoring and condition monitoring of any other system of AP600 available in PCTRAN that can be extended for different variants of PWR in future.

5. ACKNOWLEDGEMENTS

The support of the Sindh Institute of Management and Technology, Information Support Division of KNPGS and Mehran University of Engineering and Technology, is gratefully acknowledged.

6. CONFLICT OF INTEREST

The authors declare no conflict of interest.

7. REFERENCES

1. J. Ma and J. Jiang. Application of fault detection and diagnosis methods in nuclear power plants: A Review. *Progress in Nuclear Energy* 53: 255-266

(2011).

2. G. Hu, T. Zhou, and Q. Liu. Data-Driven Machine Learning for Fault Detection and Diagnosis in Nuclear Power Plants: A Review. *Frontiers in Energy Research* 9: 663296 (2021).
3. F.D. Maio, P. Baraldi, E. Zio, and R. Seraoui. Fault Detection in Nuclear Power Plants Components by a Combination of Statistical Methods. *IEEE Transactions on Reliability* 62(4): 833-845 (2013).
4. V.S. Yellapu, V. Vajpayee, Akhilan, and P. Tiwari. Online Fault Detection and Isolation in Advanced Heavy Water Reactor using Multiscale Principal Component Analysis. *IEEE Transactions on Nuclear Science* 66(7): 1790-1803 (2019).
5. J. Ma and J. Jiang. Detection and Identification of Faults in NPP Instruments using Kernel Principal Component Analysis. *Journal of Engineering for Gas Turbines and Power* 134: 103990 (2012).
6. Y. Yu, M. Peng, H. Wang, Z. Maa, and W. Li. Improved PCA Model for Multiple Fault Detection, Isolation and Reconstruction of Sensors in Nuclear Power Plant. *Annals of Nuclear Energy* 148: 107662 (2020).
7. C. Lai, I. Ahmed, E. Zio, Wei. Li, Y. Zhang, W. Yao, and J. Chen. A Multistage Physics-Informed Neural Network for Fault Detection in Regulating Valves of Nuclear Power Plants. *Energies* 17: 2647 (2024).
8. C. Gallo and V. Capozzi. Feature Selection with Non-Linear PCA: A Neural Network Approach. *Journal of Applied Mathematics and Physics* 7: 2537-2554 (2019).
9. P. Kazemi, A. Masoumain, and P. Martin. Fault Detection and Isolation for Time Varying processes using Neural based Principal Component Analysis. *Processes* 12(6)*:* 1218 (2024).
10. E.A.M.B. Ihrayz. PCTRAN Westinghouse AP1000 Power Control of Pressurized Water Reactor using Simulink of MATLAB. *Open Journal of Energy Efficiency* 12: 25-35 (2023).
11. B. Liu, J. Lei, J. Xie, and J. Zhou. Development and Validation of a Nuclear Power Plant Fault Diagnosis System based on Deep Learning. *Energies* 15*:* 8629 (2022).
12. C. Ren, H. Li, J. Lei, J. Liu, W. Li, K. Gao, G. Huang, X. Yang, and T. Yu. A CNN-LSTM based Model to FAULT Diagnosis for CPR1000. *Nuclear Technology* 209(9): 1365-1372 (2023).
13. C. Zhang, P. Chen, F. Jiang, J. Xie, and T. Yu. Fault Diagnosis of Nuclear Power Plant based on Sparrow Search Algorithm Optimized CNN-LSTM Neural Network. *Energies* 16*:* 2934 (2023).
14. M. Xin, W. Jiao, and L. Da-zi. Fault Diagnosis of Nuclear Power Plant based on Simplified Signed Directed Graph with Principal Component Analysis and Support Vector Machine. *Chinese Automation Congress, 22nd-24th November 2019, Hangzhou, China* (2009).
15. Y. Liu, F. Xie, C. Xie, M. Peng, G. Wua, and H. Xia. Prediction of Time Series of NPP Operating Parameters using Dynamic Model based on BP Neural Network. *Annals of Nuclear Energy* 85: 566-575 (2015).
16. L. Yong-kuo, A. Abiodun, W. Zhi-bin, W. Mao-pu, P. Min-jun, and Y. Wei-feng. Rajesh. A Cascade Intelligent Fault Diagnosis Technique for Nuclear Power Plants. *Journal of Nuclear Science and Technology* 55(3): 254-266 (2018).
17. L.M. Elshenawy, M.A. Halawa, T.A. Mahmoud, H.A. Awad, and M.I. Abdo. Unsupervised Machine Learning Techniques for Fault Detection and Diagnosis in Nuclear Power Plants. *Progress in Nuclear Energy* 142: 103990 (2021).

Proceedings of the Pakistan Academy of Sciences: A Physical and Computational Sciences 62(1): 41-51 (2025)
Copyright © Pakistan Academy of Sciences
ISSN (Print): 2518-4245; ISSN (Online): 2518-4253
http://doi.org/10.53560/PPASA(62-1)880

Pakistan Academy of Sciences

Research Article

A Text Mining Approach for Automated Case Classification of Judicial Judgment

Saad Rasool[1], Israr Hanif[1], Qaisar Rasool[1], Humaira Afzal[1], and Muhammad Rafiq Mufti[2]*

[1]Department of Computer Science, Bahauddin Zakariya University, Multan, Pakistan
[2]Department of Computer Science, COMSATS University Islamabad, Vehari Campus, Pakistan

Abstract: Court judgments are based on legal reasoning, evidence, and judicial decisions. However, many judgments are difficult to understand due to their length and complex language. Judges and attorneys often cite legal rulings to interpret regulations effectively. Legal education for lawyers, judges, and trainees benefits from judicial insights into legal reasoning, legislative interpretation, and legal standards. Accurate classification of legal judgments requires sophisticated methodologies. The increasing number of new and pending cases adds to the courts' workload, highlighting the need for efficient classification. Since only a limited number of court rulings are decided each year, many cases remain unresolved and are carried forward to the following year. Despite efforts to improve classification accuracy across judicial judgment datasets, Pakistani court judgments still lack a proper classification system. To address this gap, we compiled a dataset of criminal judgments from the Pakistani High and Supreme Courts. We developed a machine learning model using neural networks and a transformer architecture to achieve accurate classification. Our approach incorporated Support Vector Machine (SVM), Long Short-Term Memory (LSTM), and DistilBERT models, taking into account the dataset's volume and unique characteristics. Our research explores optimal classification algorithms tailored to Pakistan's legal landscape. After comparison, the DistilBERT transformer model outperformed the others, achieving an accuracy of 98%. It demonstrated an exceptional ability to understand contextual semantics and effectively handle the complexities of multi-label classification in legal judgments. The contributions of our work include the development of a new dataset of Pakistani court rulings, advancements in legal research, and an automated case classification system designed to streamline judicial procedures and enhance access to justice.

Keywords: Judicial Judgment, Judgment Classification, Pakistani Court, Machine Learning, Legal Knowledge.

1. INTRODUCTION

Legal judgments play a crucial role in judicial administration, as they represent the court's final decisions on verifiable issues and legal matters. Legal proceedings culminate in judgments that analyze evidence, legal arguments, and the court's conclusions. However, lawyers, lawmakers, and scholars often face significant challenges due to the sheer volume and complexity of court judgments. Court opinions frequently involve intricate language and reasoning, which can vary considerably. These judgments are often difficult to comprehend, as they include extensive legal vocabulary, precedents, and references. Lawyers spend countless hours analyzing lengthy opinions to identify relevant case precedents [1]. Legal specialists retrospectively examine cases to gain deeper insights into the factors that significantly influence judicial decisions [2]. Even individuals with strong comprehension skills must carefully read each judgment; therefore, legal determinations and case law are essential tools for legal education [3]. Classifying legal determinations is particularly challenging due to the diversity of legal language, the complexity of legal terminology, and the need for thorough analysis to distinguish between cases.

Since most people struggle to understand legal texts, lawyers must review and extract key information for end users [4]. The broad scope of legal document analysis is further complicated by the wide range of issues and concerns encountered by non-legal professionals and trial participants [5].

Received: January 2025; Revised: February 2025; Accepted: March 2025
* Corresponding Author: Muhammad Rafiq Mufti <rafiq_mufti@ciitvehari.edu.pk>

Judicial judgments employ specialized terminology, constitutional and case law references, and legal jargon. Traditional methods designed for general language processing often struggle to effectively classify this specialized legal language. Judicial judgments vary based on the authority, court level, and the nature of the case, with some involving more complex reasoning than others. Developing a predictive model is particularly challenging, as court proceedings depend on numerous factors that differ by case type [2]. Judicial language frequently contains ambiguity, as it blends legal reasoning with specific case facts. Criminal judgments span a broad spectrum of legal issues, encompassing both criminal and civil matters, which further complicates classification and information extraction.

Pakistan's court system has a massive backlog, and hundreds of rulings each year make problems worse. Although the courts have tried to reduce this backlog, many cases remain unresolved. These pending cases continue to add to the legal system's workload each year. New cases further increase court workloads, complicating the situation and delaying justice. In Australia, thousands of judgments are issued annually, but attorneys can only analyze a few, overlooking larger trends hidden within the cases [1]. A lack of adequate legal representation is a major reason contributing to the number of unsolved cases [6].

The backlog is exacerbated by administrative inefficiencies, such as procedural delays, inadequate court capacity, and insufficient funding. Moreover, the delays may be exacerbated by the competitive nature of lawsuits and the complex structure of judicial proceedings. These factors contribute to the growing number of cases, highlighting the need for efficient solutions to streamline judicial operations. As the number of pending cases continues to increase, there is an urgent need for strategies to reduce the court workload and improve legal system efficiency. Artificial Intelligence (AI) has the potential to address the challenges in both common law and civil law systems, including case congestion and delays in justice administration [3, 5]. Without intervention, the backlog will keep accumulating, resulting in a prolonged delay in justice. Efficient classification systems are essential to organize cases by their nature and category to tackle the court backlog.

Many studies have classified judicial cases in several ways. Traditional human annotation methods are applied to advanced machine learning and deep learning algorithms. In manual annotation systems, skilled personnel label decisions based on content and context. While successful, these procedures can be costly and time-consuming. Advanced algorithms, including ML, and Natural Language Processing (NLP) models, can automate the classification of legal rulings based on their semantic structure and linguistic aspects. Kwak *et al.* [7] presented a unique and useful challenge by providing a Korean Legal dataset [8]. They also employed multiple methods to find a distinct fine-tuning approach for small datasets. All models, except Multinomial Naïve Bayes (NB), achieved accuracy values above 63%. The Paraphrase-mpnet-basev2, fine-tuned with SetFit, outperformed all other models with 70.5% accuracy, a difference of at least 6% points. The second-best model was SVM, with 64.5% accuracy. Barman *et al.* [9] showed the efficiency of ML in processing Hindi legal data using Convolutional Neural Network (CNN) architecture on the Hindi Legal Documents Corpus [2, 9-12]. They classified Indian legal data [13-16] into two groups using convolutional layers. This model learns Bail Prediction binary classification from the pre-processed dataset, improving forecast accuracy and showing how ML can support legal decision-making. The researcher improved bail prediction test accuracy to 93% using data from 20 districts in Uttar Pradesh.

To improve the reliability of training data, Javed and Li [17] addressed semantic bias in legal judgment. The semantic bias in the CAIL dataset [18-21] was classified and identified using general-purpose AI. AI models outperformed structured professional risk assessment techniques in the CAIL dataset, which contains hundreds of incidents. Creative AI-based technologies could help lawyers. Semantic bias classification was used to detect bias in legal judgment. One legal approach classifies and identifies bias using the CAIL dataset, enabling to uncovering of semantic biases in court rulings. SVM, NB, MLP, and K-Nearest Neighbor classifiers were applied, with the SVM classifier outperforming the others, achieving 96.90% accuracy. Abbara *et al.* [22] used Arabic case materials to predict child custody and marriage annulment decisions using deep learning and NLP. PDF text was utilized to generate an Arabic judicial judgment prediction dataset for Saudi Personal Status cases. All 49 cases in this dataset have legitimate verdicts. The new dataset was analyzed using various DL and ML models, including Term Frequency-Inverse Document Frequency (TF-IDF), word2vec, LSTM, BiLSTM, and Logistic Regression. In the experiments, the SVM model with word2vec made the most accurate custody predictions (88%), and the LR model with TF-IDF made the most accurate annulment predictions (78%). Strickson and Iglesia [23] developed the LJP model, which was customized for UK court cases. Machine learning models were applied to a 100-year-old tagged UK judgments dataset of court decisions, creating a reliable, understandable prediction model. Both vector space features performed well; however, TF-IDF and LR achieved the best F1 score. Using n-grams and topic clusters as predictive feature sets was successful, and SLP and MLP algorithms further improved the results. Various feature formats and algorithms were tested, with their best model achieving an F1 score of 69.02 and an accuracy of 69.05%.

Shelar *et al.* [24] proposed legal annotation ideas for Indian criminal bail petitions using machine learning. Multiple research tests were conducted on 17 common ML models and compared using standard evaluation methods. ‘SmartLawAnnotator’ was developed as an open-source legal annotation suggestion system. Legal professionals labeled 2,000 samples using this approach. In smaller sample sizes, SVM models achieved the highest accuracy reaching up to 82%. Arriba-Pérez *et al.* [25] suggested a hybrid system using machine learning to categorize multi-label judgments (sentences) in the Spanish Legal System. The system integrates visual and natural language descriptions for explanation, NLP techniques, and advanced legal reasoning to identify parties involved in the cases. Their advanced legal AI system predicts and explains court decisions using ML, along with visual and plain language representation at the feature level. Previously, no known attempt had been made to mechanically recognize court decisions using multiple labels and high-quality natural language explanations. Legal professional-annotated tagged data achieved a micro accuracy of up to 85%.

Zahir [26] used Arabic written accounts to train a deep learning system for predicting judicial case outcomes. A deep learning model was trained in-house on Moroccan Court of Cassation cases to predict judgment. An innovative data augmentation strategy improved prediction performance due to the small corpus. Several deep learning model architectures along with FastText and GloVe embedding settings, were tested and analyzed. The method achieved an accuracy of 80.51% in predicting Moroccan Court of Cassation outcomes across six categories. To differentiate between classifying and anticipating court outcomes, Medvedeva *et al.* [27] developed a standardized collection of European Court of Human Rights [28-30] judgments. The dataset includes submitted cases, admissibility decisions, and pre-processed final decisions. They demonstrate that predicting court outcomes is more challenging than classifying judgments and establishing a benchmark for future research. SVM, Hierarchical Bidirectional Encoder Representations from Transformers (H-BERT), and LEGAL-BERT were tested for both classification and prediction tasks. H-BERT and LEGEL-BERT outperformed SVM in classification, however, SVM achieved better Macro F-scores. Zheng *et al.* [31] aimed to identify the most common causes of Preprocessing, Processing, and Postprocessing (PPP) conflict, summarized the findings and predicted litigation outcomes. They identified 17 legal variables and analyzed their impact on litigation outcomes in 171 PPP lawsuit cases from 2013-2018, sourced from China Judgments Online [32-34]. Using these 171 instances, they trained and evaluated nine ML models with the “prediction approach”. The ensemble models, i.e., GBDT, KNN, and MLP performed the best, surpassing the other nine ML models with a prediction accuracy of 96.42%.

In the context of the court system’s rising workloads and constrained resources, the importance of automated solution aid in case classification is becoming ever more evident. So, the legal field has traditionally utilized natural language systems because of their text-centric nature. In recent years, there has been an increasing trend to apply NLP to a wider range of legal sectors. This research work aims to build an automated system of specifically “criminal” case classification for Pakistani courts through the integration of a traditional ML approach, neural network, and cutting-edge transformer model.

2. DATASET DEVELOPMENT

Sequentially, it describes the processes that were done to construct the dataset for this research, beginning with the collecting of data, followed by the formulation of the dataset, preprocessing, feature engineering, and ending with the splitting of the dataset. A description of the framework for this process can be found in Figure 1.

2.1. Data Collection

The legal judgments in our collection were acquired comprehensively. Collecting legal judgments, particularly criminal ones, involved systematically compiling court rulings and conclusions on criminal cases. This required obtaining relevant judicial documents that were not available online. Since legal judgments were not easily accessible via the 'PAKISTANLAWSITE' website [35], collecting these judgments required court attendance. To access judicial judgments, users had to purchase a subscription plan and create an account. Personal engagement with court officials authorized judgment collection. The judgments from the Pakistani High and Supreme Court were available online. To preserve text and structure, 110 criminal judgments were collected in Word file format.

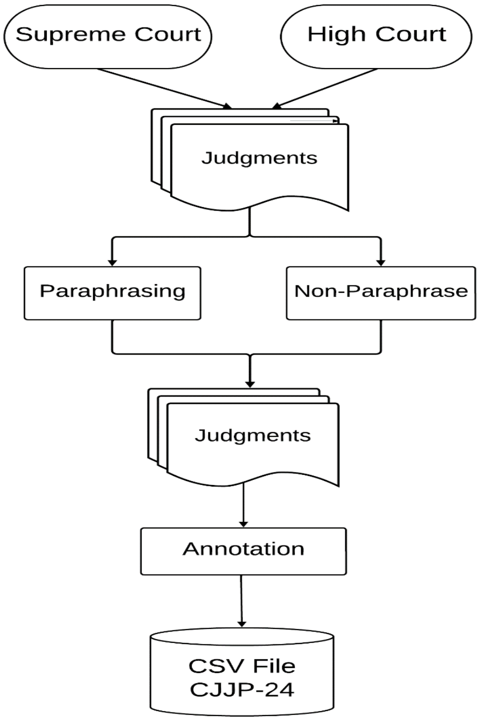

Fig. 1. Dataset creation process.

By utilizing the website's provided options, namely 'Full Judgment' and 'Head Notes', we were able to bypass a crucial step in summarizing judgments. In addition to the comprehensive and detailed judgments, the Head Notes, which originally represented the judge's actual order, were also included. Since complete judgments contain a significant amount of information on several non-essential features and components, we primarily gathered the Head Notes from the website. This method streamlined the data collection process and allowed us to concentrate exclusively on extracting the essential elements relevant to our classification objective.

2.2. Dataset Composition

Dataset construction is a crucial aspect of our work, as the integrity and organization of the data directly impact the study's conclusion. Acquiring a deep understanding of the dataset's nature is essential for effectively designing and developing its format during this phase. After careful deliberation, we determined that a multi-label classification is the most suitable approach for our dataset. Before proceeding with dataset generation, it is essential to fully understand the nature of the problem, which in this case is multi-label classification.

Unlike standard binary or multi-class classification, multi-label classification allows multiple labels to be assigned to each instance simultaneously. Legal field experts did the annotation; cross-checking among annotators assured precision and consistency. Most of the judgments targeted more than one label at once in the dataset. Multi-label text classification is an NLP task that involves assigning a text sequence to multiple categories at once [36]. This has significant implications for the administration of justice, as a single judgment may address multiple legal categories or offenses simultaneously. For instance, a judgment may encompass accusations of both theft and murder. Most of the judgments addressed more than one label at once in the dataset making it compulsory to adapt multi-label text classification nature.

2.3. Dataset Insights

To accurately represent the complexity of court decisions, particularly those involving multiple legal categories or offenses, we modified the multi-label classification process to construct our dataset. This approach lays the foundation for strong classification models capable of accurately predicting the presence of different legal categories in specific judgments. During the dataset formulation phase, our main focus was on developing a dataset optimized for multi-label classification. Initially, we identified six fundamental categories or subcategories relevant to the criminal domain: Murder, Dacoity, Rape, Fraud, Robbery or Theft, and Kidnapping.

Each category defines unique criminal offenses commonly encountered in legal proceedings. To organize our dataset, we created separate columns for each class. This framework effectively highlights the presence or absence of each category in individual cases, illustrating the complex and overlapping nature of criminal verdicts. Figure 2 illustrates the dataset's characteristics, target categories, and general organization using a multi-label classification approach.

2.4. Judgments Paraphrasing

The paraphrasing technique was employed to expand the dataset. To increase the number of instances, we used a paraphrasing tool to modify certain judgments. Specifically, the QuillBot AI tool was employed to rewrite the judgments by altering phrase structure and incorporating synonyms while maintaining the original meaning [37].

By employing this paraphrasing tool, we identified two significant advantages:

- It incorporates small structural changes, wording modifications, and synonyms. These variations enhance the model's training efficacy by introducing more versatile terminology.
- This method increases the number of instances in our dataset.

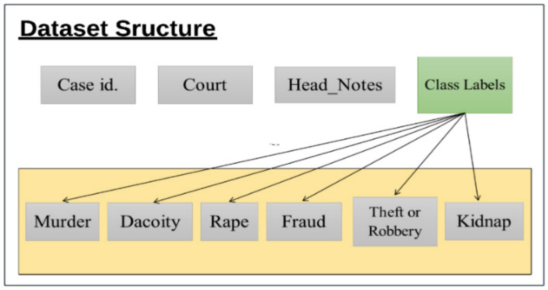

Fig. 2. Dataset structure.

A significant level of variability exists among court judgments regarding the judge's writing style [38]. By utilizing the paraphrasing technique, the total count of judgment instances in the dataset is now 221. Once the entire dataset was compiled, we designated it as "Criminal Judicial Judgments Pakistan (CJJP-24)". Paraphrased judgments were also thoroughly examined by legal annotators and experts to maintain their genuine legal value while providing textual versatility. Any type of ambiguous cases was discussed together to give the most suitable labels. The classification model will then be trained using this larger and more versatile corpus, which includes paraphrased judgments. This will improve its ability to generalize and identify subtle differences in legal language.

3. METHODOLOGY

Following a sequential approach, as illustrated in Figure 3, the procedures used to assess the performance of the adjusted methodology for this study are detailed.

3.1. Data Analysis and Visualization

The image aids in preprocessing and feature engineering tasks by displaying how the different text lengths are distributed in the dataset. It also provides an overview of the dataset's properties, which supports exploratory data analysis and informs decisions for subsequent models.

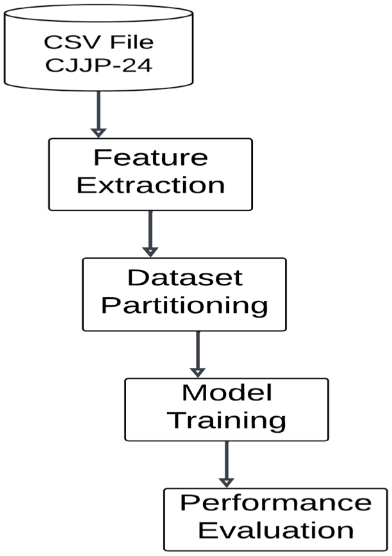

Fig. 3. Methodology process.

The text lengths in the dataset are shown in Figure 4. The highest point in the frequency distribution indicates that most judgment texts have word counts within a certain range. The figure also shows the distribution of judgment text lengths, highlighting any outliers or patterns. Additionally, the class correlation heatmap shown in Figure 5, shows the correlations between class labels in our multi-label classification dataset. This heatmap aids in classifying judicial judgments by showing how often specific classifications occur together. It displays the correlation coefficients between pairs of classes, with each column in the matrix representing the correlation value between two classes. The values range from -1 to 1, where '1' indicates a perfect positive correlation, meaning the presence of one category is consistently linked to the presence of the other. A correlation coefficient of '0' implies no association, while a negative value indicates a perfect negative correlation. Based on the heatmap, we can identify classes that frequently co-occur in judicial judgments as well as those that are more autonomous. This information is crucial for designing and interpreting our multi-label classification models.

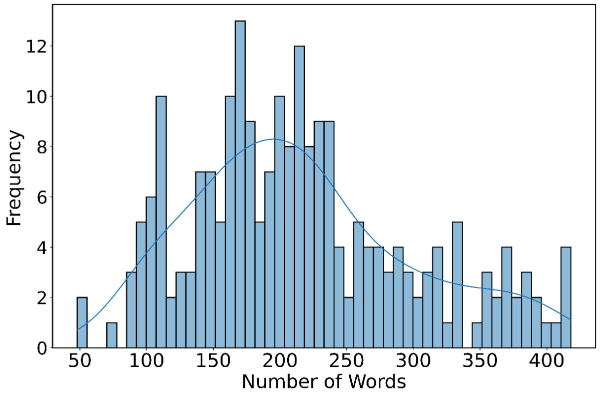

Fig. 4. Judgments text length graph.

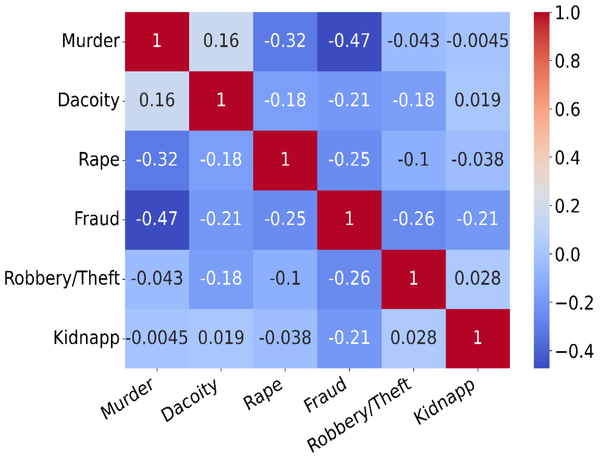

Fig. 5. Class correlation heatmap.

3.2. Data Preprocessing

Before building or using the prediction model, the judgment text must be preprocessed and feature extracted. This stage involves several essential processes to transform raw textual data into structural, model-ready data. To improve training data efficiency and quality, we prioritize text cleaning, tokenization, and vectorization. Additionally, implementing model modifications, such as encoding tokens and padding sequences, ensures compatibility with each model's input requirements. During the initial stage of text preprocessing, stop words are eliminated to improve the performance of subsequent processing steps. Removing frequently occurring stop words, such as 'and', 'the', and 'is', helps refine the text for classification purposes. The Natural Language Toolkit (NLTK) library has been employed to eliminate stop words for Support Vector Machine (SVM) processing. The NLTK stop words list includes 179 words, commonly used English words [39]. However, advanced neural network models, such as DistilBERT and Long Short-Term Memory (LSTM) do not require traditional stop-word removal for NLP tasks. In particular, Transformer models excel at extracting context-based information from complete phrase input sequences, even when stop words are present. This contrasts with traditional machine learning models, which primarily focus on word frequency.

The given text is separated into tokens, where long sentences are broken down into individual words. Tokens are separated using whitespaces and line breaks [40]. When training a machine to comprehend human language, tokenization, and vectorization strategies play a crucial role [41]. Machine learning models categorize text using feature information. Legal judgment classification involves extracting textual properties, such as words or sequences that convey meaningful patterns. These features are then converted into vectors, which are sequences of integers, so that, machine learning algorithms can process them. Most features are extracted automatically from large volumes of text. TF-IDF can be split into two components: TF and IDF. To evaluate the usefulness of word frequency, a phrase's frequency in the document must be examined. Inverse document frequency (IDF) measures a word's corpus prevalence. The number of documents d with a phrase t is referred to as document frequency.

We construct feature matrices for training and test sets by vectorizing judgments dataset using N-grams derived from the training set. N-grams are generated based on term co-occurrence frequencies within the corpus. The Count Vectorizer, a text preprocessing tool, converts a collection of text documents into a matrix of character frequencies. The Count Vectorizer tokenizes text data into words, building a lexicon with all unique terms from the training dataset. Each term in this dictionary is assigned a unique integer index. The text data is then transformed into a sparse matrix, where rows represent court judgments and columns correspond to dictionary terms. The matrix shows the frequency of each term within the given document. The LSTM model utilizes Count Vectorizer output, allowing it to analyze textual input by converting legal judgments into word frequency vectors. Applying the Count Vectorizer to the training set of judgments helps the LSTM model identify and understand text patterns and properties.

4. RESULTS AND DISCUSSION

The ML workflow requires model performance assessment to evaluate the efficacy and accuracy of our trained models. Three models were trained on our judicial judgments' dataset for classification. We have selected these three models based on two reasons; 1) To show the comparative analysis and difference in the results of using the machine learning model, LSTM, and the advanced transformer model, DistilBERT so that we can see how effective these advanced models are in performance compare to other. 2) As per our literature analysis, we conclude that in the machine learning category, SVM performs better in my legal text classification work among other ML models. Similarly, LSTM and BERT-based models have depicted outstanding performance for complex judgment text classification and sequence modeling. To determine the optimal parameters, we conducted multiple training and testing iterations. First, we vectorized the dataset and trained the SVM model. Then, we trained LSTM and DistilBERT models, carefully tracking training and validation loss. Pre-trained models were used for testing. Experimental results showed that the state-of-the-art transformer model achieved the best performance.

For correct model evaluation, we partitioned the dataset into training and testing parts, allocating 80% for training and 20% for testing, the 'train test split' technique. This technique split the whole dataset into two portions, one for training, and the other for testing the model. This partitioning method is widely used to ensure a lot of training data while maintaining a fair evaluation. We evaluated the effectiveness of SVM, LSTM, and DistilBERT, for classifying judicial judgments with multiple labels. Each model was assessed using key performance metrics, including accuracy, precision, recall, and F1 score. Table 1 provides a comprehensive comparison of their performances.

In summary, the evaluation results highlight the strengths and weaknesses of each model. SVM proves to be a reliable model for classifying legal judgments, exhibiting a well-balanced performance with a high precision of 95% and recall of 96%. The LSTM model also demonstrates strong performance, achieving a precision of 95% and an accuracy of up to 94%; however, its recall is relatively lower at 86%, indicating that it may not be able to identify specific pertinent classes. The DistilBERT transformer model remains the most efficient for this project, as its popularity is attributed to its high performance across several NLP tasks [42]. It outperforms all other models across key metrics, including precision, recall, and accuracy. Figure 6 illustrates the evaluation results for these models.

Table 1. Models performance analysis.

Models	Precision	Recall	F1-Score	Accuracy
SVM	95%	96%	95%	88%
LSTM	95%	78%	86%	94%
DistilBERT	95%	98%	96%	98%

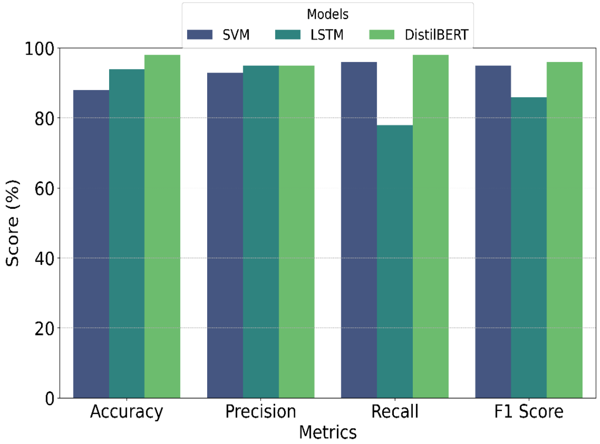

Fig. 6. Performance analysis graph.

The DistilBERT model is the most proficient and reliable methodology for the multi-label classification of judicial judgments. The SVM model ranks second, followed by the LSTM model as the third most proficient and reliable. This comprehensive assessment highlights the potential of advanced neural network models, particularly transformer-based models like DistilBERT, to achieve exceptional performance in complex classification problems. We conducted an experimental analysis by training all three models on the original judgment set and validating them using the 'train test split' technique. The dataset was partitioned into an 80-20 ratio for training and testing, respectively. The number of epochs was set to 5 for the LSTM model and 7 for the DistilBERT model.

Based on the results in Table 2, the SVM model exhibits high precision but moderate accuracy, reaching up to 0.55. This suggests that while the model effectively identifies true positive instances with few false positives, it struggles to capture all relevant classes, leading to a lower recall of 0.67. The LSTM model is adept at capturing the sequential relationships within judicial judgments. However, its relatively lower recall of 0.70 suggests that, despite excelling at generating accurate predictions, it may overlook certain categories. DistilBERT demonstrates outstanding performance, achieving a high accuracy of up to 0.98, along with precision, and recall, resulting in a remarkable F1 score of 0.95. This is attributed to its ability to capture contextual information and subtle subtleties in the text.

The results illustrated in Figure 7, were obtained by these models on the paraphrased judgments dataset. Our findings demonstrate that SVM may not handle the complexity and variability introduced by paraphrasing the judgments as effectively as neural network-based models [9, 13], leading to a lower accuracy of 0.59. While LSTM can better capture sequential dependencies, it may still struggle with the variability in paraphrased data, affecting recall (0.60). Despite being a powerful transformer-based model, DistilBERT's high precision of 0.95 but low recall of 0.53 suggests that while it is highly confident about its predictions, it misses many relevant instances, possibly due to overfitting. The results show that the meaning content of the paraphrased judgments was kept, but the models had a hard time with the new syntax that the paraphrasing tools added. This is especially true in situations with more than one label where the lines between labels can be fuzzy. It shows how much the models depend on original legal wording patterns and how hard it is to capture legal meanings through fake enhancement.

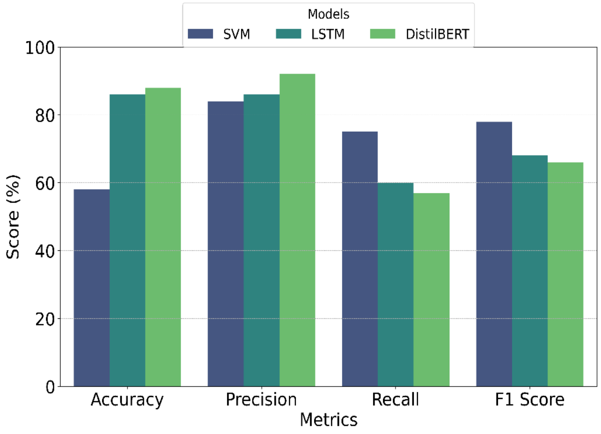

Fig. 7. Results on paraphrased judgments set.

Table 2. Results on the original judgments dataset.

Models	Precision	Recall	F1-Score	Accuracy
SVM	91%	67%	77%	55%
LSTM	91%	70%	79%	91%
DistilBERT	98%	93%	95%	98%

5. CONCLUSIONS

Court decisions are based on legal reasoning, facts, and judicial determinations. Judges and lawyers rely on legal rulings as precedents to interpret legislation. Classifying legal judgments requires sophisticated techniques to accurately categorize them. The increasing number of new and pending cases places a significant burden on courts, highlighting the need for efficient classification systems. Considerable efforts have been made to address these challenges and improve the categorization of legal decision datasets. However, the classification of Pakistani judicial verdicts remains underdeveloped. To address this gap, we created a large database of criminal case rulings from Pakistan's District, High, and Supreme Courts. Our data classification approach incorporates a standard machine learning model, a neural network, and an advanced transformer model. Traditional ML techniques such as TF-IDF Vectorizer with SVM classifier, were employed to handle the dataset's volume and unique characteristics. Additionally, we implemented more advanced models like LSTM and DistilBERT, which further enhanced the performance. Key results from our experiments include: DistilBERT outperformed the other models, achieving the highest accuracy of 98% on our dataset of judicial judgments. The SVM model demonstrated satisfactory performance, albeit with a slightly lower accuracy of 88%. On the other hand, the LSTM model achieved promising accuracy of up to 94%, however, it exhibited deficiencies in a recall. Future classification studies will examine more legal judgments and can be created by including constitutional, family, civil, and other rulings.

6. CONFLICT OF INTEREST

The authors declare no conflict of interest.

7. REFERENCES

1. W. Hwang, D. Lee, K. Cho, H. Lee, and M. Seo. A multi-task benchmark for korean legal language understanding and judgement prediction. *Advances in Neural Information Processing Systems* 35: 32537-32551 (2022).
2. V. Vaissnave and P. Deepalakshmi. A keyword-based multi-label text categorization in the Indian legal domain using bi-LSTM. In: Soft Computing: Theories and Applications: Proceedings of SoCTA 2020, Volume 1 (Advances in Intelligent Systems and Computing, 1380). T.K. Sharma, A.W. Ahn, O.P. Verma, and B.K. Panigrahi (Eds.). *Springer, Singapore* pp. 213-227 (2022).
3. S. Agrawal. How To Read Court Judgments Quickly and Efficiently (2023). https://www.scribd.com/document/628208457/How-to-Read-Court-Judgments-Quickly-and-Efficiently.
4. B. Shukla, S. Gupta, A.K. Yadav, and D. Yadav. Challenges and issues in legal documents classification. *AIP Conference Proceedings* 2754(1): 020001 (2023).
5. J. Li, G. Zhang, L. Yu, and T. Meng. Research and design on cognitive computing framework for predicting judicial decisions. *Journal of Signal Processing Systems* 91(10): 1159-1167 (2019).
6. G. Sukanya and J. Priyadarshini. A meta-analysis of attention models on legal judgment prediction system. *International Journal of Advanced Computer Science and Applications* 12(2): 531-538 (2021).
7. A.S. Kwak, C. Jeong, J.W. Lim, and B. Min. A Korean Legal Judgment Prediction Dataset for Insurance Disputes. *arXiv preprint arXiv* 2401: 14654 (2024).
8. A.J. Rawat, S. Ghildiyal, and A.K. Dixit. Topic Modeling Techniques for Document Clustering and Analysis of Judicial Judgements. *International Journal of Engineering Trends and Technology* 70(11): 163-169 (2022).
9. A. Barman, D. Roy, D. Paul, I. Dutta, S.K. Guha, S. Karmakar, and S.K. Naskar. Convolutional Neural Networks can achieve binary bail judgement classification. *arXiv preprint arXiv* 2401: 14135 (2024).
10. K. Shirsat, A. Keni, P. Chavan, and M. Gosavi. Legal judgement prediction system. *International Research Journal of Engineering and Technology* 8(5): 734-738 (2021).
11. R.A. Shaikh, T.P. Sahu, and V. Anand. Predicting outcomes of legal cases based on legal factors using classifiers. *Procedia Computer Science* 167: 2393-2402 (2020).
12. V. Malik, R. Sanjay, S.K. Nigam, K. Ghosh, S.K. Guha, A. Bhattacharya, and A. Modi. ILDC for CJPE: Indian legal documents corpus for court judgment prediction and explanation. *arXiv preprint arXiv* 2105: 13562 (2021).
13. N. Sivaranjani, V.K.S. Ragavan, and G. Jawaherlalnehru. A Neural Network model for Indian Supreme Court legal judgment prediction. *Journal of Intelligent & Fuzzy Systems* 1: 235936 (2024).

14. S.S. Megala. Classification of Legal Judgement Summary using Conditional Random Field Algorithm. *International Journal of Computer Sciences and Engineering* 6(5): 23-33 (2018).
15. R. Sil and A. Roy. A novel approach on argument based legal prediction model using machine learning. *IEEE International Conference on Smart Electronics and Communication, (10-12 September 2020), Trichy, India* pp. 487-490 (2020).
16. P. Bhilare, N. Parab, N. Soni, and B. Thakur. Predicting outcome of judicial cases and analysis using machine learning. *International Research Journal of Engineering and Technology* 6(3): 326-330 (2019).
17. K. Javed and J. Li. Artificial intelligence in judicial adjudication: Semantic biasness classification and identification in legal judgement. *Heliyon* 10(9): e30184 (2024).
18. A. Fan, S. Wang, and Y. Wang. Legal Document Similarity Matching Based on Ensemble Learning. *IEEE Access* 12: 33910-33922 (2024).
19. Z. Yang, J. Ge, T. Hu, W. Yu, Y. Zheng, and Y. Dong. Text Classification of Judgement Documents Considering Sample Imbalance. *17th IEEE Conference on Industrial Electronics and Applications (16-19 December 2022)*, *Chengdu, China* pp. 1459-1462 (2022).
20. Y. Wang, J. Gao, and J. Chen. Deep learning algorithm for judicial judgment prediction based on BERT. *5th IEEE International Conference on Computing, Communication and Security (14-16 October 2020), Patna, India* pp. 1-6 (2020).
21. B. Chen, Y. Li, S. Zhang, H. Lian, and T. He. A deep learning method for judicial decision support. *19th IEEE International Conference on Software Quality, Reliability and Security Companion (22-26 July 2019)*, *Sofia, Bulgaria* pp. 145-149 (2019).
22. S. Abbara, M. Hafez, A. Kazzaz, A. Alhothali, and A. Alsolami. ALJP: An Arabic Legal Judgment Prediction in Personal Status Cases Using Machine Learning Models. *arXiv preprint arXiv* 2309: 00238 (2023).
23. B. Strickson and B.D.L. Iglesia. Legal judgement prediction for UK courts. *3rd International Conference on Information Science and Systems (19 - 22 March, 2020)*, *Cambridge, United Kingdom* pp. 204-209 (2020).
24. A. Shelar, M. Moharir, V. Nama, J. Jaikumar, V. Patil, and A. Edupuganti. SmartLawAnnotator: A Machine Learning-Based Annotation Recommendation for Judgment Prediction. In: International Conference on Advances in Data-driven Computing and Intelligent Systems. *Springer, Singapore* pp. 415-430 (2023).
25. F. de Arriba-Pérez, S. García-Méndez, F.J. González-Castaño, and J. González-González. Explainable machine learning multi-label classification of Spanish legal judgements. *Journal of King Saud University-Computer and Information Sciences* 34(10): 10180-10192 (2022).
26. J. Zahir. Prediction of court decision from a rabic documents using deep learning. *Expert Systems* 40(6): e13236 (2023).
27. M. Medvedeva, A. Üstün, X. Xu, M. Vols, and M. Wieling. Automatic judgement forecasting for pending applications of the European Court of Human Rights. *Proceedings of the Fifth Workshop on Automatec Semantic Analysis of Information in Legal Text*. *CEUR Workshop Proceedings* pp. 12-23 (2021).
28. C. O'Sullivan and J. Beel. Predicting the outcome of judicial decisions made by the european court of human rights. *arXiv preprint arXiv* 1912: 10819 (2019).
29. M. Medvedeva, M. Vols, and M. Wieling. Judicial decisions of the European Court of Human Rights: Looking into the crystal ball. *13th Annual Conference on empirical legal studies (9-10 November, 2018), University of Michigan Law School, USA* pp. 24 (2018).
30. M. Medvedeva, M. Vols, and M. Wieling. Using machine learning to predict decisions of the European Court of Human Rights. *Artificial Intelligence and Law* 28(2): 237-266 (2020).
31. X. Zheng, Y. Liu, J. Jiang, L.M. Thomas, and N. Su. Predicting the litigation outcome of PPP project disputes between public authority and private partner using an ensemble model. *Journal of Business Economics and Management* 22(2): 320-345 (2021).
32. Y. Fang, X. Tian, H. Wu, S. Gu, Z. Wang, F. Wang, and Y. Weng. Few-shot learning for Chinese legal controversial issues classification. *IEEE Access* 8: 75022-75034 (2020).
33. L. Liu, D. An, Y. Wang, X. Ma, and C. Jiang. Research on legal judgment prediction based on Bert and LSTM-CNN fusion model. *3rd IEEE world symposium on artificial intelligence (18-20 June 2021)*, *Guangzhou, China* pp. 41-45 (2021).
34. Y. Liu and Y. Chen. A two-phase sentiment analysis approach for judgement prediction. *Journal of Information Science* 44(5): 594-607 (2018).
35. https://www.pakistanlawsite.com/Login/MainPage.
36. M. Omar, S. Choi, D. Nyang, and D. Mohaisen.

Robust natural language processing: Recent advances, challenges, and future directions. *IEEE Access* 10: 86038-86056 (2022).

37. T.N. Fitria. QuillBot as an online tool: Students' alternative in paraphrasing and rewriting of English writing. *Englisia: Journal of Language, Education, and Humanities* 9(1): 183-196 (2021).
38. K. Clark, U. Khandelwal, O. Levy, and C.D. Manning. What Does Bert Look At? An Analysis of Bert's Attention. *arXiv preprint arXiv* 1906: 04341 (2019).
39. S. Sarica and J. Luo. Stopwords in technical language processing. *Plos One* 16(8): e0254937 (2021).
40. R.C. Staudemeyer and E.R. Morris. Understanding LSTM-a tutorial into long short-term memory recurrent neural networks. *arXiv preprint arXiv* 1909: 09586 (2019).
41. G. Sukanya and J. Priyadarshini. Analysis on word embedding and classifier models in legal analytics. *AIP Conference Proceedings* 2802(1): 140001 (2024).
42. D.W. Otter, J.R. Medina, and J.K. Kalita. A survey of the usages of deep learning for natural language processing. *IEEE transactions on Neural Networks and Learning Systems* 32(2): 604-624 (2020).

Proceedings of the Pakistan Academy of Sciences: A
Physical and Computational Sciences 62(1): 53-65 (2025)
Copyright © Pakistan Academy of Sciences
ISSN (Print): 2518-4245; ISSN (Online): 2518-4253
http://doi.org/10.53560/PPASA(62-1)681

Pakistan Academy of Sciences

Research Article

Evaluating the Efficacy of Convolutional Neural Networks Across Diverse Datasets

Swati Gupta*, Bal Kishan, and Pooja Mittal

Department of Computer Science and Applications, Maharshi Dayanand University (MDU), Rohtak, India

Abstract: Focusing on sentiment analysis and medical image processing, this paper assesses Convolutional Neural Networks performance across different datasets. Emphasized are recent developments in deep learning models for segmentation and picture categorization as well as other purposes. Using contemporary Convolutional Neural Network architectures, this work seeks to get good performance in medical diagnosis and sentiment analysis. The paper emphasizes how well Convolutional Neural Networks perform in domain-specific tasks. Using the same data preparation techniques, appropriate designs, and strategies to split the data, this paper investigates how well Convolutional Neural Network algorithms perform on medical data and sentiment analysis. Convolutional Neural Network models are optimized using hyperparameter tweaking and cross-validation techniques. While guaranteeing patient privacy, data anonymization, and bias reduction, the research seeks to highlight strengths, weaknesses, and patterns. Focusing on ethical concerns and offering suggestions for improvement, it tackles problems in sentiment categorization and medical imaging anomaly detection. This work attains 96 percent accuracy using Convolutional Neural Networks across four datasets. Common measures in the performance assessments of Sentiment Analysis, Skin Cancer Detection, Brain Tumour Detection, and Kidney Stone Detection include F1 scores, recall, and accuracy. With 0.97, Brain Tumour Detection had the highest accuracy; Kidney Stone Detection and Skin Cancer Detection both had 0.95; Sentiment Analysis scored 0.96. The consistently high recall and accuracy scores across all domains indicate good classification capabilities; an F1 score between 0.95 and 0.96 guarantees outstanding performance in both detection and analysis tasks.

Keywords: Accuracy, Precision, Performance Metrics, Diverse Datasets, CNNs.

1. INTRODUCTION

CNNs are special neural networks that can process inputs that resemble grids, such as images. CNNs leverage a basic design of connected layers to enable tasks like object recognition and picture categorisation. These activities rely on the input data to extract key attributes. CNNs excel in part because they can learn feature hierarchies from input pictures automatically and efficiently. Convolution layers do this by applying filters to the input picture to identify different patterns and characteristics [1]. To further reduce computational complexity while preserving critical information. In the end, the learned representations in Figure 1 are used to make predictions, and the retrieved features are integrated by fully linked layers. The figure shows CNN architecture for image processing or recognition tasks. It consists of an input, convolutional, max-pooling, hidden, and an output layer. Compared with 125 x 125 pixels, the input layer takes color pictures. Max-pooling layers downscale feature maps; convolutional layers shrink spatial dimensions. Compared with 784 and 16 neurons, the hidden layers enable the learning of intricate patterns. The S neurons in output layer reflect classes in the classification challenge [1].

Although very effective, CNNs have several shortcomings. One disadvantage of vanishing gradients in deep networks with several layers is that the gradients required changing network parameters decrease, thereby either delaying or ceasing learning. Usually, proper network weight

---

Received: November 2024; Revised: February 2025; Accepted: March 2025

* Corresponding Author: Swati Gupta <swati.rs20.dcsa@mdurohtak.ac.in>

initialization, specialized activation functions, batch normalization, and skip connections help to encourage gradient flow throughout the network. Current deep learning methods depend on CNNs, which also drive image analysis and related fields to unprecedented heights despite challenges. CNNs shine in NLP and computer vision. CNNs are the foundation of healthcare image analysis in disease detection and identification [1]. CNNs can assist in the image data analysis for public opinion and sentiment trends. This work will evaluate the performance of the CNN algorithm in skin cancer detection [2], emotion analysis [3], renal stone detection [4], and brain tumor diagnosis [5]. The joint study of these domains clarifies CNN efficiency in various situations and shares obstacles and discoveries are shown in Figure 1.

Figure 1 presents Convolutional Neural Network (CNN) architecture where input layer receives raw image data, which is passed through convolutional layers that apply filters to extract local features like edges and textures. These features are then passed through activation functions such as ReLU to introduce non-linearity, followed by pooling layers that reduce the spatial size and retain important information. This feature extraction process is repeated to form a deep representation of the input. The resultant feature maps are flattened and transmitted to fully linked layers, which identify high-level patterns and connections. The output layer uses methods such as softmax to categorise the input into established classifications. The significance of the study lies in the comprehensive assessment of CNNs in two crucial areas: sentiment analysis [3] and medical image processing [4, 5]. This work improves diagnostic accuracy, fraud prevention, and sentiment analysis by addressing the limitations of existing approaches and exploring creative concepts, such as optimisation algorithms and hybrid models. The results suggest implications for the creation of reliable, effective, and scalable practical deep learning systems. Correlation of datasets to research work is given below:

- Sentiment Analysis Datasets: Datasets for sentiment analysis, including emotion, opinion, and sentiment analysis image data, are available here. Highlighting sentiment classification and feature extraction, they establish a foundation for assessing CNN's image processing capabilities [3].
- Medical picture Datasets: The capabilities of CNNs in picture segmentation and classification are assessed using datasets for kidney stone detection, brain tumour identification, and skin cancer diagnosis. These datasets facilitate the assessment of the algorithms' proficiency in accurately classifying illnesses and identifying outliers [4, 5].

In similar way the correlation of research studied to present research work are given below:

- Image Classification and Segmentation: CNN's performance might be enhanced by using the content-based image retrieval techniques suggested by Alrahhal and Supreethi [6] and by Zohra *et al.* [7] segmentation-based image classification.
- Medical Image Processing: This study in line with Silambarasan *et al.* [8] on PCOS diagnosis and Pandiyarajan and Valarmathi [9] on dementia classification using VDRNet19 seeks to enhance sickness diagnosis using deep learning.

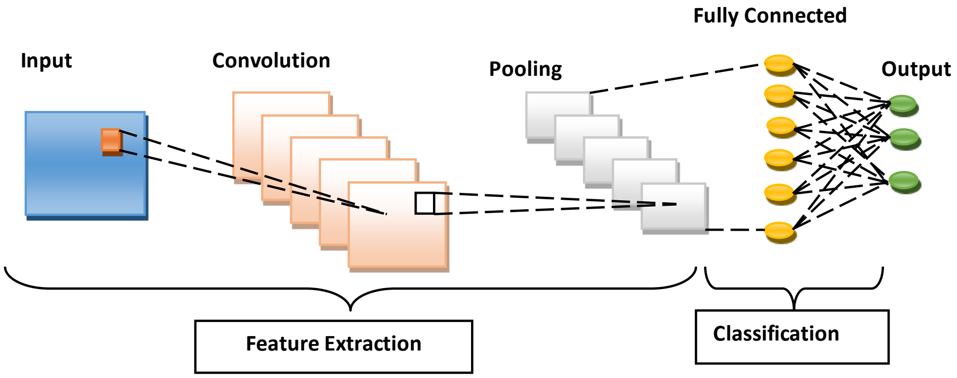

Fig. 1. CNN architecture.

- Security and Network Analysis: New hybrid methods to resilient classification issues are inspired by the work of Bandu *et al.* [10] on counterfeit detection.

The present study's research gap highlights the remarkable efficacy of CNNs in various tasks, including image classification, object identification, and feature extraction. But the majority of contemporary research focuses on their application within a particular domain or dataset. The existing study aims to assess CNN efficacy on homogenous datasets, including medical pictures or natural language tasks converted into image-like formats. Nonetheless, there is a significant deficiency in thorough research evaluating the generalizability and comparative effectiveness of CNNs across many datasets spanning multiple industries, such as medical imaging and Image-based sentiment/emotion categorization. Differences in data types, uneven class distribution, and specific features of different fields make it hard for CNNs to work well across various situations, like comparing grayscale and RGB images or low-resolution and high-resolution scans. Few studies investigate the functioning of CNN designs or the modifications required when applying them to diverse data types. This disparity hinders our comprehension of the flexibility, transferability, and resilience of CNN design while transitioning across various data environments. Filling this research gap will improve our understanding of how adaptable CNNs are, help us choose the right models for different applications, and support the development of more flexible neural network designs.

This study cannot emphasize the significance of CNNs in medical image processing. Healthcare workers urgently want automated methods to aid in interpreting intricate pictures, given the substantial rise in medical imaging data. CNNs can extract important details from basic pixel data, making it easier to identify, categorize, and locate problems in medical images. The primary convolutional neural network employed in healthcare is for brain tumor identification. Convolutional neural networks help find and treat cancers early by accurately identifying and describing them using magnetic resonance imaging. Convolutional Neural Networks analyze CT images to detect and assess kidney stones. CNNs proficiently identify skin cancer in dermatological applications. They accurately diagnose benign and malignant tumors using microscope pictures. CNNs have been shown to be beneficial in sentiment analysis, particularly in extracting sentiment from images, as well as their use in medical imaging. Sentiment analysis with the Flickr30k dataset entails deriving emotional meaning from photographs by correlating visual areas with descriptive captions. Models acquire the ability to concurrently evaluate visual signals and words to forecast underlying attitudes. This study analyzes current works using CNNs for various tasks, focusing on their techniques, experimental configurations, and performance measures. This paper offers significant insights into the advantages and drawbacks of CNNs in medical image analysis and sentiment analysis. This study examines previous research and highlights prevalent themes and issues. The study then talks about possible future research directions, such as looking into new CNN architectures, combining different types of data, and creating models that are easier to understand and improve clinical decision support and sentiment analysis. This paper enhances the current discourse on the utilization of CNNs in healthcare and NLP, aiming to progress to the forefront of medical image analysis and sentiment analysis fields.

In their study, Debnath and Mondal [11] recommended CNN and PCA for dynamic variance control in audio compression. The GCN-based intelligent network traffic analysis and classification model by Olabanjo *et al.* [12] was designed to handle complicated, interconnected network traffic data. Alrahhal and Supreethi [13] improved content-based image retrieval with machine learning. Silambarasan *et al.* [14] improved SVM and DenseNet for PCOS detection. SVM's classification and DenseNet's deep learning enhance PCOS diagnosis. Mishra *et al.* [15] used neurosymbolic AI to predict how much energy CoCrMo-architected materials can absorb in material science. Alzubaidi *et al.* [16] provided a detailed look at deep learning methods, focusing on CNN architectures and explaining important parts such as convolutional layers, pooling methods, activation functions, and fully connected layers. They addressed problems and prospective approaches. Zhao *et al.* [17] highlighted the uses of CNNs in computer vision, providing a comparative examination of cutting-edge architectures and their performance measures. Cong *et al.* [18] grouped

CNN architectures based on their features, pointing out how quickly CNNs are being developed and adjusted for specific tasks.

Despite significant advancements in deep learning, the application of CNNs across diverse datasets poses challenges, particularly in achieving consistent performance in sentiment analysis and medical image processing. Existing models often struggle with generalization, robustness, and accuracy in handling complex, high-dimensional datasets. This research aims to evaluate the applicability and limitations of CNNs for diverse tasks while integrating insights from related studies to enhance their efficacy. The objective and scope of the present study is to evaluate the performance of CNNs in sentiment analysis and medical image processing across diverse datasets. Research has integrated advanced optimization techniques and hybrid models for improving classification accuracy and robustness. Upcoming research is supposed to set benchmark CNN performance against conventional techniques and state-of-the-art models in related fields. The focus of research work is to identify domain-specific challenges and propose strategies for overcoming them using deep learning.

2. RESEARCH METHODOLOGY

The objectives, are defined pertinent medical datasets are selected, data preprocessing steps are standardized, appropriate CNN architectures are selected, datasets are divided into training, validation, and test sets, cross-valuation or bootstrapping is implemented, and hyperparameter tuning forms the basis of the research methodology for a comparison of CNN algorithm performance on medical datasets and sentiment analysis.

Because in presvious research Campos *et al.* [19] concentrated on enhancing CNNs for on-device implementation, prioritizing energy-efficient architectures while maintaining accuracy—essential for edge computing and mobile systems. Khan *et al.* [20] conducted a comprehensive survey of the evolution of CNN architectures, ranging from LeNet and AlexNet to more intricate networks such as ResNet and DenseNet, highlighting innovations including skip connections, depth-wise separable convolutions, and attention mechanisms that have markedly enhanced architectural design. Through cross-validation or bootstrapping, the experimental design divides datasets into training, validation, and test sets and hyperparameter adjustment via grid search BO approaches. CNN models are trained on every dataset via specified procedures and hyperparameters; performance is accessed via predetermined metrics. CNN algorithm strengths, shortcomings, and trends across medical datasets and sentiment analysis tasks are identified via comparative study findings. Patient privacy and data anonymizing in medical databases guarantee ethical issues. The research guarantees adherence to ethical standards, thereby offering insightful analysis for both fields. Researchers with objective definitions provide medical datasets, sentiment analysis challenges, CNN performance measures, and other goals. Choosing a dataset entails finding appropriate medical records for many imaging modalities and diseases. Preprocessing then provides medical image format and content data format compatibility for sentiment analysis by standardizing data handling across all datasets. With respect to both fields of Model Selection, researchers choose CNN architectures. Datasets should be statistically partitioned into training, validation, and test sets in order to achieve a balance in class representations in the experimental design. In the assessment, interpretation, and discussion stages, trained models are used to uncover strengths, weaknesses, performance trends, and CNN architectures/ datasets comparisons. Finally, the method ensures patient privacy, data anonymization, and bias minimization by considering ethical considerations. Using this technique, we can evaluate how well CNN algorithms perform in sensing and medical imaging.

However, Bandu *et al.* [21] fought counterfeit banknotes with image analysis and machine learning to boost financial security and fraud prevention . But deep learning model supposed to provide better accuracy. Sanjay *et al.* [22] studied smart home automation security using deep learning. Considering this research, the idea of smart home automation is used in present research. Tran *et al.* [23]examined filter widths and GCN reception information extraction enhances document processing. This research article provided the idea of image pre processing. Pandiyarajan and Valarmathi [24] introduced VDRNet19, dense residual DL network for dementia classification using VGG architecture improves dementia classification. But these models provide limited accuracy thus present study is considering advance CNN model. Jaganathan *et al.* [25] design novel style transfer method increases CNN generalization and model resilience. Figure 2 shows a thorough method for assessing the performance of CNN algorithms.

In Figure 2, the objectives are defined, dataset is selected. Then preprocessing and model selection takes place. The experimental design is developed for evaluation then interpretation and discussion is made for ethical considerations.

2.1. Contribution of Present Research

The current approach significantly advances CNNs in sentiment analysis and medical picture processing. It combines hybrid techniques combining CNNs [23, 24] with optimization techniques like dense residual networks and stochastic gradient descent to improve performance. Using results from related studies, this work addresses issues particular to several fields, like face expression sentiment classification and medical imaging anomaly detection. It also evaluates the weaknesses of present deep learning models and proposes fresh approaches to increase their generalizability and resilience. Apart from bridging some of the gaps in current approaches, this study provides a guide on how CNNs need to be used in different kinds of datasets going forward.

2.2. Hyper Parameters Configuration

Essential hyperparameters used in sentiment analysis CNN model design and optimization across many datasets as well as in medical imaging [30]. These hyperparameters have to be tuned to provide optimum performance:

i. Learning Rate: The learning rate finds the step size by repeatedly approaching the minimum of the loss function.
    - Relevance: A slower learning rate provides continuous convergence; a quicker one speeds training but runs the danger of overshooting.
    - Values Tested: Typical ranges include 0.001 to 0.01, with adjustments during hyperparameter tuning.

ii. Batch Size: The number of samples processed before the model's internal parameters are updated.
    - Relevance:While smaller batches provide for more frequent updates, which increases model generalization, larger batches increase computation efficiency.
    - Values Tested: 32.

iii. Epochs: The total count of times the training dataset has been passed is the number of epochs.
    - Relevance:The model could avoid overfitting and grasp the data's trends with enough training cycles.
    - Values Tested:Usually tested values fall between 10 and 100; early termination strategies are given if necessary.

iv. Optimizer: Training loss might be reduced using weight-adjusting algorithms such RMSprop, Adam, or SGD.
    - Relevance:The characteristics of the dataset define which optimizers fit the best.
    - Choices Explored: Adam (default for most tasks), SGD with momentum, and RMSprop.

v. Dropout Rate: A regularization technique to prevent overfitting by randomly setting a fraction of the input units to zero during training.
    - Relevance: Enhances model robustness and generalization.

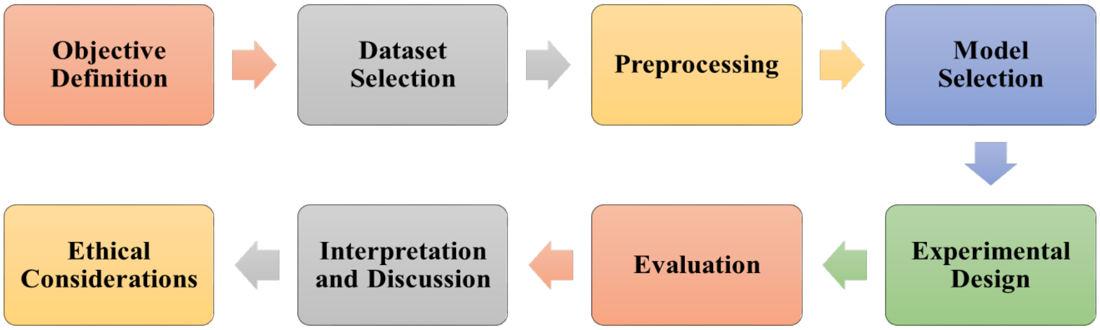

Fig. 2. Research methodology.

  - Values Tested: Common rates include 0.2, 0.4, and 0.5.

vi. Activation Function: specifies, for the next layer—ReLU, Sigmoid, or Softmax—the neuronal output transformation.
  - Relevance: ReLU is often used for hidden layers, while Softmax is ideal for the output layer in classification tasks.
  - Choices Explored: ReLU for hidden layers; Softmax or Sigmoid for output layers, depending on task type.

vii. Kernel Size: Specifies the filter size in convolutional layers.
  - Relevance: Determines how the model captures spatial features in images or sequential dependencies in text.
  - Values Tested:5x5.

viii. Regularization (L2, L1): Penalty terms added to the loss function to prevent overfitting by discouraging large weights.
  - Relevance: Ensures simpler models and better generalization.
  - Values Tested: L2 regularization using lambda values 0.001 and 0.01 tests values.

ix. Cross-Validation/Bootstrapping: Methods for reliably assessing models by splitting data into training and validation sets in various ways include bootstrapping and cross-valuation.
  - Relevance: Provides reliable predictions for many datasets.
  - Choices Used: Bootstrapping in addition to 5-fold cross-valuation was used for smaller datasets.

x. Metrics: Precision, accuracy, recall, and F1-score, are among the measures of model performance employed here.
  - Relevance: It denotes that the model's efficacy is seen holistically.
  - Focus: Consider medical dataset precision, sentiment analysis accuracy, and F1-score.

2.3. Process Flow of Proposed Work

Emphasizing sentiment analysis and medical imaging, the work's process flow seeks to identify challenges of evaluating CNN performance on different datasets. For relevance-that is, for skin cancer, kidney stones, brain tumors, and sentiment analysis-specific datasets are selected. Two preparation techniques that fit well include resize and adding content for sentiment analysis; furthermore, scaling and normalizing images for medical data Appropriate CNN [25] architectures like VGG, ResNet, and DenseNet are chosen based on the task criteria. Training, validation, and test include three sections to the datasets. Class balance is maintained and rigorous evaluation is done via cross-valuation or bootstrapping. Hyperparameter tuning—using grid search or Bayesian optimization—allows one to maximize learning rate, batch size, and other factors. CNN models trained with updated hyperparameters using optimization techniques like Adam or SGD are evaluated in part by accuracy, precision, recall, and F1-score. CNN performance as well as its strengths and shortcomings may be shown by means of comparison between CNNs on sentiment analysis and medical imaging datasets [30]. We give ethical issues like data anonymization and privacy great importance so that research complies with all the guidelines. We analyze the data to demonstrate how well CNNs perform in these particular contexts and provide recommendations on how to enhance them and where to go in terms of research shown in Table 1.

2.3.1. Steps in the process flow

i. Problem Identification: Determine the challenges in evaluating CNN performance on sentiment analysis and medical imaging datasets [30].

ii. Selecting and getting ready the database
  - Select suitable medical imaging databases, including those for brain cancer or kidney stones detection.
  - Select datasets for sentiment analysis—movie reviews, product reviews, etc.
  - Resizing photos or tokenizing content can help you to ensure compatibility by means of any required preparatory actions.

iii. CNN Architecture Selection: Choose CNN architectures [31] suitable for image classification, segmentation, and content analysis.

iv. Dataset Splitting
  - Divide datasets into training, validation, and test sets with balanced class representation.
  - Implement cross-validation or bootstrapping for robust evaluation.

v. Hyperparameter Tuning: Optimize key hyperparameters (e.g., learning rate, batch size, dropout rate) using grid search.

vi. Model Training: Use algorithms such as Adam or SGD to train CNN models with optimal hyperparameters.

vii. Model Evaluation: Consider measures like recall, accuracy, precision, F1-score, and AUC when assessing performance.

viii. Comparative Analysis: Conduct a comparative analysis to see patterns in performance and find areas of strength and improvement across different datasets.

ix. Ethical Considerations
  - Protect the privacy of patients and guarantee that their medical records are anonymized.
  - Eliminate prejudice from the process of selecting and evaluating datasets.

The Table 1 outlines key aspects of the machine learning model development. It includes CNN architectures such as VGGNet, which serves as a simple baseline, ResNet, which uses residual connections to address vanishing gradients, and Inception, which captures multi-scale features for better image understanding. The dataset preprocessing involves resizing images to 224 × 224 pixels, normalizing pixel values, augmenting data with transformations like flip and rotation, encoding labels, and using a stratified train-test split to maintain class balance. For hyperparameter tuning, a learning rate of 0.001, a batch size of 32, and early stopping with patience between 5-10 epochs are used, alongside SGD and Adam optimizers, and dropout rates ranging from 0.3 to 0.5. Evaluation metrics include overall accuracy, class-wise precision, recall, and F1-score, along with a confusion matrix for detailed performance analysis and tracking training/inference time to ensure efficiency. These elements work together to optimize model performance across tasks.

3. RESULTS AND DISCUSSION

The current study examines Skin cancer , Kidney Stone Detection, Brain MRI Tumor Detection, and Emotion Analysis datasets. The Skin cancer dataset [26] comprises dermatoscopic pictures of skin lesions, rendering it significant for image classification and segmentation in skin cancer diagnosis. Comprising medical images-ultrasound and CT scans-the Kidney Stone Detection [28] collection helps to categorize and diagnose kidney stones. Composed of MRI pictures categorized by tumor kind, the Brain MRI Tumor Detection [29] collection allows exact identification and classification of brain tumors. Comprising images of faces expressing emotions like as pleasure and rage, the Sentiment Analysis [32] collection in natural language processing is appropriate for categorizing emotions and studying sentiments. Developing research in medical imaging and natural language processing applications depends on these datasets.

3.1. Dataset

This paper offers a carefully selected collection of publicly accessible datasets pertinent to several fields of medical imaging and natural language processing. For experts and academics working on

Table 1. CNN-based model design considerations.

Aspect	Details
CNN Architectures Used	• VGG Net: Simple, deep network - good baseline. • ResNet: Uses residual connections to handle vanishing gradients. • Inception: Captures multi-scale features efficiently.
Dataset Preprocessing	• Image resizing to 224 × 224 pixels • Normalization of pixel values • Data augmentation: flip, rotate, zoom, contrast • Label encoding for categorical outputs • Stratified train-test split (e.g., 80/20)
Hyperparameter Tuning	• Learning rates: 0.001 • Batch sizes: 32 • Epochs: early stopping with patience 5-10 • Optimizers: SGD, Adam • Dropout: 0.3-0.5
Evaluation Metrics	• Accuracy for overall performance • Precision, Recall, F1-Score for class-wise insight • Confusion matrix for detailed class performance • Training/inference time

machine learning and deep learning applications within healthcare and affective computing, these datasets are very useful. The table below offers a brief summary of datasets connected to emotion identification, skin cancer detection, kidney stone diagnosis, and brain tumor analysis. Every entry has the dataset name, a short explanation stressing its contents and possible applications, and a direct access link to the dataset shown in Table 2.

Many datasets used for various machine learning applications are shown in Table 2. Valuable for skin cancer diagnosis by image classification and segmentation, the Skin Cancer dataset consists of dermatoscopic photos of skin lesions. Comprising medical images used to identify kidney stones via ultrasound or CT scans, the Kidney Stone Detection collection supports detection and classification activities. Comprising MRI pictures categorized by tumor kinds, the Brain MRI Tumor identification dataset helps to identify and classify brain cancers. Appropriate for emotion classification and sentiment analysis projects, the Emotion Analysis dataset finally consists of face samples marked with emotions like pleasure and fury. Advancing studies in natural language processing and medical imaging depends on these datasets.

3.2. Simulation

The conventional CNN approach makes use of testing and training data sets. Evaluation across tasks like Skin Cancer Detection [26], Kidney Stone Detection [28], Brain Tumor Detection [29], and Sentiment Analysis [32] reveals that CNN models often show good performance across all criteria. In brain tumor diagnosis, the model shows outstanding performance with an F1-score of 95%, recall and accuracy of 97%, and precision of 96%. With few false positives and negatives, these studies show the model's effectiveness in correctly categorizing brain cancers. With an F1-score of 95%, recall rates of 96% and 95%, and accuracy rates of 96%, Kidney Stone Detection shows consistent case identification and categorization. With a 95% accuracy rate, 95% recall and accuracy, and a little higher F1-score of 96%, Skin Cancer Detection shows quick and exact performance. With an F1-score of 95% and both recall and accuracy of 96%, the CNN model performs well in Sentiment Analysis, hence confirming its dependability in sentiment categorization. The results show that the CNN model can adapt and perform well in many areas; hence, it efficiently handles medical imaging and text-based sentiment classification. The findings show that CNN is a flexible and strong method for solving difficult classification tasks. Table 3 shows the outcomes for accuracy, precision, recall, and F1 score; Figure 3 offers a graphical depiction of the simulation. The table shows the performance measures of models across four separate detection tasks: Brain Tumor Detection, Kidney Stone Detection, Skin Cancer Detection, and Sentiment Research. With an accuracy of 97%, the model performs very well in Brain Tumor Detection, indicating its ability to precisely categorize most cases. A recall of 96% indicates that it effectively identifies most actual brain tumor cases; a precision of 96% indicates that when it forecasts a tumor, it is mostly right. A 95% F1-score shows a well-balanced effectiveness in tumor identification and categorization. The model

Table 2. Dataset and its description.

S. No.	Dataset Name	Description	Reference
1	Skin Cancer Detection	Dermoscopic pictures categorize cutaneous lesions as melanoma, nevus, and keratosis. These pictures are used for categorization and segmentation purposes.	[26, 27]
2	Kidney Stone Detection	Medical imaging and diagnostic criteria for the detection of nephrolithiasis via ultrasound or computed tomography. This method is particularly useful for tasks involving classification and detection.	[28]
3	Brain MRI Tumor Detection	MRI pictures classified as glioma, meningioma, pituitary tumor, and absence of tumor. These images are beneficial for the identification, segmentation, and categorization of brain tumors.	[29-31]
4	Sentiment Analysis	Facial picture examples annotated with emotions such as pleasure, rage, sadness, etc. These examples are ideal for tasks related to natural language processing, specifically sentiment and emotion categorization.	[32]

indicates reliable classification with 95% accuracy in Kidney Stone Detection. At 95% and 96%, the recall and accuracy show the ability of the model to find most kidney stones and lower false positives. A F1-score of 95% underlines even more the model's effectiveness in correctly classifying and spotting kidney stones. Ensuring correct identification of cases, the model achieves 95% accuracy and 95% recall in skin cancer detection. While an F1-score of 96% emphasizes the general effectiveness of the model in balancing detection and accuracy, a precision of 95% shows a low false positive rate. With 96% accuracy and 96% recall and accuracy, the Sentiment Analysis model shows its strong ability to properly classify feelings. The F1-score of 95% indicates that the model effectively balances recall and accuracy. The models exhibit outstanding performance in all challenges, underscoring their efficacy in practical applications for medical diagnosis and content analysis.

Table 3 is presenting comparative analysis of accuracy parameters in case of various applications such as retailer, logistic providers, manufacturers, suppliers. Considering the table's data, the figure would likely visualize the comparison of these performance metrics across all tasks. A bar chart could be used to depict accuracy, recall, precision, and F1-Score for each task, with each metric represented by a separate bar for clarity. Figure 3 highlights the consistency in performance across tasks, illustrating how well each model is trained to detect specific conditions (brain tumors, kidney stones, skin cancer) or analyze sentiment in facial expression. For example, the Brain Tumor Detection model might show the highest accuracy, while the Skin Cancer Detection model could have a slightly higher F1-score. This comparison would help emphasize the effectiveness of the models in various domains, showcasing their potential for real-world applications in both medical imaging and natural language processing.

3.3. Error Analysis

While the CNN model [25] performed well across all domains, some observations include:

- Class Imbalance: In medical datasets (especially skin cancer [26]), rare classes may still be underrepresented, leading to marginally lower recall in minority categories.
- Overfitting Risk: In some cases, especially with smaller datasets, the model showed signs of overfitting, which was mitigated using dropout, data augmentation, and early stopping.

Table 3. Comparison of accuracy parameters of CNN.

	Brain tumor detection	Kidney stone detection	Skin cancer detection	Sentiment analysis
Accuracy	0.97	0.95	0.95	0.96
Recall	0.96	0.95	0.95	0.96
precision	0.96	0.96	0.95	0.96
F1-score	0.95	0.95	0.96	0.95

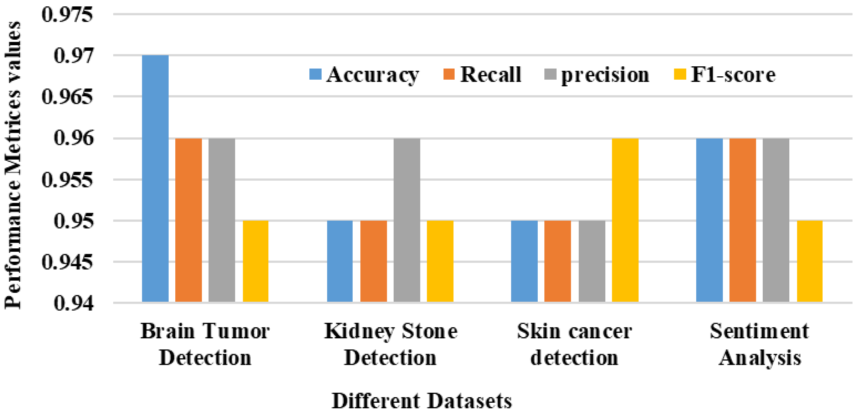

Fig. 3. Comparative analysis of accuracy parameters for various applications.

- Text Data Challenges: For sentiment analysis, sarcasm or nuanced emotional tones were sometimes misclassified, highlighting limitations in handling contextual ambiguity.

3.4. Model Limitations

Despite strong overall performance, the study acknowledges the following limitations:

- Domain-specific Optimization: CNN architectures [23] may require tuning or modifications for optimal performance across distinct domains, such as 2D medical imaging [30] vs. sequential text. Lack of Explainability: CNNs are often viewed as black boxes. Interpretability techniques (e.g., Grad-CAM for images or attention maps for text) were not implemented here.
- Cross-dataset Generalization: The current study does not explore transfer learning across datasets, which could reveal deeper insights into CNN flexibility.
- Computational Cost: Training deep CNNs, especially on large image datasets, is resource-intensive and may not be feasible in low-resource environments without optimization.

3.5. Aspect-Based CNNs Comparison

The current study demonstrates the remarkable performance of CNNs in many domains including content-based sentiment analysis and medical imaging (skin cancer detection [26], Kidney stone [28], brain tumor [29, 30]). The strong results achieved for accuracy parameters confirm the efficacy and flexibility of CNN architectures. Notwithstanding the encouraging results, certain significant limitations and areas for improvement still have to be acknowledged. One of the most major limitations of this study is the absence of comparison with evolving deep learning architectures. Reflecting a paradigm shift in computer vision, these models have now attained state-of-the-art performance on multiple test sets. Unlike CNNs, which rely on local receptive fields, transformers utilize self-attention methods to grab global connections in data, usually producing superior results, especially in large-scale datasets. Including such models in future studies would provide a more whole view of how CNNs function in respect to the most current advancements. The study also makes no particular reference to biases in the datasets used. Common dataset imbalance occurs, particularly in medical applications where certain disease categories might be underrepresented. Uneven model performance in which the classifier favors dominant classes and does not correctly generalize might follow from this. Linguistic or cultural disparities in the content corpus might lead to sentiment analysis biases. Without a thorough bias investigation, it is impossible to assess the fairness and reliability of the models across various populations or unknown data distributions. Future work should incorporate model performance audits across demographic groups, bias detection tools, and class balancing techniques to help to lower this. Another significant concern is overfitting, particularly in models trained on rather small data sets. Although the study employs traditional countermeasures like as dropout, early pausing, and data augmentation, it provides no comprehensive analysis or visualization of training vs validation performance trends. Without this, one struggles to know if the test set performance of the model is really generalizable or a consequence of overfitting shown in Table 4.

4. CONCLUSIONS

This study concentrates on assessing CNN efficacy across diverse datasets, particularly in sentiment analysis and medical imaging. The process includes issue identification, database selection, CNN architecture selection, dataset partitioning, hyperparameter optimization, model training, assessment, and comparative analysis. The work highlights ethical aspects such as data anonymization and privacy, aiming to illustrate CNN performance in certain circumstances and offer ideas for enhancement. The process includes class equilibrium maintenance, bootstrapping, and cross-validation. The study shows that CNNs are suitable for a number of uses, including brain tumor identification, renal stone detection, skin cancer diagnosis, and sentiment analysis. Compared to other approaches, CNN performs best in text-based sentiment classification and medical imaging. CNN is accurate, flexible, and rather strong. Often exceeding 95% in accuracy measures, the research shows CNN's dependability in generating accurate categorization outcomes. Addressing important issues like data preparation, model selection, hyperparameter optimization, and

Table 4. Comparison of convention model considering various aspects.

Aspect	Sentiment Analysis	Medical Imaging (Brain Tumor, Renal Stone, Skin Cancer)	Strengths of CNNs	Limitations & Areas for Improvement	Ref. No.
Application Domain	Emotion classification from content datasets (e.g., Emognition)	Detection of brain tumors, kidney stones, and skin cancer using CT/MRI images	Versatile across textual and image domains	Domain-specific adaptation may be required	[2, 33-35]
Accuracy	High accuracy in binary/multi-class classification tasks	High precision in abnormality detection in medical datasets	Strong performance in supervised learning tasks	No benchmarking with transformer-based models	[35, 36]
Feature Extraction	Captures local content features (e.g., sentiment-carrying words)	Captures spatial features like shape and intensity variations	Learns hierarchical feature maps	Limited ability to capture global dependencies	[37, 38]
Scalability	Effective on moderate datasets	Works well with curated medical datasets	Efficient with modest compute	May not scale well on extremely large or diverse datasets	[37, 39]
Bias Handling	Prone to linguistic and cultural biases	Imbalanced data (e.g., fewer rare diseases) causes class bias	Some resilience via data augmentation	No bias detection or fairness audit included	[40]
Overfitting Risk	Managed with dropout, small batch sizes	Higher in small dataset cases (e.g., rare diseases)	Regularization methods used (dropout, early stopping)	No validation vs training trend analysis provided	[36]
Comparison with State-of-the-Art	No comparison with transformers (e.g., BERT)	No comparison with hybrid models	CNNs remain strong for many tasks	Transformers often outperform CNNs in large-scale tasks	[41, 42]
Future Scope	Include demographic and bias-aware training	Address class imbalance and overfitting	Base for building deeper models	Use of transformers and fairness evaluation tools recommended	[41-43]

ethical concerns, the paper provides a thorough approach for evaluating CNN models. Apart from showing how CNNs may be used in many sectors, these results support the development of artificial intelligence systems for crucial tasks like medical diagnosis and emotion interpretation. This work adds notably to current understanding on deep learning by implying that it might increase accuracy and efficiency in addressing challenging real-world issues. Future developments in NLP and healthcare provide great promise to increase CNN algorithm performance in medical datasets and sentiment analysis. Future studies tackling problems including data scarcity, class imbalance, and medical dataset interpretability could focus on enhancing CNN architectures and techniques. Combining various data kinds with CNN models might provide a more complete view of patient information, hence supporting improved diagnosis, outcome prediction, and therapy planning.

5. CONFLICT OF INTEREST

The authors declare no conflict of interest.

6. REFERENCES

1. R.N.V.J. Mohan, B.H.V.S.R.K. Raju, V.C. Sekhar, and T.V.K.P. Prasad (Eds.). Algorithms in Advanced Artificial Intelligence. 1st Edition. *CRC Press, London, UK* (2025).
2. M. Esteva, B. Kuprel, R.A. Novoa, J. Ko, S.M. Swetter, H.M. Blau, and S. Thrun. Dermatologist-level classification of skin cancer with deep neural

networks. *Nature* 542(7639): 115-118 (2017).

3. S.R. Karra and A.K. Kakhandki. An extensive study of facial expression recognition using artificial intelligence techniques with different datasets. *Journal of Autonomous Intelligence* 6(2): 631 (2023).
4. A. Khan, S. Ullah, S. Ahmad, and H. Latif. Automated kidney stone detection in CT scans using convolutional neural networks. *Journal of Medical Imaging and Health Informatics* 11(8): 1980-1989 (2021).
5. S. Rajendra, K.G. Srinivas, and K.S. Rajasekaran. A Convolutional Neural Network-based framework for brain tumor detection from MRI images. *International Journal of Imaging Systems and Technology* 31(5): 432-445 (2021).
6. A. Alrahhal and K. Supreethi. Enhancing CNN performance through content-based image retrieval techniques. *International Journal of Computer Vision and Image Processing* 12(3): 45-56 (2021).
7. F.T. Zohra, R.T. Ratri, S. Sultana, and H.B. Rashid. Image segmentation and classification using neural network. *International Journal of Computer Science & Information Technology* (2025). https://doi.org/10.5121/ijcsit.2024.16102.
8. R. Silambarasan, K. Venkatesan, and P. Devi. Deep learning approach for the diagnosis of PCOS using medical imaging data. *Journal of Medical Imaging and Health Informatics* 14(2): 115-124 (2022).
9. R. Pandiyarajan and M.L. Valarmathi. Dementia classification using VDRNet19: A deep learning model for brain image analysis. *Computational Intelligence and Neuroscience* 2021: 8854362 (2021).
10. P. Bandu, T. Ramesh, and N. Shah. Hybrid deep learning models for counterfeit detection in digital transactions. *IEEE Transactions on Information Forensics and Security* 15: 3021-3030 (2020).
11. A. Debnath and U.K. Mondal. Leveraging CNN and principal component analysis for dynamic variance control in audio compression. *International Journal of Information Technology* 17(2): 1039-1047 (2024).
12. O. Olabanjo, A. Wusu, E. Aigbokhan, O. Olabanjo, O. Afisi, and B. Akinnuwesi. A novel graph convolutional networks model for an intelligent network traffic analysis and classification. *International Journal of Information Technology* (2025). https://doi.org/10.1007/s41870-024-02032-4.
13. M. Alrahhal and K.P. Supreethi. Integrating machine learning algorithms for robust content-based image retrieval. *International Journal of Information Technology* 16(8): 4995-5003 (2024).
14. E. Silambarasan, G. Nirmala, and I. Mishra. Polycystic ovary syndrome detection using optimized SVM and DenseNet. *International Journal of Information Technology* 17(2): 1039-1047 (2025).
15. A. Mishra, V.S. Jatti, D.A. Sawant, and A.S. Visave. Novel neurosymbolic artificial intelligence (NSAI) based algorithm to predict specific energy absorption in CoCrMo based architected materials. *International Journal of Information Technology* 17(2): 999-1005 (2025).
16. L. Alzubaidi, J. Zhang, A.J. Humaidi, A. Al-Dujaili, Y. Duan, O. Al-Shamma, J. Santamaría, M.A. Fadhel, M. Al-Amidie, and L. Farhan. Review of deep learning: concepts, CNN architectures, challenges, applications, future directions. *Journal of Big Data* 8(1): 53 (2021).
17. X. Zhao, L. Wang, Y. Zhang, X. Han, M. Deveci, and M. Parmar. A review of convolutional neural networks in computer vision. *Artificial Intelligence Review* 57: 99 (2024).
18. S. Cong and Y. Zhou. A review of convolutional neural network architectures and their optimizations. *Artificial Intelligence Review* 56: 1905-1969 (2023).
19. I. Rodriguez-Conde, C. Campos, and F. Fdez-Riverola. Optimized convolutional neural network architectures for efficient on-device vision-based object detection. *Neural Computing and Applications* 34: 10469 (2022).
20. A. Khan, A. Sohail, U. Zahoora, and A.S. Qureshi. A survey of the recent architectures of deep convolutional neural networks. *Artificial Intelligence Review* 53(8): 5455-5516 (2020).
21. S.C.D. Bandu, M. Kakileti, S.S.J. Soloman, and N. Baydeti. Indian fake currency detection using image processing and machine learning. *International Journal of Information Technology* 16(8): 4953-4966 (2024).
22. C. Sanjay, K. Jahnavi, and S. Karanth. A secured deep learning based smart home automation system. *International Journal of Information Technology* 16(8): 5239-5245 (2024).
23. A.C. Tran, B.T. Le, and H.T. Nguyen. Efficiency evaluation of filter sizes on graph convolutional neural networks for information extraction from receipts. *International Journal of Information Technology* (2025). http://dx.doi.org/10.1007/s41870-024-02089-1.
24. M. Pandiyarajan and R.S. Valarmathi. VDRNet19: a dense residual deep learning model using stochastic gradient descent with momentum optimizer based on VGG-structure for classifying dementia.

International Journal of Information Technology (2025). http://dx.doi.org/10.1007/s41870-024-02103-6.

25. A.P. Jaganathan. Meta-styled CNNs: boosting robustness through adaptive learning and style transfer. *International Journal of Information Technology* (2025). https://doi.org/10.1007/s41870-024-02150-z.
26. K. Mader. Skin Cancer MNIST: HAM10000. *Kaggle Datasets* (2018). https://www.kaggle.com/datasets/kmader/skin-cancer-mnist-ham10000.
27. K. Nawaz, A. Zanib, I. Shabir, J. Li, Y. Wang, T. Mahmood, and A. Rehman. Skin cancer detection using dermoscopic images with convolutional neural network. *Scientific Reports* 15: 7252 (2025).
28. O. Sejuti. Axial CT Imaging Dataset-Kidney Stone Detection. *Kaggle Datasets* (2022). https://www.kaggle.com/datasets/orvile/axial-ct-imaging-dataset-kidney-stone-detection.
29. N. Chakrabarty. Brain MRI Images for Brain Tumor Detection. *Kaggle Datasets* (2019). https://www.kaggle.com/datasets/navoneel/brain-mri-images-for-brain-tumor-detection.
30. Y. Xie, F. Zaccagna, L. Rundo, C. Testa, R. Agati, R. Lodi, D.N. Manners, and C. Tonon. Convolutional neural network techniques for brain tumor classification (from 2015 to 2022): review, challenges, and future perspectives. *Diagnostics (Basel)* 12(8):1850 (2022).
31. M. Taus, A. Tasneem, A. Al Mueed, and M.E. Islam. Convolutional Neural Network Based Framework for Classification of Brain Tumor from MRI Images. *IEEE 2023 International Conference on Information and Communication Technology for Sustainable Development (ICICT4SD)*, 21st - *23rd September 2023, Dhaka, Bangladesh* pp. 259-263 (2023).
32. S.A.M. Khan. Dataset on Emotion and Facial Detection. *Kaggle Datasets* (2023). https://www.kaggle.com/datasets/sardarabdulmoizkhan/emotiondetectiondataset.
33. E.S. Agung, A.P. Rifai, and T. Wijayanto. Image-based facial emotion recognition using convolutional neural network on Emognition dataset. *Scientific Reports* 14: 14429 (2024).
34. M. Shetty, S.B. Shetty, G.P. Sequeria, and V. Hegde. Kidney Stone Detection Using CNN. *27th Second International Conference on Data Science and Information System (ICDSIS), 17th - 18th May 2024, Hassan, India* (2024).
35. H.A. Khan, W. Jue, M. Mushtaq, and M.U. Mushtaq. Brain tumor classification in MRI image using convolutional neural network. *Mathematical Biosciences and Engineering* 17(5): 6203-6216 (2020).
36. D.P. Kingma and J.L. Ba. Adam: A Method for Stochastic Optimization. *International Conference on Learning Representations (ICLR), 7th - 9th May 2015, San Diego, USA* (2015). https://arxiv.org/abs/1412.6980.
37. Y. LeCun, Y. Bengio, and G. Hinton. Deep learning. *Nature* 521: 436-444 (2015). https://doi.org/10.1038/nature14539.
38. I. Goodfellow, Y. Bengio, and A. Courville (Eds.). Deep Learning. 1st Edition. *MIT Press, Cambridge, MA, USA* (2016).
39. F. Chollet (Ed.). Deep Learning with Python. 1st Edition. *Manning Publications, Shelter Island, NY, USA* (2017).
40. R. González-Sendino, E. Serrano, J. Bajo, and P. Novais. A Review of bias and fairness in artificial intelligence. *International Journal of Interactive Multimedia and Artificial Intelligence* 9(1): 5-17 (2024).
41. A. Dosovitskiy, L. Beyer, A. Kolesnikov, D. Weissenborn, X. Zhai, T. Unterthiner, M. Dehghani, M. Minderer, G. Heigold, S. Gelly, J. Uszkoreit, and N. Houlsby. An Image is Worth 16x16 Words: Transformers for Image Recognition at Scale. *International Conference on Learning Representations (ICLR), 3rd - 7th May 2021, Virtual Conference* (2021). https://arxiv.org/pdf/2010.11929.
42. J. Devlin, M.-W. Chang, K. Lee, and K. Toutanova. BERT: Pre-training of Deep Bidirectional Transformers for Language Understanding. *2019 Conference of the North American Chapter of the Association for Computational Linguistics: Human Language Technologies (NAACL-HLT), 1st - 6th June 2019, Minneapolis, Minnesota, USA* (2019). https://arxiv.org/pdf/1810.04805.
43. B.A. Plummer, L. Wang, C.M. Cervantes, J.C. Caicedo, J. Hockenmaier, and S. Lazebnik. Flickr30k Entities: Collecting Region-to-Phrase Correspondences for Richer Image-to-Sentence Models. *IEEE International Conference on Computer Vision (ICCV), 11th - 18th December 2015, Santiago, Chile* (2015). https://arxiv.org/pdf/1505.04870.

Proceedings of the Pakistan Academy of Sciences: A Physical and Computational Sciences 62(1): 67-80 (2025)
Copyright © Pakistan Academy of Sciences
ISSN (Print): 2518-4245; ISSN (Online): 2518-4253
http://doi.org/10.53560/PPASA(62-1)871

Pakistan Academy of Sciences

Research Article

Uncertainty Quantification and Enhancing Panic Disorder Detection using Ensemble and Resampling Techniques

Muazzam Ali[1*], Amina Shabbir[1], Muhammad Azam[2], M.U. Hashmi[2], Umair Ahmad[1], and Affan Ahmad[2]

[1]Department of Basic Sciences, Superior University, Lahore, Pakistan
[2]Department of Computer Sciences, Superior University, Lahore, Pakistan

Abstract: Panic disorder is one of the leading mental health problems that entail serials of extreme fear that can highly hinder an individual's activities of daily life. Sometimes, intervention is very important, understanding the problem is highly crucial. Unfortunately, some methods assist with diagnostics do not provide accuracy in identification. Using machine learning approaches can resolve this problem as accuracy can be improved with data-driven models. This paper used ensemble machine learning models, Random Forest, Bagging Classifier, and Balanced Bagging Classifier to identify panic disorder. Medical datasets usually have a class imbalance problem. Therefore, we performed resampling SMOTE, ADASYN, and Tomek Links. We evaluated these models by accuracy, precision, recall, F1 score, ROC AUC, Cohen's Kappa, uncertainty measures, aleatoric uncertainty, epistemic uncertainty, and predictive entropy. In our results, The Bagging Classifier was out performance with the highest accuracy (99.97%), recall (99.66%), F1-score (99.60%), and Cohen's Kappa (99.58%), minimal uncertainty metrics (aleatoric: 0.00062, entropy: 0.002003), establishing itself as the optimal model for panic disorder diagnosis. This study proves the effectiveness of ensemble learning and resampling methods for early panic disorder diagnosis and future mental health technologies.

Keywords: Panic Attack, Machine Learning, Synthetic Samples, Decision Trees, Predictive Analytics, Mental Health.

1. INTRODUCTION

The mental health known as panic disorder is typified by frequent, unplanned panic attacks [1]. A panic disorder is characterized by a sudden increase in anxiety or discomfort that lasts for only a few minutes and is accompanied by both psychological and physical symptoms [2, 3]. A fast heartbeat, perspiration, shaking, dyspnea, chest pain, lightheadedness, nausea, and a dread of losing control or passing away are some examples of these symptoms [4]. In contrast to normal anxiety, which frequently has recognizable triggers, panic attacks in people with panic disorder might happen suddenly or for no apparent reason. This unpredictability often leads to chronic fear about future attacks and behavioral adjustments, such as avoiding circumstances or places where attacks have previously happened [5, 6]. About 2-3% of the population is affected by panic disorder each year, which typically manifests in late adolescence or early adulthood. Compared to men, women are more likely to receive a diagnosis. Although the precise causes of panic disorder are unknown, a mix of biochemical, psychological, environmental, and hereditary variables are thought to be responsible [7, 8]. An individual's life may be severely impacted by untreated panic disorder, which can lead to substance abuse, hopelessness, agoraphobia, and avoidance behaviors.

However, effective solutions are available. Cognitive-behavioral therapy (CBT), the most recommended psychological remedy, helps people recognize and change the mental processes that trigger panic attacks [9-11]. One class of drugs that is effective in alleviating symptoms is selective serotonin reuptake inhibitors (SSRIs) [12-14]. Additionally, regular exercise, stress management, and relaxation techniques are lifestyle adoptions

---

Received: January 2025; Revised: February 2025; Accepted: March 2025

* Corresponding Author: Muazzam Ali <muazzamali@superior.edu.pk>

that aid recovery. The treatment of panic disorder, including early diagnosis and intervention, allows affected individuals to restore order to their lives, improve their functioning, and alleviate symptoms. Advanced data science and machine learning have further enhanced treatment and diagnostic options available to individuals suffering from this disorder. The mental health paradigm concerning the research, diagnosis, and even forecasting of panic disorder is undergoing a profound change due to the impact of data science and machine learning technologies [15]. These technologies analyze and predict outcomes using sophisticated algorithms, large datasets, and modern computation techniques. By applying data from wearable, psychological evaluations, and medical records, these systems can provide an effective early diagnosis and identification of panic disorder. Through predictive analytics, customized assessments can be conducted that link stressors, genetic indicators, and panic attacks, something that traditional methods would miss [16]. With wearable and mobile applications, physiologic and behavioral data can be monitored as they happen, enabling instant capture of data [17]. Machine learning models can boost therapeutic effectiveness and lessen the trial-and-error process by predicting the therapies most likely helpful to a specific patient [18]. Machine learning also aids in the discovery of unknown phenomena within massive quantities of data, such as social networks and electronic health records, to better comprehend the etiology, course, and comorbidities of panic disorder. The amalgamation of data science and machine learning into mental health creates an opportunity for more thorough and precise identification, diagnosis, and treatment of panic disorder [19, 20]. It, in turn, would minimize societal burden and optimize patient care.

Although there have been advancements in the diagnosis of mental disorders over the years, accurately diagnosing panic disorder is still particularly challenging due to its changing nature. It seems that traditional approaches to diagnosis are not adequate. However, the use of automatic diagnostic systems based on machine learning and data science models shows potential for better accuracy in diagnosis. An example of this is the class imbalance problem in medical datasets, which is a situation where one category contains a significantly lower sample size. This frequently leads to skewed results as well as challenges in detecting the minority cases. This paper looks at these issues applying Random Forest, Bagging Classifier, Balanced Bagging Classifier ensemble learning methods, and advanced resampling techniques like SMOTE, ADASYN, and Tomek Links that are focused on improving classification accuracy. This study proposes a novel framework for panic disorder detection which removes class imbalance while including quantification of uncertainty to increase model trustworthiness. Unlike past work on anxiety disorders, this research is focused on providing robust estimations which minimizes misclassification risk, enabling dependable mental health diagnostics.

2. MATERIALS AND METHODS

Panic disorders constitute a grave anxiety issue that poses potential risks to one's mental well-being. To deal with it, one must act quickly. Technology plays a great role in aiding early detection through data-driven methods. Classification must be on point to diagnose and treat panic disorder properly. Single- and multi-attribute generalizations performed by machine learning systems on unbalanced samples tend to overfit, resulting in poor generalization performance. Employing the Random Forest approach, this work analyzes the effectiveness of the classification of the acknowledged panic disorder datasets in the context of SMOTE handling overfitting. The results indicate that SMOTE is proven to greatly improve the Random Forest classification detection of panic disorder datasets, increasing accuracy by 15% [21]. This research proposes a technique for real-time detection of panic attacks leveraging wearable devices through the lens of human-computer interaction (HCI). The application predicts panic episodes by monitoring physiological parameters such as heart rate, heart rate variability (HRV), and electrocardiogram (ECG). These parameters are evaluated by a machine learning model based on CNN and SVM methods, where the system achieved great results revealed by eight percent accuracy, high user satisfaction, and low false positive rates. The system needs fine-tuning in further studies to help improve accuracy [22]. The work aimed to build a model capable of distinguishing panic disorder individuals from healthy subjects using machine learning. Eleven features were extracted from physiological reactions recorded during rest, stress, and recovery. The results showed key markers of

Parkinson's disease to be PT and ECG features during stress and recovery phases. The study's multilayer perceptron (MLP) achieved a maximum accuracy of 75.61% with 33 features. The study showed the capability of objective differentiation of people with Parkinson's disease by combining multimodal signals [23]. The relevance of different biometric and geographical parameters is examined for their significance in the overall process of panic detection, as described in reference [24]. A model for predicting panic attacks is based on 7 days of data gathered from wearable, passive sensors, and online questionnaires. The system integrates environmental, physiologic, and survey responses to predict panic attacks in advance. The overall accuracy is between 67.4 percent and 81.3 percent, which is driven mostly by the questions asked and the physiological attributes of the respondents. However, the focus of the study was narrowed down to patients who have panic disorder only [25]. Even though 95% of participants were able to identify a trigger, 11% of individuals suffer from panic attacks annually. A higher likelihood of panic attacks the next day was associated with lower mood, state-level mood, higher resting heart rate, and more background noise. This information could improve the specificity of one-session psycho-education programs and help direct ecological momentary treatments [26, 27].

According to cognitive-behavioral theories, perceived threat, and arousal-related bodily sensations produce a positive feedback loop that leads to panic attacks. A computational model suggests that a simulated disturbance of arousal is a good indicator of panic disorder and the likelihood of an attack. This study reviews the empirical literature on biological challenge reactions and their relationship to disorder and panic episodes. The results show a moderate association with recurring panic attacks but no association with panic disorder [28]. The study used digital phenotypes and machine learning algorithms to predict panic symptoms in patients with mood and anxiety disorders. For two years, 43 patients were monitored through wearable devices and smartphone applications. The XGBoost model also proved useful with additional features such as elevated anxiety, increased step counts, and Childhood Trauma Questionnaire results [29]. A machine learning-based technique was used to differentiate panic disorder from other forms of anxiety disorders using heart rate variability (HRV). Of the five algorithms that were employed, the L1-regularized LR showed the best accuracy. However, the study had limitations, including a limited sample size and a cross-sectional methodology. Future studies should use machine learning techniques to duplicate the diagnostic usefulness of HRV [30]. This study aimed to develop a dropout prediction model for cognitive behavioral therapy (CBT) for panic disorder using machine learning techniques. Two hundred eight patients received group cognitive behavioral therapy. The results showed excellent accuracy in predicting dropout during CBT for PD, with random forest achieving 88% accuracy and light gradient boosting machine achieving 85% accuracy. This machine-learning technology may help with clinical decision-making in typical clinical situations [31].

Panic disorder is a refractory mental condition that affects 5% of people worldwide and 10% of persons with subclinical symptoms. If untreated, it is a serious issue that can significantly harm individuals, families, and society. The prediction model of panic disorder is examined in this study using machine learning algorithms that simulate human learning processes. The results show that the artificial neural network model has the largest AUC (0.8255) and the shortest running time (less than 1 second) when compared to other models [32]. The study used machine learning to look at PD patients' brain networks. The results showed that the structural network, particularly the extended fear network, had changed. Increased connections to the insula, hippocampus, and amygdala were associated with better treatment response, while over-connectivity was associated with poor response. SVM and CPM can predict treatment outcomes based on changes in network patterns [33]. Robinaugh *et al.* [34] presented panic disorder symptoms as panic, chest pain, and tremors, afflicting 5% of the global population. Accurate diagnosis is crucial in the early stages of illness to maximize therapeutic efficacy. Among the many promising ML algorithms, artificial neural networks (ANN) appear to perform the best in predicting panic disorder, with AUC scoring 0.8255 and exceeding one second in processing speed. These discoveries fortify the argument for advancing predictive ML models for earlier discovery and preventative measures regarding panic disorder.

2.1. Methodology

This study uses a classification model with a resampling technique to develop a machine learning-based approach to detect panic disorder. Following sections demonstrate the process, which includes acquiring the dataset, data cleaning, feature engineering and transformation, exploratory data analysis, implementing techniques to resample and adjust for class imbalance, fitting the models, determining their performance, and quantifying the uncertainty.

2.1.1. Dataset acquisition and preprocessing

This study utilized a Kaggle dataset containing 100,000 entries featuring 17 attributes. Each entry is associated with an individual and captures various attributes, including a person's demographic details, family details, personal details, psychological stressors, symptoms, their severity, impact on daily activities, medical history, psychiatric history, substance use, coping strategies, social support, and lifestyle choices. The dataset also contains a binary variable capturing the existence and absence of panic disorder as the target variable. The dataset is largely imbalanced due to the large portion of not diagnosed with panic disorder, and thus, the patient group (those diagnosed with panic disorder) is significantly underrepresented in the dataset.

The dataset was uploaded and processed using Python libraries like Pandas, NumPy, and Scikit-learn. Categorical features were labeled via Label Encoding, transforming them to numerical values during the data loader's execution. This stage ensured that all features were numeric and, therefore, usable by machine learning algorithms. Examine the missing values and find no missing values. The standard scalar from Scikit-learn was used to perform feature scaling. This scalar standardizes features by removing the mean and scaling to unit variance. This process is important to ensure that models do not have their predicted outcomes skewed as a function of larger range features [35].

2.1.2. Addressing the issue of class imbalance

The study undertook measures to address class imbalance issues by leveraging multiple resampling methods such as SMOTE, ADASYN, and Tomek Links under-sampling. Through SMOTE, new instances are made in the feature space, increasing the generalization of the model by augmenting the representation of the minority class.

$$x_{new} = x_i + \gamma(x_j - x_i) \qquad (1)$$

Where,
x_i is a randomly chosen minority class sample,
x_j is one of its nearest neighbors in the feature space,
γ is a random number between 0 and 1, ensuring interpolation.
ADASYN improves SMOTE by creating synthetic samples that pay more attention to the difficult cases, which allows less bias in the model's predictions [38].

$$G_i = \bar{G}.\frac{r_i}{\sum_{i=1}^{n_m} r_i} \qquad (2)$$

Where,
G_i is the number of synthetic samples to generate. For instance x_i,
$\bar{G}$ is the total number of synthetic samples needed,
r_i is the ratio of majority class neighbors to total neighbors for x_i,
n_m is the number of minority class samples.
As an under-sampling technique, Tomek links focus on class separation by deleting instances of the nearest border from the majority class [39].

$$d(x_i, x_j) = \min_{x_k \in X} d(x_i, x_j) \qquad for\ all\ k \qquad (3)$$

These resampling methods were evaluated using stratified k-fold cross-validation to determine their effectiveness in improving model performance. Some other techniques for dealing with class imbalance, for instance, Random Under-sampling, Random Over-sampling, Cluster-based Over-sampling, and near-miss, have weaknesses that make them unsuitable for this research. Random Under-sampling has the potential to result in the loss of important information, and Random Over-sampling is problematic in that it is prone to over fitting by copying minority class instances. In particular, Cluster-based Over-sampling may be time-consuming to process and introduce potential prejudice. At the same time, NearMiss can make wrong speculations about data distributions and may lead to high-class overlap. In contrast, SMOTE, ADASYN, and Tomek Links represent more sophisticated approaches. SMOTE creates synthetic samples that increase the generalization ability; ADASYN is committed to identifying the hard instances to lower the bias. In contrast, Tomek Links is used to eliminate the near-border instances to clarify the class boundaries, ensuring a better performance, generalization, and less over fitting of the model, thus making them very good for detecting minority classes such as panic disorder.

2.1.3. Exploratory data analysis

During the exploratory phase of the analysis, we developed correlation matrices and histograms to understand the features' relations and distributions.

2.1.3.1. Correlation matrix: The heat map style correlation matrix was useful in spotting the presence of linear relationships between the features. This was beneficial for not only identifying multi-collinearity issues, but also feature selection redundancies [35]. Figure 1 displays the correlation heatmap of the Panic Disorder dataset, elaborating on important inter-variable relationships. The most significant aggravating associations were noted both for symptoms and their severity, which was less than 0.15, and more pronounced for panic disorder diagnosis which showed a greater than 0.26 value. This shows that more severe symptoms and greater likelihood of diagnosis are strongly correlated and aggravated in individuals with severe panic disorders. Furthermore, Lifestyle Factors show a moderate positive association toward the Panic Disorder Diagnosis with a coefficient near 0.26 suggesting some degree of lifestyle influence in regard to the condition diagnosis. In general, the heatmap provides insights into the role of Severity and Symptoms of panic disorder and its clinical significance. This information is useful for other researchers if they fine-tune their efforts in managing severity and lifestyle changes.

2.1.3.2. Histogram: The analysis of solitary characteristics distribution was carried out using histograms. This method allowed for detecting potential skewed distributions that could affect the model. Based on the histograms, log transformations, and normalization techniques that improve the accuracy and reliability of the model

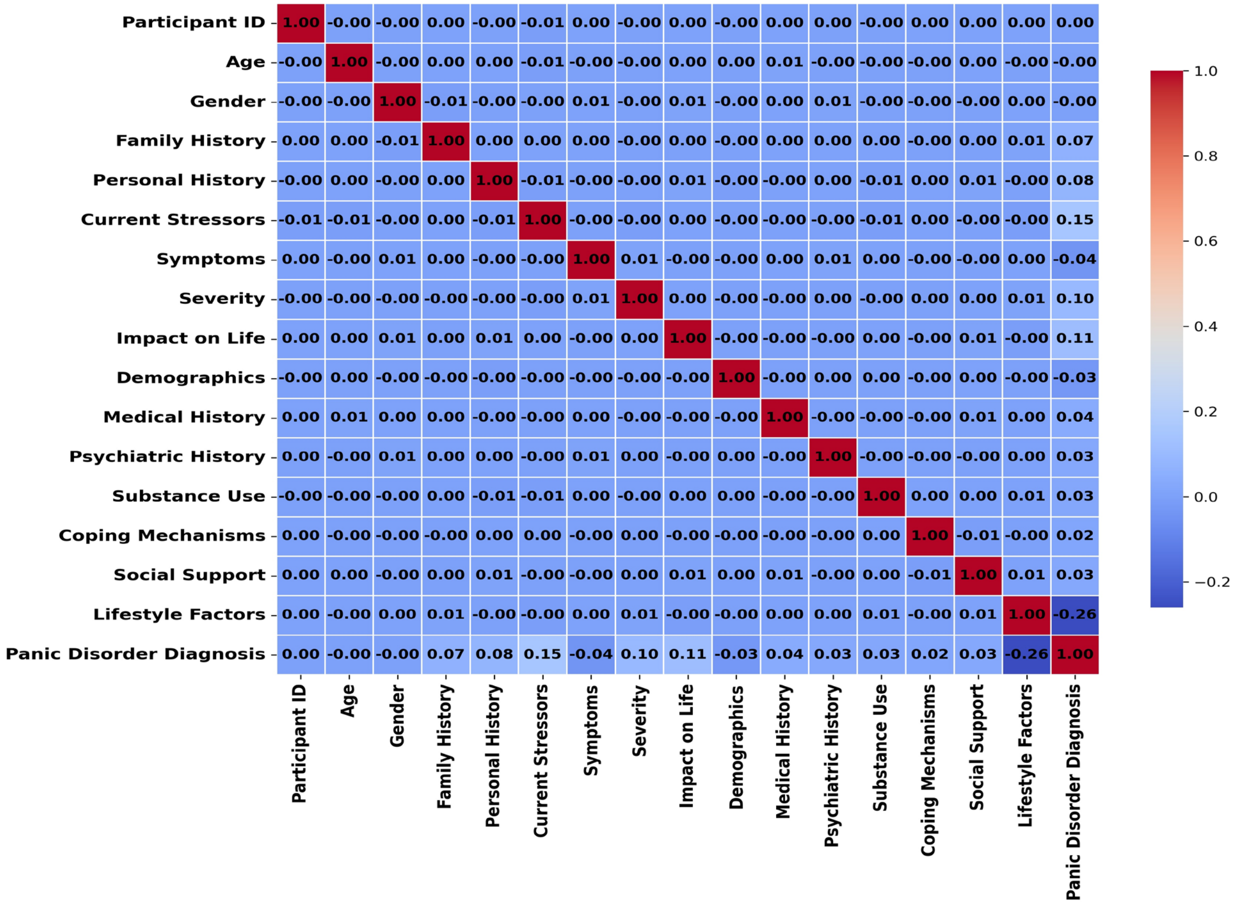

Fig. 1. Correlation heat map of variables in the panic disorder dataset.

were adopted [37]. Each histogram in Figure 2 indicates the distributions of features within the dataset's context, which gives us implications regarding the underlying patterns within the dataset. Most family history, personal history, and severity features demonstrate distinct binary or categorical features, which suggest clear categories with minimal or no intermediate cases. Features like age and gender have even distributions, which indicate a good level of diversified representation among the participants in the study. Reporting or categorizing current stressors, symptoms, and impacts on life will likely be dominated by a few prevalent patterns indicated by multimodal distribution. Medical history, psychiatric history, substance use, and coping mechanisms have features with distributions that appear to have several levels or categories, enriching the dataset with nuanced participant information. Social support and lifestyle factors showed the same level of clustering, suggesting that discrete levels of support and lifestyle habits are present. The disparity between these distributions

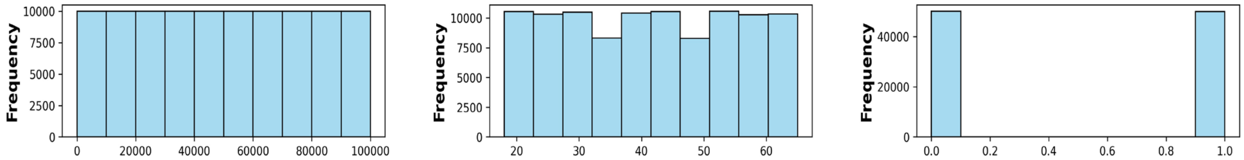

(a) Participant ID **(b) Age** **(c) Gender**

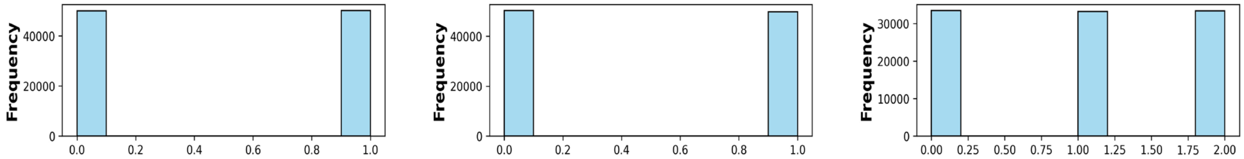

(d) Family History **(e) Personal History** **(f) Current Stressors**

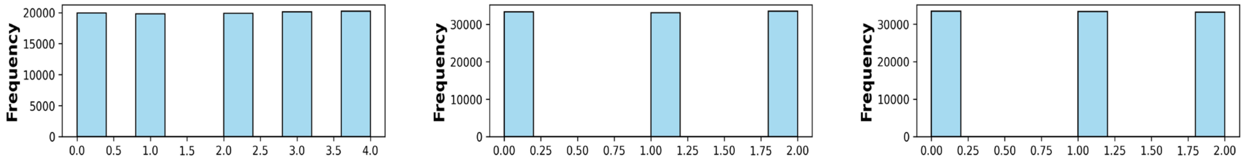

(g) Symptoms **(h) Severity** **(i) Impact on Life**

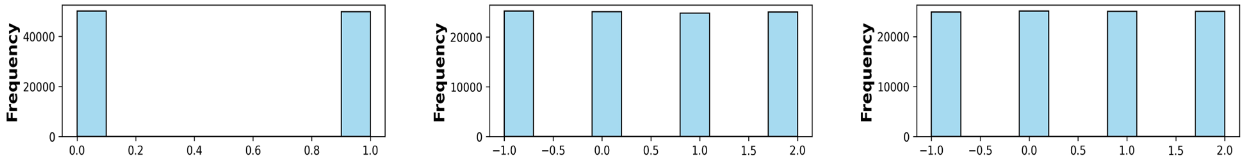

(j) Demographics **(k) Medical History** **(l) Psychiatric History**

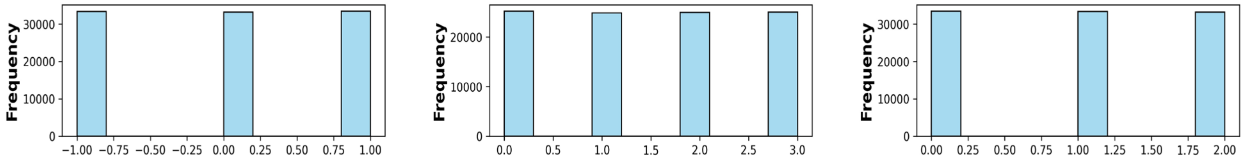

(m) Substance Use **(n) Coping Mechanisms** **(o) Social Support**

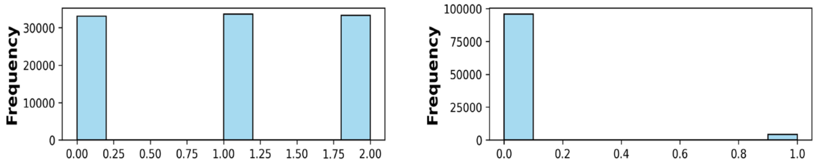

(p) Lifestyle Factors **(q) Panic Disorder Diagnosis**

Fig. 2. Distribution of variables in the panic disorder dataset.

indicates that the dataset will easily be subjected to classification techniques since it relies heavily on categorical or binary features.

2.1.4. Model training and evaluation

The classifiers used for this work included Random Forest, and Balanced Bagging Classifier. Random forest is an ensemble of classifiers with decision trees that works well with imbalanced data sets as class weight can be assigned. The Balanced Bagging Classifier is a class from an imbalanced learn library that uses bootstrap aggregation to balance the distribution of classes among samples [40-42]. Each model was developed using stratified k-fold cross-validation and five splits for the most accurate performance estimation. Accuracy, precision, recall, F1-score, and the area under the Receiver Operating Characteristic Curve (ROC AUC) were determined for each model-resample configuration. Accuracy, while a good measure of the overall correctness of model predictions, is difficult to interpret with imbalanced datasets. So precision assesses the value of positively predicted positives (PPV) while recall determines the rate of true positives captured by the model. The F1 score provides a balance between precision and recall and, thus, is a more appropriate metric with class imbalance.

$$Accuracy = \frac{TP+TN}{TP+TN+FP+FN} \tag{4}$$

$$precision = \frac{TP}{\mathrm{TP}+FP} \tag{5}$$

$$Recall = \frac{PT}{TP+FN} \tag{6}$$

Where TP is true positive, TN is true negative, FP is false positive, and FN is false positive.

$$F1\ Score = 2 \times \frac{Precision \times Recall}{Precision \times Recall} \tag{7}$$

$$\mathcal{K} = \frac{P_0 - P_e}{1 - P_e} \tag{8}$$

2.1.5. Estimation of uncertainty

This research focused on estimating aleatoric and epistemic uncertainties, as well as predictive entropy, to increase model accuracy. As stated in the previous section, aleatoric uncertainty stems from underlying noise in data sources and was measured as the variance of predicted probabilities. Higher aleatoric uncertainty indicates class distribution overlaps, and therefore, individual predictions become ambiguous due to noise. The variance of the predictive distribution is used to quantify aleatoric uncertainty:

$$Aleatoric\ Uncertainty = E_{p(y|x,\theta)[(y-E|y)^2]} \tag{9}$$

It can be approximated using the variance of Softmax probabilities:

$$\sigma^2 = \frac{1}{N}\sum_{i=1}^{N} p(y_i|x,\theta)(1 - p(y_i|x,\theta)) \tag{10}$$

$p(y_i|x,\theta)$ is predictive probability of class y.
N is the number of Monte Carlo dropout samples
θ represents the model parameter.
Due to the lack of training data, epistemic uncertainty denotes model uncertainty, which was estimated through the variance of probabilistic predictions from ensemble models.

$$Epistemic\ Uncertainty = Var\left[E_{p(\theta|D)} p(y_i|x,\theta)\right] \tag{11}$$

Monte Carlo dropout-based estimation is:

$$\sigma^2 = \frac{1}{T}\sum_{i=1}^{T} p(y_i|x,\theta)^2 - \left(\frac{1}{T}\sum_{i=1}^{T} p(y_i|x,\theta_t)^2 (1 - p(y_i|x,\theta_t))\right)^2 \tag{12}$$

T is the number of stochastic forward passes (MC Dropout), $p(y_i|x,\theta_t)$ is the probability of class y given x and model parameters at $t-th$ forward pass.

In addition, predictive entropy for model outputs was estimated using Shannon entropy [43]. These measures of uncertainty were used to evaluate the confidence of the model predictions and the additional data that needs to be collected to make the model more accurate.
It is computed using the Shannon entropy:

$$H[y_i|x] = -\sum_{i=1}^{C} p(y_i|x) \log p(y_i|x) \tag{13}$$

C is the number of classes and $p(y_i|x)$ is the predicted probability for class i.

2.1.6. Random forest

Random Forest is an ensemble learning approach that combines several weak classifiers to handle complicated problems. It comprises several decision trees that make predictions based on the majority vote of forecasts. Regression and classification issues are addressed by the supervised machine learning method, which uses decision trees. Decision trees display predictions from a sequence of feature-based splits using a tree structure resembling a flowchart. The root, decision, and leaf nodes are their three constituent parts. The root node is where population division begins; the nodes remaining after splitting a root node are known as the decision node, and the node that cannot be further divided is the leaf node. The *Gini Index* is used to identify which feature will be the root node. Mathematically, it can be written as:

$$\begin{aligned} Gini\ Index &= 1 - \sum_{i=1}^{n} (p_i)^2 \\ &= 1 - \left[(p_+)^2 + (p_-)^2\right] \end{aligned} \tag{14}$$

Where p_+ the probability of positive is class and p_- is the probability of negative class. Unlike other decision tree models, the Random Forest model is an ensemble learning algorithm that increases the model's accuracy and stability by training multiple decision trees in parallel. Each of the trees is trained using a different subset of the data, and the final result is determined by aggregating the outcomes of the trees. The class_weight = 'balanced' parameters are also of great use for datasets with imbalance problems, as they modify the weight of each class based on its prevalence. Other parameters of importance include n_estimators, which controls the number of decision trees in the forest with a default value of 100, max_depth, which limits how deep each tree can get and also starts as None, which allows trees to grow until all nodes are pure, and min_samples_split which determines the minimum sample count needed to split a node which is also set at two by default. Additionally, min_samples_leaf refers to the minimum number of samples to be required to form a leaf node, which starts at 1. max_features controls the number of features available for consideration of levels splits, and bootstrap = True signifies that without reserve sampling is used, meaning each of the trees is trained on a different sample set of the data. Using the random_state parameter guarantees that results will be the same across runs by setting a random seed to create trees (see Table 1).

2.1.7. Balanced bagging classifier

The Balanced Bagging Classifier is another ensemble method, which, like Random Forest, resolves the problem of imbalanced data by automatically combining imbalance handling classes with multiple decision tree learners. Balanced Bagging differs from Random Forest in that it also balances the class distribution for each bootstrapped sample by oversampling the minority class to the size of the majority class; this is done for all bootstrapped samples. This particular model helps manage highly imbalanced datasets. Key parameters are base_estimator, which by default implements a DecisionTreeClassifier as the base model, and n_estimators, with a default value of 10, which sets the count of base models in the ensemble. max_samples controls the proportion of the dataset for each model, and max_features defines the proportion of features to be used when fitting each base model. The former is set to 'None,' thus enabling all data to be used, whereas the latter is overridden to guarantee some degree of sparsity defined by the ratio s. The bootstrap parameter indicates whether or not bootstrapped sampling will be used, while the sampling_strategy='auto' parameter guarantees that the minority class will be scaled to the dominant class. Like the Random Forest, random_state sets a seed for reproducibility (see Table 1).

3. RESULTS AND DISCUSSION

The results showcase the performance of different machine learning models Random Forest, Bagging Classifier, and Balanced Bagging Classifier each evaluated with various resampling techniques, including SMOTE, ADASYN, and Tomek Links. A comparative analysis of key performance metrics such as accuracy, precision, recall, F1-score, ROC AUC, Cohen's Kappa, and uncertainty measures (aleatoric uncertainty, epistemic uncertainty, and predictive entropy) provides valuable insights into the models' effectiveness in detecting panic disorder.

3.1. Performance Evaluation of Random Forest

Table 2 shows that the accuracy performed by the baseline Random Forest model was 0.99805, giving perfect precision with a value of 1.0. However, the model's recall was comparatively lower at 0.955682. Due to this disparity, the model is quite sensitive as it demonstrates missing a notable portion of true positive cases while identifying positive cases with high confidence. The SMOTE also automated the recall improvement and F1 score to 0.977363 and

Table 1. Hyperparameters used for the model.

Model	Hyperparameter	Value
Random Forest	class_weight	'balanced' (handles imbalanced classes)
	n_estimators	Default (100)
	max_depth	Default (None, trees expand until pure leaves)
	min_samples_split	Default (2)
	min_samples_leaf	Default (1)
	max_features	Default ('auto,' square root of the number of features)
	Bootstrap	Default (True, bootstrap sampling used)
	random_state	Default (None, random seed set by the OS)
Balanced Bagging Classifier	base_estimator	Default (DecisionTreeClassifier)
	n_estimators	Default (10)
	max_samples	Default (1.0, 100% of data used for each estimator)
	max_features	Default (1.0, 100% of features used for each estimator)
	Bootstrap	Default (True, bootstrap sampling used)
	sampling_strategy	Default ('auto,' balances data by making minority class size equal to majority class)
	random_state	Default (None, random seed set by the OS)

Table 2. Evaluation metrics results.

Model	Accuracy	Precision	Recall	F1-Score	ROC AUC	Cohen's Kappa
Random Forest	0.99805	1	0.95568	0.97733	0.99999	0.97632
Random Forest with SMOTE	0.99903	1	0.97736	0.98854	0.99999	0.988043
Random Forest with ADASYN	0.99915	0.999762	0.98039	0.98997	0.99999	0.989527
Random Forest with TomekLinks	0.99839	1	0.96242	0.98083	0.99999	0.979999
Bagging Classifier	0.99965	0.99546	0.99659	0.99602	0.99991	0.995842
Balanced Bagging with SMOTE	0.99931	0.9923	0.99159	0.99194	0.99996	0.991585
Balanced Bagging with ADASYN	0.99942	0.99232	0.99416	0.99323	0.99997	0.992934
Balanced Bagging with TomekLinks	0.99738	0.942666	0.99976	0.97035	0.99996	0.968983

0.988549, respectively. These changes indicate much better recall, especially in the lower class instances. This enhancement comes from SMOTE's ability to balance the dataset automatically, and as the model learns, it can define issues more cohesively. Like that, recall for Random Forest with ADASYN rose to 0.980397 while achieving a higher F1 score of 0.989971 compared to SMOTE. ADASYN performs better than SMOTE when learning the model's generalization because it is based on harder-to-classify instances requiring new synthetic samples. The opposite was true for the Random Forest with Tomek Links. When the comparison was made, the recall dropped to 0.962427, lower than previously achieved. However, the precision remained the same at 1.0. Although, the Tomek Links methodology suffers sensitivity as it is an under-sampling approach. In Table 3, uncertainty metrics revealed additional insights. Compared to models that utilized SMOTE and ADASYN, the baseline Random Forest model had relatively greater values in its aleatoric uncertainty (0.010129) and predictive entropy (0.036515). These values did drop somewhat with the use of SMOTE and ADASYN. These drops in values do demonstrate a greater degree of confidence in the predictions due to better balanced training data. Nonetheless, epistemic uncertainty fluctuated much less, suggesting consistent model performance irrespective of the resampling technique (Figure 4).

3.2. Performance of Bagging Classifier and Balanced Bagging Classifier

The Bagging Classifier demonstrated exceptional performance, achieving an accuracy of 0.99965 alongside a remarkable recall of 0.996591 and an F1 score of 0.996025. The model performed optimally due to the ability of the ensemble to cut down on variance and issues arising from overfitting. Surprisingly, aleatoric uncertainty was much lower (0.00062), and predictive entropy was also very low (0.002003), suggesting that the model was highly confident in its predictions and, therefore, the model was quite reliable. The balanced ensemble approach already solves the problem of disproportionate class distribution and, therefore, does not require resampling. Once again, applying SMOTE and ADASYN techniques proved beneficial for the Balanced Bagging Classifier. Balanced Bagging with SMOTE achieved a 0.99931 accuracy score, 0.991599 recall, and F1-score of 0.991945. ADASYN achieved slightly better results than SMOTE, with a recall of 0.994166 and an F1 score of 0.993237 (Figure 3). It proves that the targeted sampling techniques employed by ADASYN accurately overcame restrictions posed by the minority class (see Table 2). It is also worth noting that both models retained low levels of uncertainty, with aleatoric uncertainty being approximately 0.00068 and predictive entropy sitting at 0.0021. It can be taken as a sign of the robustness of the models. As for the Balanced Bagging Classifier trained with Tomek Links, the results were mixed. Although the model achieved a remarkable recall of 0.999767, the precision dropped to 0.942666, resulting in a lower F1-score of 0.970352, as shown in Table 3. It suggests that while the model could correctly identify almost all positive cases, it also had too many false positives. The increase in aleatoric uncertainty (0.004502) and predictive entropy (0.013946) indicates that the model had

Table 3. Uncertainty results of the data set with different classifiers.

Model	Aleatoric Uncertainty	Epistemic Uncertainty	Predictive Entropy
Random Forest	0.010129	0.030084	0.036515
Random Forest with SMOTE	0.009757	0.032701	0.036485
Random Forest with ADASYN	0.009711	0.032793	0.03621
Random Forest with TomekLinks	0.010639	0.028976	0.038413
Bagging Classifier	0.00062	0.04143	0.002003
Balanced Bagging with SMOTE	0.00068	0.040308	0.002127
Balanced Bagging with ADASYN	0.000749	0.040301	0.002311
Balanced Bagging with TomekLinks	0.004502	0.042529	0.013946

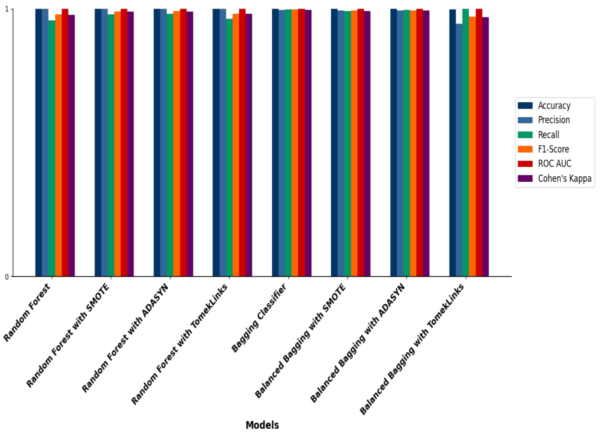

Fig. 3. Comparative analysis of evaluation matrices.

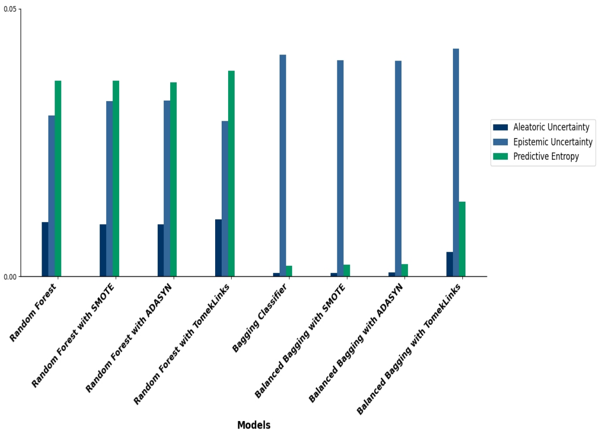

Fig. 4. Comparative analysis of uncertainties.

less confidence due to the more radical removal of borderline samples done by Tomek Links (see Figure 4).

3.3. Comparative Insights

While comparing to [24], it can be noticed that our models, particularly Random Forest with ADASYN (99.915% Accuracy), have shown marked and significant improvement in accuracy over the Gaussian SVM (94.5%). The application of resampling methods, particularly ADASYN, has greatly improved classification performance, surpassing raw features and HRMAD results [24]. These findings resonated in [21], where SMOTE was reported to increase the accuracy of Random Forest from 82% to 97%, demonstrating the positive effects of resampling on class imbalance and overall model performance. In regards to precision and recall, our models outperform previously published results. For example, Random Forest with ADASYN also attained one of the highest recorded precision scores of 0.999762 and recall scores of 0.98039, outperforming the precision (0.632) and recall (0.667) scores in [30] for Random Forest. The results from [30] indicate that integrating ADASYN and other ensemble changes is much more effective in decreasing false positives and true negatives than models. Additionally, our F1-Score results with Random Forest with ADASYN (0.98997) and Bagging Classifier (0.99602) far exceed [30] SVM (0.733) and Logistic Regression (0.790), meaning that our models achieve a preferable balance between recall and precision. It indicates that ensemble methods such as Bagging are more effective at optimizing the balance between false positive and negative rates than traditional methods. Our models achieve almost perfect values (0.99999) for ROC AUC, far exceeding the AUC of 0.8255 recorded for ANN in [34]. This sharp deviation reinforces the claim that my models, particularly those with resampling techniques, remarkably outperformed previous models in distinguishing panic disorder from other conditions. Moreover, the remarkably high Cohen's Kappa score (0.989527) accompanies my results, demonstrating divergence from those values against the consensus that he was predicting outcome targets, bolstered by the previously cited Kappa of 0.298 from Random Forest in [30], highlighting that his assertion was closer to the reality.

The uncertainty metrics set out in Table 3 are indicators of considerable disparities in a model's performance. It has been noted that using a Random Forest with TomekLinks (a preprocessing method for cleaning up the data and reducing the imbalanced training set) has increased the aleatoric uncertainty, which is the noise of the prediction and the class overlap, indicating that the model is facing greater difficulty in distinguishing between the classes. This higher uncertainty resulted in unreliable classification. However, epistemic uncertainty, which exhibited model uncertainty due to either a limit in the data or insufficient learning, did not exhibit consistent fluctuations instead of moving up and down among models, which would have suggested that the model, even with the resampling technique used, is still having a good performance. It is also notable that the predictive entropy, which is a concept of what the prediction's uncertainty is about, is quite much lower in the case of the Bagging Classifier models as a result of their solid confidence and stability in classification (see Figure 3). It gives a cue that methods like Bagging, which uses ensembles, are much more capable of giving accurate predictions while at the same time reducing the uncertainty compared to other approaches.

In summary, ensemble models, specifically the Balanced Bagging Classifier with ADASYN, recorded the best balance between performance metrics and uncertainty measures. This research also illustrates the importance of resampling methods to improve model sensitivity and reliability, which requires a specific framework depending on the nature of the data set.

4. CONCLUSIONS

This research shows the advanced applications of ensemble machine learning techniques using Random Forest, Bagging Classifier, and Balanced Bagging Classifier that diagnose panic disorder utilizing SMOTE, ADASYN, and Tomek Links for class imbalance resampling. Notably, the Balanced Bagging Classifier with ADASYN outperformed the competition by achieving greater accuracy, recall, precision, and F1 scores combined with low uncertainty metrics, which signify strong and dependable predictions. The addition of uncertainty quantification reduced the chances of misclassification while increasing rationale within the model, thereby making the model more useful from a clinical standpoint. Despite promising results, further analysis utilizing diverse datasets alongside real-time data from wearable devices can augment performance and adaptability. This work illustrates the significant impacts of using machine learning in diagnostics within the mental health field, thereby providing a benchmark for developing efficient and tailored treatments for panic disorders and psychiatry in general.

5. ACKNOWLEDGMENT

The authors are greatly indebted to the Superior University, Lahore, for providing all the necessary material and funding for this research. We thank the colleagues of the Department of Basic Sciences and the Department of Computer Sciences for their valuable comments and guidance.

6. ETHICAL STATEMENT

All research involving medical data was done ethically using best practices, which was done by the protocols set up. The Institutional Review Board reviewed the protocol for this study at the Superior University of Lahore, Pakistan. In this study, all materials were handled confidentially and remained anonymous.

7. CONFLICT OF INTEREST

The authors have no conflict of interest regarding this article.

8. REFERENCES

1. A.E. Meuret, J.L. Kroll, and T. Ritz. Panic disorder comorbidity with medical conditions and treatment implications. *Annual Review of Clinical Psychology* 13(1): 209-240 (2017).
2. L. Spytska. Exploration of personality characteristics of individuals with panic attacks: A personality profile study. *Journal of Infant, Child, and Adolescent Psychotherapy* 84(1): 84-94 (2025).
3. M.G. Abrignani, N. Renda, V. Abrignani, A. Raffa, S. Novo, and R. Lo Baido. Panic disorder, anxiety, and cardiovascular diseases. *Clinical Neuropsychiatry* 11(5): 130-144 (2014).
4. A.M. Krypotos, G. Mertens, D. Matziarli, I. Klugkist, and I. M. Engelhard. Fear generalization in individuals with subclinical symptoms of panic disorder. *Behaviour Research and Therapy* 1(184): 104649 (2025).
5. P. Porcelli. Fear, anxiety, and health-related consequences after the COVID-19 epidemic. *Clinical Neuropsychiatry* 17(2): 103-111(2020).
6. J.F. Brosschot, B. Verkuil, and J.F. Thayer. The default response to uncertainty and the importance of perceived safety in anxiety and stress: An evolution-theoretical perspective. *Journal of Anxiety Disorders* 41(1): 22-34 (2016).
7. M.G. Craske, M.B. Stein, T.C. Eley, M.R. Milad, A. Holmes, R.M. Rapee, and H.U. Wittchen. Anxiety disorders. *Nature Reviews. Disease Primers* 3: 17024 (2017).
8. B. Bandelow, D. Baldwin, M. Abelli, C. Altamura, B. Dell'Osso, K. Domschke, N.A. Fineberg, E. Grünblatt, M. Jarema, E. Maron, and D. Nutt. Biological markers for anxiety disorders, OCD, and PTSD–a consensus statement. Part I: Neuroimaging and genetics. *The World Journal of Biological Psychiatry* 17(5): 321-365 (2016).
9. S.G. Hofmann (Ed.). An Introduction to Modern CBT: Psychological Solutions to Mental Health Problems. *John Wiley & Sons* (2011).
10. N.R. Rayburn and M.W. Otto. Cognitive-behavioral therapy for panic disorder: A review of treatment elements, strategies, and outcomes. *CNS Spectrums* 8(5): 356-362 (2003).
11. S.G. Farri, L. Derby, and M.M. Kibbey. Getting comfortable with physical discomfort: A scoping review of interoceptive exposure in physical and mental health conditions. *Psychological Bulletin* 151(2): 131-191 (2025).
12. G. Chouinard and V.A. Chouinard. A new classification of selective serotonin reuptake inhibitor withdrawal. *Psychotherapy and Psychosomatics* 84(2): 63-71 (2015).
13. S.S. Clevenger, D. Malhotra, J. Dang, B. Vanle, and W.W. Ishak. The role of selective serotonin reuptake inhibitors in preventing relapse of major depressive disorder. *Therapeutic Advances in Psychopharmacology* 8(1): 49-58 (2018).
14. D. Lochmann and T. Richardson. Selective serotonin reuptake inhibitors. In: Antidepressants. Handbook of Experimental Pharmacology. M. Macaluso and S. Preskorn (Eds.). Volum 250. *Springer Nature Switzerland* pp. 135-144 (2018).
15. U. Madububambachu, A. Ukpebor, and U. Ihezue. Machine learning techniques to predict mental health diagnoses: A systematic literature review. *Clinical Practice and Epidemiology in Mental Health* 20: e17450179315688 (2024).
16. F. Akhtar, M.B.B. Heyat, A. Sultana, S. Parveen,

H. Muhammad Zeeshan, S.F. Merlin, B. Shen, D. Pomary, J. Ping Li, and M. Sawan. Medical intelligence for anxiety research: Insights from genetics, hormones, implant science, and smart devices with future strategies. *Wiley Interdisciplinary Reviews: Data Mining and Knowledge Discovery* 14(6): e1552 (2024).

17. G. Prieto-Avalos, N.A. Cruz-Ramos, G. Alor-Hernandez, J.L. Sánchez-Cervantes, L. Rodriguez-Mazahua, and L.R. Guarneros-Nolasco. Wearable devices for physical monitoring of heart: A review. *Biosensors* 12(5): 292 (2022).
18. E.A. Poweleit, A.A. Vinks, and T. Mizuno. Artificial intelligence and machine learning approaches to facilitate therapeutic drug management and model-informed precision dosing. *Therapeutic Drug Monitoring* 45(2): 143-150 (2023).
19. N.K. Iyortsuun, S.H. Kim, M. Jhon, H.J. Yang, and S. Pant. A review of machine learning and deep learning approaches on mental health diagnosis. *Healthcare* 11(3): 285 (2023).
20. K. Nova. Machine learning approaches for automated mental disorder classification based on social media textual data. *Contemporary Issues in Behavioral and Social Sciences* 7(1): 70-83 (2023).
21. D. Nurmalasari, H.R. Yuliantoro, and D.H. Qudsi. Improving panic disorder classification using SMOTE and random forest. *Journal of Applied Informatics and Computing* 8(2): 272-279 (2024).
22. P. Sahebi. Enhancing user experience for real-time panic attack detection with wearable technology: A human-computer interaction approach with machine learning integration. *International Journal of Advanced Human-Computer Interaction* 2(2): 55-66 (2024).
23. E.H. Jang, K.W. Choi, A.Y. Kim, H.Y. Yu, H.J. Jeon, and S. Byun. Automated detection of panic disorder based on multimodal physiological signals using machine learning. *ETRI Journal* 45(1): 105-118 (2023).
24. I. Lazarou, A.L. Kesidis, G. Hloupis, and A. Tsatsaris. Panic detection using machine learning and real-time biometric and spatiotemporal data. *ISPRS International Journal of Geo-Information* 11(11): 552 (2022).
25. C.H. Tsai, P.C. Chen, D.S. Liu, Y.Y. Kuo, T.T. Hsieh, D.L. Chiang, F. Lai, and C.T. Wu. Panic attack prediction using wearable devices and machine learning. Development and cohort study. *JMIR Medical Informatics* 10(2): e33063 (2022).
26. E.W. McGinnis, B. Loftness, S. Lunna, I. Berman, S. Bagdon, G. Lewis, M. Arnold, C.M. Danforth, P.S. Dodds, M. Price, and W.E. Copeland. Expecting the unexpected: Predicting panic attacks from mood, Twitter, and Apple Watch data. *IEEE Open Journal of Engineering in Medicine and Biology* 5(1): 14-20 (2024).
27. I.H. Bell, S.L. Rossell, J. Farhall, M. Hayward, M.H. Lim, S.F. Fielding-Smith and N. Thomas. Pilot randomised controlled trial of a brief coping-focused intervention for hearing voices blended with smartphone-based ecological momentary assessment and intervention (SAVVy): Feasibility, acceptability and preliminary clinical outcomes. *Schizophrenia Research* 216: 479-487 (2020).
28. D.J. Robinaugh, M.J. Ward, E.R. Toner, M.L. Brown, O.M. Losiewicz, E. Bui, and S.P. Orr. Assessing vulnerability to panic: A systematic review of psychological and physiological responses to biological challenges as prospective predictors of panic attacks and panic disorder. *General Psychiatry* 32(6): e100140 (2019).
29. S. Jang, T.H. Sun, S. Shin, H.J. Lee, Y.B. Shin, J.W. Yeom, Y.R. Park, and C.H. Cho. A digital phenotyping dataset for impending panic symptoms: A prospective longitudinal study. *Scientific Data* 11(1): 1264 (2024).
30. K.S. Na, S.E. Cho, and S.J. Cho. Machine learning-based discrimination of panic disorder from other anxiety disorders. *Journal of Affective Disorders* 278: 1-4 (2021).
31. S. Ogawa. Predicting dropout from cognitive behavioral therapy for panic disorder using machine learning algorithms. *Journal of Clinical Medicine Research* 16(5): 251 (2024).
32. C.H. Tsai, P.C. Chen, D.S. Liu, Y.Y Kuo, T.T Hsieh, D.L Chiang, F. Lai and C.T Wu. Panic attack prediction using wearable devices and machine learning: development and cohort study. *JMIR Medical Informatics* 10(2): e33063 (2022).
33. C. Pae, H.J. Kim, M. Bang, C.I. Park, and S.H. Lee. Predicting treatment outcomes in patients with panic disorder: Cross-sectional and two-year longitudinal structural connectome analysis using machine learning methods. *Journal of Anxiety Disorders* 106(2): 102895 (2024).
34. D.J. Robinaugh, J. Haslbeck, L.J. Waldorp, J.J. Kossakowski, E.I. Fried, A.J. Millner, R.J. McNally, O. Ryan, J. de Ron, H.L. van der Maas and E.H. van Nes. Advancing the network theory of mental disorders: A computational model of panic disorder. *Psychological Review* 131(6): 1482 (2024).
35. R. Rajendran and A. Karthi. Heart disease prediction using entropy-based feature engineering and

ensembling of machine learning classifiers. *Expert Systems with Applications* 20(7): 117882 (2022).

36. X. Peng, W. Wu, Y. Zheng, J. Sun, T. Hu, and P. Wang. Correlation analysis of land surface temperature and topographic elements in Hangzhou, China. *Scientific Reports* 10(1): 10451 (2020).
37. O.L. Usman, R.C. Muniyandi, K. Omar, and M. Mohamad. Gaussian smoothing and modified histogram normalization methods to improve neural-biomarker interpretations for dyslexia classification mechanism. *PLoS One* 16(2): e0245579 (2021).
38. F. Gurcan and A. Soylu. Synthetic boosted resampling using deep generative adversarial networks: A novel approach to improve cancer prediction from imbalanced datasets. *Cancers* 16(23): 4046 (2024).
39. S. Nouas, L. Oukid, and F. Boumahdi. Syngo: Synthetic genetic oversampling technique for textual data. *Social Network Analysis and Mining* 15(1): 9 (2025).
40. S.S. Dhaliwal, A.A. Nahid, and R. Abbas. Effective intrusion detection system using XGBoost. *Information* 9(7): 149 (2018).
41. A.S. More and D.P. Rana. Review of random forest classification techniques to resolve data imbalance. *Proceedings of the 2017, 1st International Conference on Intelligent Systems and Information Management (ICISIM)* pp. 72-78 (2017).
42. S. Hido, H. Kashima, and Y. Takahashi. Roughly balanced Bagging for imbalanced data. *Statistical Analysis and Data Mining. The ASA Data Science Journal* 2(5-6): 412-426 (2009).
43. E. Hüllermeier and W. Waegeman. Aleatoric and epistemic uncertainty in machine learning: An introduction to concepts and methods. *Machine Learning* 110(3): 457-506 (2021).

Proceedings of the Pakistan Academy of Sciences: A Physical and Computational Sciences 62(1): 81-95 (2025)

ISSN (Print): 2518-4245; ISSN (Online): 2518-4253
http://doi.org/10.53560/PPASA(62-1)869

Pakistan Academy of Sciences

Research Article

A Study on CIGS Thin-Film Solar Cells Through SCAPS-1D Simulations

Ateeq ul Rehman[1], Shahbaz Afzal[2], Iqra Naeem[1], Tahir Munir[1], Sakhi Ghulam Sarwar[3], Muhammad Saleem[1], and Raphael M. Obodo[4*]

[1]Institute of Physics, Baghdad ul Jadeed Campus, The Islamia University of Bahawalpur, Bahawalpur, Pakistan
[2]Department of Physics, University of Education Lahore, D.G. Khan Campus, Pakistan
[3]Centre of Excellence in Solid-State Physics, University of the Punjab, Lahore, Pakistan
[4]Department of Physics and Astronomy, University of Nigeria, Nsukka, Enugu State, Nigeria

Abstract: This research utilized SCAPS-1D simulation software to model a high-efficiency CIGS-based solar cell with configuration Ag/ZnO:Al/i-ZnO/CdS/CIGS/Mo. Various optimizations were performed, focusing on the absorber layer's thickness, defect density, and acceptor density to enhance the cell's performance. Moreover, the work function values of rear contact metals were studied in regard to their effect on important V_{oc}, J_{sc}, FF, and PCE steps in critical photovoltaics parameters. Their Influence was compared alongside temperature, highlighting the importance of reliable thermal control systems for sustained performance under changing conditions. The study further emphasized the importance of the hole transport layer (HTL) in improving charge carrier collection and reducing recombination losses. Efforts to develop cadmium-free designs reinforced the push towards sustainable and eco-friendly photovoltaic technologies. The optimal parameters achieved in this study included an absorber layer thickness of 0.4 µm, acceptor density of absorber at 1×10^{18} cm^{-3}, defect density of 1×10^{15} cm^{-3}, and a back contact selenium work function of 5.9 eV. Under AM 1.5 G spectrum illumination at 300 K, the optimized cell demonstrated exceptional performance, with a V_{oc} of 0.7338 V, J_{sc} of 36.352805 mA/cm^2, FF of 83.33%, and PCE of 22.23%. The results were benchmarked against existing literature, showcasing significant improvements in device efficiency. This study provides a comprehensive framework for optimizing CIGS-based solar cells and highlights their potential for delivering high-performance, sustainable solar energy.

Keywords: SCAPS 1D, Thin Films, Solar Cell, CIGS, Simulations.

1. INTRODUCTION

For last many years, scientists have devoted considerable resources to investigating renewable energy sources as sustainable alternatives to fossil fuels primarily due to their finite availability and significant environmental impact. Fossil fuels release substantial quantities of carbon dioxide, a greenhouse gas that significantly contributes to the expedited progression of climate change. Furthermore, the extraction and consumption of these finite resources result in significant environmental deterioration, encompassing air and water contamination. At the same time, their restricted availability engenders apprehensions regarding the sustainability of energy resources in the long term [1-3]. Photovoltaic (PV) energy has emerged as a promising solution for pursuing a sustainable and more environmentally friendly future [4-5]. PV technology focuses on converting sunlight into electrical energy, offering the potential to reduce dependence on finite fossil fuels, mitigate greenhouse gas emissions, and facilitate a shift toward clean, renewable energy sources [6]. Consequently, renewable energy has increasingly focused on materials that have high

---

Received: June 2024; Revised: February 2025; Accepted: March 2025
* Corresponding Author: Raphael M. Obodo <Raphael.obodo@unn.edu.ng>

energy conversion efficiency with environmentally sustainable [7]. Ongoing research and development efforts have increasingly focused on cells composed of III-VI materials like InSe, GaSe, and GaS, demonstrating significant potential for advancing solar energy production while maintaining environmental sustainability. A key consideration in this field is optimizing the efficiency-to-cost ratio, a crucial factor driving the advancement of thin-film solar cell materials. Chalcopyrite-based solar cells typically feature a substantial absorbent layer (up to 2 μm in thickness), capable of efficiently capturing a vast portion of the solar spectrum. Chalcogenide photovoltaic technologies, as a novel alternative to conventional silicon-based systems, offer exciting opportunities for advancing solar cell performance and cost-effectiveness [8-10].

The continuous progress in thin-film solar cell technology has attracted significant scholarly interest in recent years, especially concerning enhancing materials like Copper Indium Gallium Selenide (CIGS). Numerous studies have demonstrated the potential of CIGS-based solar cells to attain elevated power conversion efficiencies (PCE) while addressing the challenges of cost and scalability. For instance, Abdulmageed *et al.* [11] verified that CIGS solar cells can achieve PCE values exceeding 20% under laboratory conditions Specifically, Islam *et al*. [12] work with a CIGS absorber layer having a thickness of 1 μm has been shown to reach an efficiency of approximately 17% while Das *et al.* [13] laboratory-reported efficiencies range between 12% and 13%.

Notably, the study by Goncalves *et al*. [14] explored the effect of reducing the thickness of the CIGS absorber layer, demonstrating the potential for achieving theoretical efficiencies as high as 33%. Despite these remarkable results, the widespread adoption of CIGS thin-film solar cells remains constrained by the high cost of indium and gallium. However, their unique attributes, such as tunable band gaps, high absorption coefficients, and excellent external stability, continue to position CIGS cells as a promising contender for next-generation photovoltaic technologies [15]. Recent studies have further refined the performance of CIGS devices by optimizing material parameters. For example, Hossain *et al.* [16] achieved a PCE of 23% by optimizing various CIGS parameters. Danladi *et al.* [17] reported an efficiency of 22.58% through similar optimization efforts. In addition to the previous studies, other scholars have concentrated on augmenting the scalability and cost-effectiveness of devices based on Copper Indium Gallium Selenide (CIGS). For example, Muzakkar *et al.* [18] examined innovative doping methodologies to improve carrier mobility and the overall efficacy of the devices. Likewise, Smith *et al.* [19] investigated alternative fabrication techniques to mitigate dependence on indium while maintaining optimal performance. These synergistic endeavors underscore the persistent advancements achieved to elevate the efficiency and economic viability of CIGS thin-film solar cells, reinforcing their significance in the shift toward sustainable energy solutions.

This study proposes a novel CIGS-based solar cell structure with Cadmium Sulfide (CdS) as a buffer layer. This material is widely adopted in thin-film solar cells due to its favorable properties. The use of CDs offers several advantages, including efficient charge carrier separation, excellent optical properties, chemical stability, tunability, cost-effectiveness, and compatibility with various deposition techniques, making it a preferred choice for enhancing the performance and reliability of CIGS-based photovoltaic devices [20, 21]. The proposed Ag/ZnO:Al/i-ZnO/CdS/CIGS/Mo solar cell model was comprehensively analyzed, exploring various parameters to optimize its performance and implementation. Key factors, such as the thickness of the absorber, acceptor density, and defect densities, were systematically varied to understand their impact on power conversion efficiency (PCE) and overall device stability. Additionally, the study evaluated the influence of rear contact materials, operating temperatures, different hole transport layers HTLs, and alternative buffer layers to identify the most effective configuration for achieving enhanced photovoltaic performance. Prior studies have demonstrated the potential of CIGS solar cells, but limited attention has been given to exploring alternative buffer materials such as SnS_2, In_2S_3, and ZnSe, as well as different hole transport layers (HTLs) like CuI and Spiro-OMeTAD, and rear contact materials. This study is distinguished by its methodical optimization of the structural parameters inherent to the CIGS solar cell, aimed at realizing elevated efficiencies alongside economic efficiency. Innovative features encompass the incorporation of CdS as the buffer layer and the subsequent assessment of its influence on the comprehensive photovoltaic performance. The results yield critical insights into the architecture of high-performance CIGS-based solar cells that possess practical scalability and economic feasibility. Prospective research trajectories will emphasize the amalgamation of advanced materials with CIGS-based frameworks to augment efficiency and stability further. Furthermore, initiatives will be concentrated on formulating cost-effective and environmentally sustainable fabrication methodologies to promote the extensive implementation of CIGS thin-film solar cells within the renewable energy landscape.

2. METHODOLOGY

The utilization of SCAPS 1D in this simulation study is based on the one-dimensional solar cell capacitance program created and upheld by Marc Burgelman and his research team at the Department of Electronics and Information Systems at the University of Ghent in Belgium [15]. SCAPS 1-D functions by solving key semiconductor equations, which include the Poisson equation, continuity equations for electrons and holes as shown in Equations (1-3) [22-24].

$$\frac{d^2}{dx^2}\varphi(x) = \frac{e}{\varepsilon_0\varepsilon_r}\rho(x) - n(x) + N_D - N_A + \rho_P\rho_N \quad (1)$$

$$-\left(\frac{1}{q}\right)\frac{\partial J_P}{dx} + \mathrm{U}_P + G = \frac{\partial P}{\partial t} \quad (2)$$

$$-\left(\frac{1}{q}\right)\frac{\partial J_n}{dx} + \mathrm{U}_n + G = \frac{\partial n}{\partial t} \quad (3)$$

Where, $\varphi(x)$ denotes the electrostatic potential, e represents the elementary charge, ε_r stands for relative permittivity, ε_0 is the vacuum permittivity, p and n indicate concentrations of holes and electrons, N_A and N_D are for acceptor and donor densities respectively. Additionally, ρ_n and ρ_p describe electron and hole distributions, while J_n and J_p represent current densities for electrons and holes. G signifies the carrier generation rate in Equations (2) and (3).

2.1. Materials and Layer Details

The solar cell architecture investigated in his research comprises multiple layers, each serving a distinct purpose in optimizing device performance. The primary materials used in the solar cells include: soda-lime glass substrate provides mechanical support for the solar cell structure. Molybdenum (Mo) is employed as the back contact due to its excellent electrical properties and thermal stability. The absorber layer, composed of Copper Indium Gallium Selenide (CIGS), is the key sunlight absorber and is vibrant in converting photons into charge carriers. The Cadmium Sulfide (CdS) buffer layer is crucial for aligning the energy bands and facilitating efficient charge carrier transport among the absorber and window layer. To address environmental concerns, alternative buffer materials like Tin disulfide (SnS_2), Indium Sulfide (In_2S_3), and Zinc Selenide (ZnSe) are suggested to substitute CdS due to concerns regarding cadmium in solar cells. Furthermore, Intrinsic Zinc Oxide (i-ZnO) is used as a window layer to improve light scattering and increase photon absorption. The transparent conducting oxide (TCO) layer consists of Aluminum-doped Zinc Oxide (ZnO:Al), which improves electrical conductivity and reduces sheet resistance. Additional materials such as Copper Iodide (CuI) and Spiro-OMeTAD are examined as hole transport layers (HTLs) to enhance charge carrier collection and reduce recombination losses [25, 26].

2.2. Solar Cell Construction

The architecture of the solar cell is designed as Ag/ZnO:Al/i-ZnO/CdS/CIGS/Mo, with layers constructed sequentially on a sod-lime glass substrate. The Molybdenum (Mo) back contact layer is deposited first, providing a stable base for the subsequent layer and ensuring good electrical contact. Next, the CIGS absorber layer is deposited, followed by the CdS buffer layer, which ensures proper band alignment for efficient charge transport. Intrinsic Zinc Oxide (i-ZnO) is then applied as the window layer to optimize the light scattering and absorption. The Aluminum-doped Zinc Oxide (ZnO:Al) TCO layer, with a thickness of 500 nm, is added on top to enhance conductivity and improve carrier mobility. Finally, Silver (Ag) is applied as the front contact to complete the structure. The proposed design also incorporates modifications to address cadmium-related concerns by substituting buffer materials such as SnS_2, In_2S_3, and ZnSe and incorporating CuI and Spiro-oMeTAD as hole transport layers. These modifications aim to improve solar cell performance and sustainability, as shown in Figure 1. The intrinsic properties of each layer are defined by assigning explicit defects to their particular elements, as outlined in Tables (1-3).

3. RESULTS AND DISCUSSION

3.1. Mechanism of Solar Cells

Solar cells operate on the principle of the photovoltaic effect, which is the generation of electric current when a material captivates light energy. The process begins when sunlight illuminates the solar cell. Photons with energies equal to or greater than the bandgap energy of the absorber material (such as CIGS in this study) are absorbed, exciting electrons from the valence band to the conduction band. This excitation creates electron-hole pairs, which are the fundamental charge carriers in the solar cell [27]. A PN junction is employed in the solar cell structure to couple the energy of these charge carriers. The PN junction creates an internal electric field that separates the electron-hole pairs. Electrons are driven towards the N-type layer, while holes are pushed towards the P-type layer. This separation prevents recombination of the charges and allows them to move towards their respective electrodes. The front and back contacts of the solar cell collect the electrons and holes. The collected electrons flow through an external circuit, creating an electric current, while the holes flow to the back contact to complete the circuit. Several factors, including the material properties, the thickness of the absorber layer, the defect density, and the alignment of energy bands between the layers, influence the efficiency of this process. The role of the transparent conducting oxide (TCO), such as ZnO:Al, is to allow sunlight to pass through to the absorber layer while facilitating the movement of charge carriers. The buffer layer, such as CdS or cadmium-free alternatives like In_2S_3, aligns the energy bands between the absorber and the TCO, ensuring efficient charge transport. The back contact, such as molybdenum (Mo), facilitates the collection of holes and ensures good ohmic contact with the absorber layer [11-15, 28].

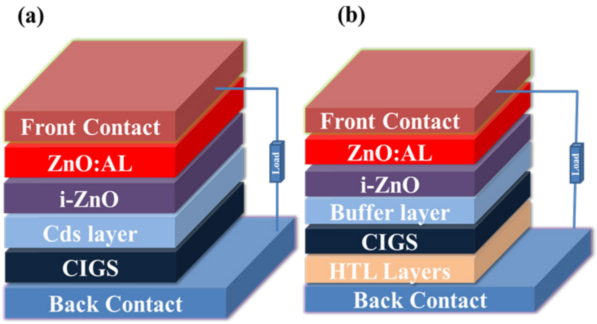

Fig. 1. (a) CIGS-based-simulated fundamental structure of solar cells, (b) CIGS-based solar cell with different buffer and hole layers.

This investigation presents an innovative solar cell architecture designated as Ag/ZnO:Al/i-ZnO/CdS/CIGS/Mo, which, following an extensive review of existing literature, appears to be unreported in the context of comparative analysis. The originality of this research is manifested in its benchmarking of performance metrics against other established configurations, such as Ag/ZnO:Al/ZnO/CdS/Sb_2Se_3/Mo, which attained a power conversion efficiency (PCE) of 8.72%, and CdS/Sb_2Se_3/Mo/

Table 1. Different used simulation parameters.

S. No.	Electrical Parameter	CIGS [25]	CdS [5]	i-ZnO [5]	ZnO:AI [5]
1	Bandgap (eV)	1.2	2.4	3.3	3.3
2	Dielectric permittivity (eV)	13.6	10	9	9
3	Thickness (µm)	2	0.05	0.05	0.5
4	CB (cm^{-3})	2.2×10^{18}	2.2×10^{18}	2.2×10^{18}	2.2×10^{18}
5	VB (cm^{-3})	1.8×10^{19}	1.8×10^{19}	1.8×10^{19}	1.8×10^{19}
6	Electron affinity (eV)	4.5	4.2	4.45	4.45
7	Electron mobility (cm^2/Vs)	1×10^2	1×10^2	1×10^2	1×10^2
8	Hole mobility (cm^2/Vs)	2.5×10^1	2.5×10^1	2.5×10^1	2.5×10^1
9	N_D (cm^{-3})	0	1×10^{17}	1×10^{15}	1×10^{18}
10	N_A (cm^{-3})	1×10^{16}	1×10^2	1×10^1	1×10^1
11	N_t (cm^{-3})	1×10^{15}	1×10^{15}	1×10^{10}	1×10^{17}

Table 2. Parameters of additional Buffer and Hole transport layer.

S. No.	Parameter	ZnSe [5]	SnS_2 [5]	In_2S_3 [5]	Spiro-Metad [26]	CuI [26]
1	Bandgap (eV)	2.4	2.45	2.8	3	3.1
2	CB (cm^{-3})	2.2×10^{18}	7.32×10^{18}	1.8×10^{19}	2.8×10^{18}	2.8×10^{19}
3	VB (cm^{-3})	1.8×10^{19}	1×10^{19}	4×10^{18}	1.8×10^{10}	1×10^{19}
4	Dielectric permittivity (eV)	10	17.7	13.5	3	6.5
5	Electron affinity (eV)	4.2	4.26	4.7	2.2	2.1
6	Thickness (µm)	0.05	0.05	0.025	0.2	0.1
7	N_D (cm^{-3})	1×10^{17}	9.85×10^{18}	1×10^{22}	0	0
8	N_A (cm^{-3})	1×10^{2}	0	0	1×10^{18}	1×10^{18}
9	Electron mobility (cm^2/Vs)	1×10^{2}	2.5×10^{1}	4×10^{2}	2.1×10^{-3}	1×10^{2}
10	Hole mobility (cm^2/Vs)	2.5×10^{2}	5×10^{1}	2.1×10^{2}	2.16×10^{-3}	4.39×10^{11}
11	Defect density (N_t)	1×10^{14}	1×10^{15}	1×10^{14}	1×10^{15}	1×10^{15}

Table 3. Front and Back contact values [29].

Electrical properties		Back contact	Front contact
Allow contact tunneling	Electron & holes	1×10^{7}	1×10^{7}
	Work function	5.6286	4.4903
	Relative to EF & E_C	0.0714 & -0.1227	0.0403 & 0.0019
	The effective mass of electrons & holes	1 and 1	1 and 1
Optical properties	Filter mode & value	Reflection & 0.8	Transmission & 0.95
	Complement of filter value	0.2	0.05

Ni, which realized a PCE of 23.39%. Alternative configurations, including $ZnSe/Sb_2Se_3$ and In_2S_3/Sb_2Se_3, exhibited 22.98% and 23.02% efficiencies, respectively. In contrast, the proposed configuration achieved remarkable results as shown in Table 4. This inquiry elucidates the advantages inherent in utilizing CIGS as an absorber layer instead of its Sb_2Se_3-based counterparts, exemplifying enhanced photovoltaic performance. Furthermore, the research accentuates the importance of optimizing material combinations to realize elevated efficiency levels. The outcomes of this study underscore the relevance of this novel configuration as a competitive and sustainable alternative for advancing thin-film solar cell technologies, thereby facilitating further optimization and practical application. Table 4 presents the difference between already presented work and previous work.

Figures (2-4) provide key insights into the performance and structure of CdS-based solar cells. Figure 2(a) shows the recombination curve, which highlights the rate at which charge carriers recombine within the solar cell, impacting efficiency. Figure 2(b) presents the I-V characteristic curve, essential for understanding the electrical behavior and efficiency of the solar cell under different operating conditions. Figure 3(a) illustrates the quantum efficiency (QE) curve, demonstrating the ability of the solar cell to convert incident photons into electrical current. Figure 3(b) depicts the photon energy curve, revealing the relationship between photon energy and the absorption efficiency of the solar cell. Lastly, Figure 4 displays the energy band diagram of the CdS-based solar cell, showing the alignment of energy levels across various layers, which is crucial for efficient charge carrier transport and overall device performance.

3.2. Impact of Absorber Layer Thickness

The absorber layer plays a vital role in solar cell performance for several reasons. It is the region where electron-hole pairs are primarily generated

Table 4. Comparison of this study with previous studies.

S. No.	Structure	V_{oc} (V)	J_{sc} (mA/cm²)	FF (%)	PCE (%)
1	Ag/ZnO:Al/ZnO/CdS/Sb_2Se_3/Mo	0.43	32.17	62.20	8.72 [2]
2	CdS/Sb_2Se_3/Mo/Ni	0.78	35.45	84.14	23.39 [2]
3	ZnSe/Sb_2Se_3	0.78	35.41	82.70	22.98 [2]
4	$In2S_3$/Sb_2Se_3	0.78	35.19	83.41	23.02 [2]
5	Ag/ZnO:Al/ZnO/CdS/CIGS /Mo	0.795	35.93141	82.8	20.98 (This work)
6	Ag/ZnO:Al/ZnO/ZnSe/CIGS /Mo	0.705	35.93147	82.8	20.98 (This work)
7	Ag/ZnO:Al/ZnO/SnS_2/CIGS /Mo	0.7048	35.92011	83.04	21.02 (This work)
8	Ag/ZnO:Al/ZnO/SnS_2/CIGS /Mo	0.7049	35.959757	83	21.04 (This work)
9	Ag/ZnO:Al/ZnO/SnS_2/CIGS /Mo	0.7338	36.352805	83.33	22.23 (Optimized result)

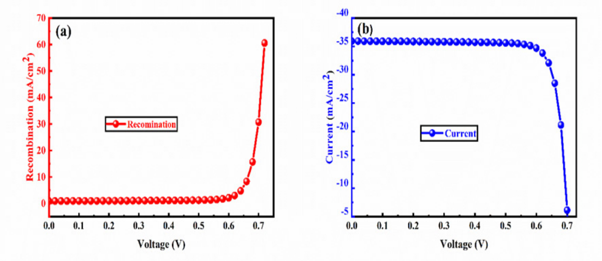

Fig. 2. (a) Recombination curve of CdS-based solar cell and (b) I-V characteristic curve of CdS-based solar cell.

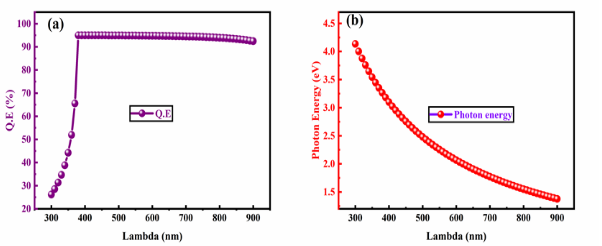

Fig. 3. (a) Quantum efficiency (QE) curve of CdS-based solar cell and (b) photon energy curve of CdS-based solar cell.

and constitutes a significant portion of the device's thickness. This characteristic is true for both silicon wafer and thin-film solar cell technologies. However, thin-film solar cells hold an advantage over wafer-based cells, as they can be much thinner and flexible, typically with thicknesses measured in microns. In contrast, wafer-based solar cells can be as thick as 200 µm [30]. To determine the optimal configuration, simulations were carried out using absorber layer thicknesses ranging from 2.0 to 4.0 µm, specifically analyzing the CIGS structure with a CdS buffer layer. Results indicated that increasing the thickness of the CIGS absorber layer enhances

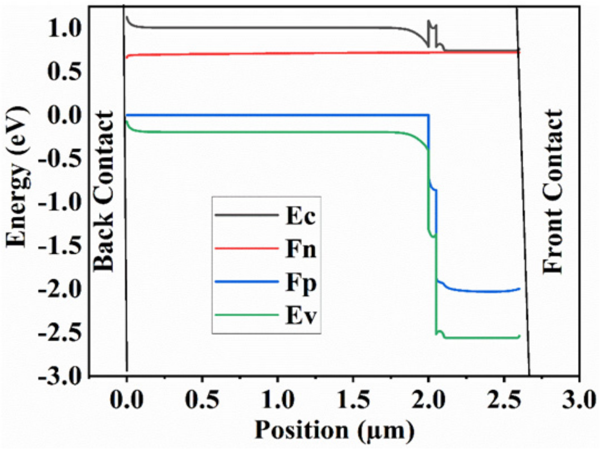

Fig. 4. Illustrating the alignment of energy levels across different layers.

the solar cell's efficiency. Key photovoltaic parameters, including short-circuit current density (J_{sc}), open-circuit voltage (V_{oc}), fill factor (FF), and power conversion efficiency (PCE) were evaluated as shown in Figure 5. Notably, J_{sc}, V_{oc}, and FF all improved with increasing absorber thickness, leading to higher overall efficiency. For example, J_{sc} increased from 35.93 mA/cm² to 36.1425 mA/cm² as the thickness rose from 2.0 to 4.0 µm, resulting in a corresponding efficiency improvement from 20.98% to 21.47%. This enhancement is largely due to improved photon absorption, especially for longer wavelengths, as the absorber layer becomes thicker [31]. Additionally, as seen in Figure 6(a), back contact recombination significantly decreases with greater absorber thickness, further boosting efficiency. Thicker absorber layers also increase the carrier diffusion length, which minimizes electron-hole pair losses at the rear contact and

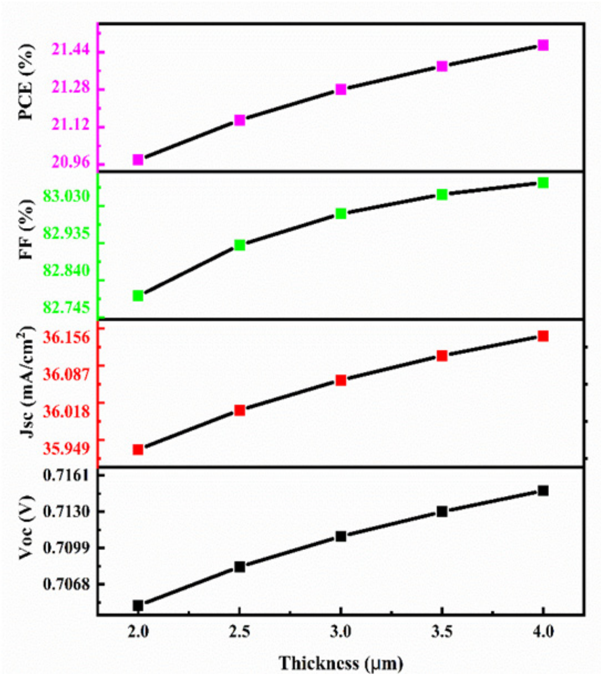

Fig. 5. Impact of absorber layer thickness on solar cell parameters such as V_{oc}, J_{sc}, FF (%), and PCE (%).

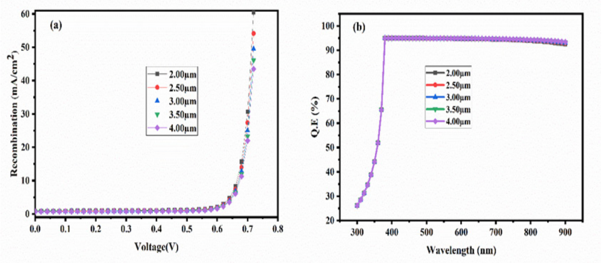

Fig. 6. (a) Recombination rate and (b) Quantum efficiency with varying absorber layer thickness.

contributes to better conversion efficiency [32]. However, extremely thin layers can exhibit quantum confinement effects, potentially altering the spectral response and introducing discrete energy levels [33]. Based on these findings, an absorber thickness of approximately 4.0 μm is considered optimal. Further increases in thickness offer minimal efficiency gains while requiring more material, making them less practical. Figure 6(b) illustrates how quantum efficiency (Q.E.) varies with absorber layer thickness.

3.3. Impact of Absorber Layer Acceptor Density

Our investigation analyzed the impact of acceptor density (N_A) on the performance of a p-type semiconductor material CIGS with a fixed thickness of 2 μm. The N_A concentration controlled the density of "holes" in the semiconductor material, affecting all key parameters of the solar cell [34]. We changed the majority carrier concentration within a range from 1×10^{16} to 1×10^{12} cm^{-3} and observed notable trends of different solar cell parameters in Figure 7. As the N_A changes from 1×10^{16} to 1×10^{12} cm^{-3}, the J_{sc} substantially rose from 35.93 to 36.32 mA/cm². Conversely, the V_{oc} showed an opposing behavior, decreasing from 0.705 to 0.6594 V during all the changes. Interestingly, N_A below 1×10^{15}, both V_{oc} and J_{sc} show little value changes. These findings underscore the critical role of acceptor concentration in determining device performance [35]. Notably, we observed a decline in FF and PCE when we changed the N_A values from 1×10^{16} to 1×10^{12} cm^{-3}. Careful deliberation of material suitability and reliability is essential to maintain optimal performance. There exists a trade-off between carrier concentration and recombination rates, where reduced acceptor concentration can lead to a decrease in carrier concentration, but if not properly controlled, may result in increased recombination, as shown in Figure 8. A decrease in the electrical conductivity due to reduced concentration of acceptors can impede charge separation and transport within the material, thus aiding in inefficient charge separation and transport [36]. Therefore, optimizing acceptor concentration can enhance the efficacy of thin-film solar cells by

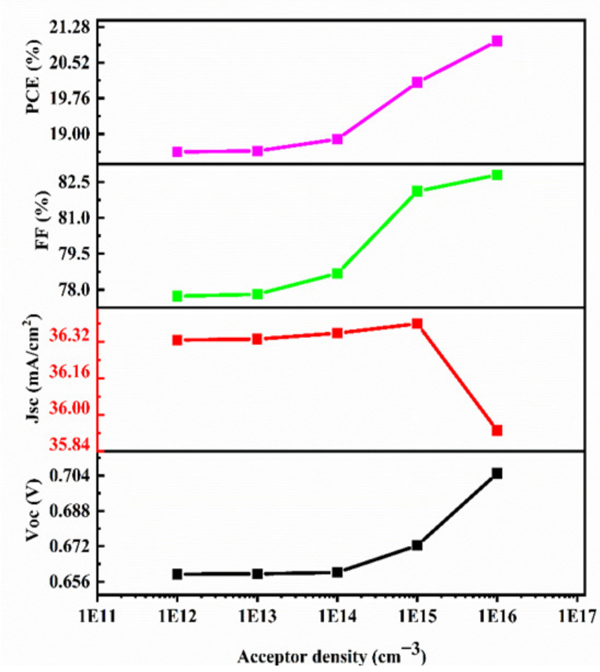

Fig. 7. Impact of acceptor density on solar cell parameters such as V_{oc}, J_{sc}, FF%, and PCE%.

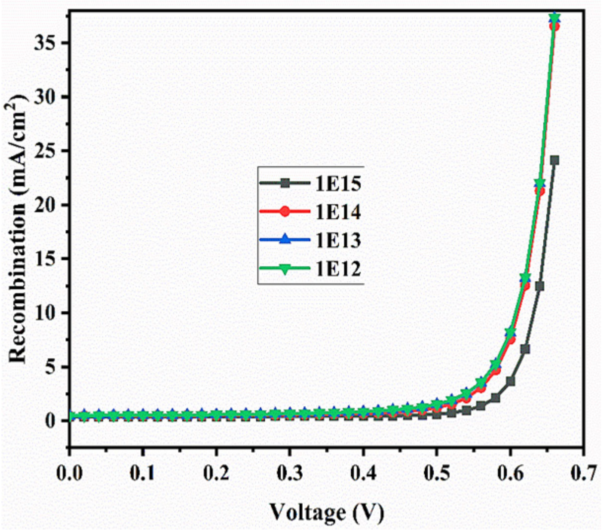

Fig. 8. Impact of accepter density on recombination rate.

dropping recombination rates of charge carriers, leading to higher overall PCE (%) and improving material stability and longevity.

3.4. Impact of Absorber Defects Density

We explored the impact of defect density (N_t) on the photovoltaic (PV) device performance. N_t is defined by the Shockley-Read-Hall recombination model by Equation (4):

$$R = \frac{np - n_i^2}{\tau_p \left(n + n_c e^{\left(E_g - E_\tau\right)/kT} \right) + \tau_p \left(p + n_v e^{\frac{(e_\tau)}{kT}} \right)} \quad (4)$$

Where, E_t shows trap energy levels, τ_p and τ_n are carrier lifetimes for holes and electrons, respectively [37]. Figure 9 illustrates the variations in essential PV parameters such as PCE (%), J_{sc}, FF, and V_{oc} with simultaneous changes in N_t. We varied N_t from 1×10^{18} to 1×10^{19} cm^{-3}, which shows that high N_t in the absorber layer is attributed to the poor quality of doping, notably in CGIS. Elevated N_t increases recombination rates due to pinhole formation, leading to reduced carrier diffusion lengths and diminished carrier collection efficiency at contacts, as shown in Figure 10. The drop in overall device performance is evident, and the increase in the N_t impacts the device's overall performance. PCE of PSCs substantially declines with increasing N_t, dropping from 20.98 to 4.23%. Similarly, FF decreases from 82.80 to 52.13%, with the same variations in N_t. J_{sc} and V_{oc} also show the same behavior as it decreases from 35.93 to 21.73 mA/cm^2 and 0.70 to 0.37 V variations with defect density values from 10^{15} cm^{-3} to 10^{19} cm^{-3}. Defect-induced impurities in the CIGS thickness or composition can lead to uneven light absorption across the solar cell's surface, ultimately reducing its overall PCE [38]. Because the defects can act as limiting factors, preventing the solar cell from achieving its maximum efficiency potential as described by the Shockley-Queisser limit [39]. The extent of these limitations depends on the type and

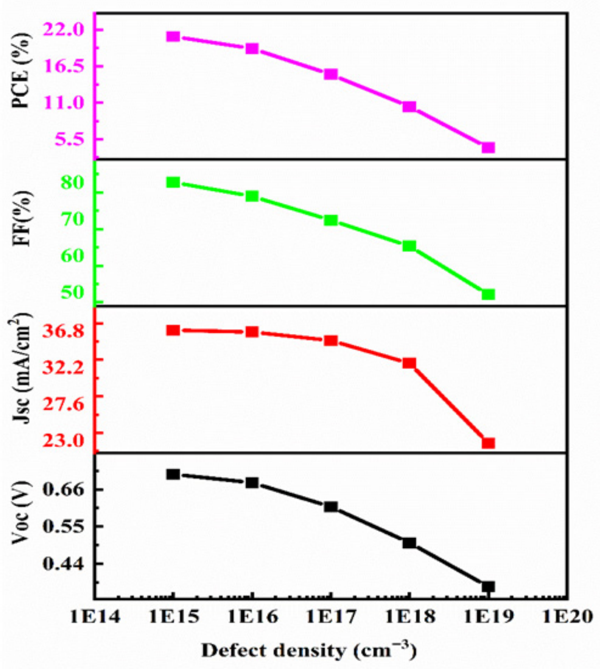

Fig. 9. Impact of absorber (N_t) on performance parameters.

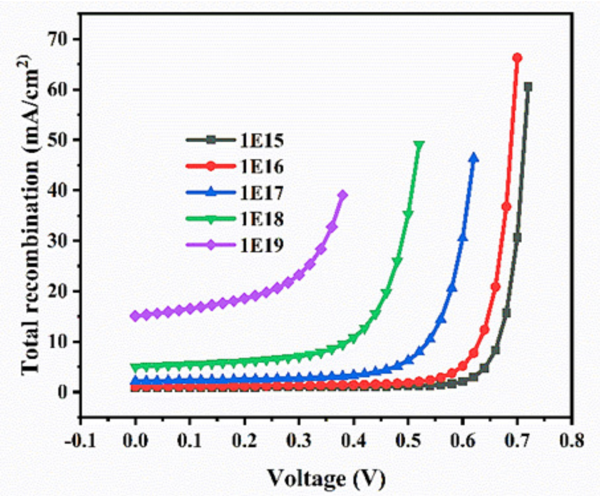

Fig. 10. Impact of absorber (N_t) on recombination rate.

density of defects present. To address these issues, researchers and engineers employ various strategies to modify the impact of defects. These approaches include interface engineering, defect passivation, and advancements in material growth techniques. By minimizing recombination and improving overall performance, these efforts aim to enhance the efficiency and effectiveness of solar cells.

3.5. Impact of Temperature

Temperature has a complex impact on the performance of thin-film solar cells, influencing parameters such as fill factor (FF), open-circuit voltage (Voc), short-circuit current density (Jsc), power conversion efficiency (PCE), and long-term durability [40]. Understanding these temperature effects is essential for optimizing the design and operation of solar cell systems, especially in environments with wide temperature variations. To explore these effects, simulations were conducted across a temperature range of 300 K to 320 K, as shown in Figure 11. This temperature range was selected to reflect realistic operating conditions while avoiding extreme scenarios that may introduce non-linear effects or material degradation beyond the scope of this study. One of the most significant temperature-related changes observed is the reduction in V_{oc} as temperature increases. This drop is attributed to the increase in intrinsic carrier concentration at elevated temperatures, which leads to higher recombination rates [41]. Due to this, fewer charge carriers reach the cell contacts, reducing the voltage output. In contrast, J_{sc} tends to show a modest increase with rising temperature. This is primarily due to improved charge carrier mobility, which enhances electrical conductivity and promotes more effective charge separation and transport. However, the slight gain in J_{sc} is typically insufficient to offset the loss in V_{oc}, ultimately resulting in a decrease in overall efficiency. Specifically, efficiency drops from 20.98% to 19.54% as temperature increases. This decline in performance is further linked to the temperature-dependent behavior of the semiconductor's bandgap. As temperature rises, the bandgap contracts, which causes the absorption spectrum to shift towards longer wavelengths. This reduces the cell's sensitivity to higher-energy photons and lowers the amount of electricity generated [42]. These findings are consistent with previous research and highlight the critical role of temperature in determining the efficiency and reliability of thin-film solar cells. Effectively understanding and mitigating temperature effects is essential for improving the performance and longevity of these devices under varying environmental conditions.

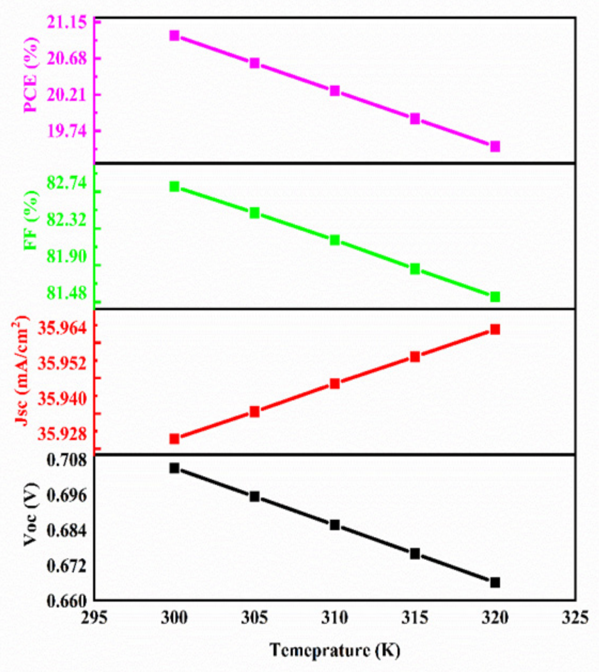

Fig. 11. Impact of temperature on solar cell parameters such as V_{oc}, J_{sc}, FF%, and PCE%.

3.6. Impact of Back Contact

The choice of back contact material (BCM) in thin-film solar cells significantly influences device performance; we used BCM such as Mo, Au, Cu, Pt, Pd, C, W, Ni, Se, and Fe [43]. Among these materials, the most widely utilized metal is molybdenum because of its efficiency and low cost, but in CIGS-based solar cells, Se BCM 1 shows superior efficiency. The performance of thin-film solar cells may be optimized by varying the work function value of the BCM. Simulation results, as depicted in Figure 12, illustrate a noticeable improvement in overall yield with changes in the BCM. This enhancement is attributed to the decline of recombination rates at the interface of BCM. When metal work function (MWF) increases the barrier height decreases, transforming the interface from Schottky to ohmic type [44]. Compared to molybdenum, an ohmic interface with an MWF of 5.9 eV facilitates improved charge carrier transport and extraction. The work function of the BCM directly impacts the energy barrier for charge

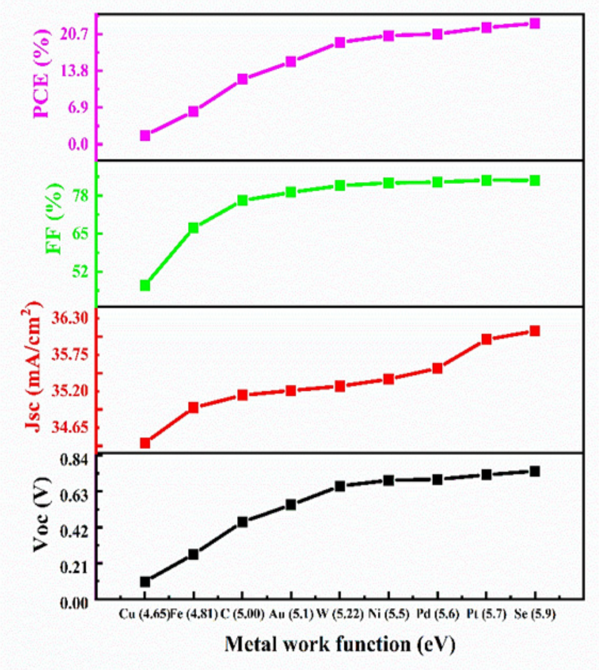

Fig. 12. Impact of back-metal work function on solar cell parameters.

carriers, inducing their ease of transportation and extraction. A suitable determined back contact MWF can boost charge carrier, increasing J_{sc} and 5.9 eV WF, showing this improvement in J_{sc} value from 35.93 to 36.40 mA/cm^2. Moreover, a suitable WF between the BCM and the semiconductor can minimize losses due to interface rejoining, resulting in a higher V_{oc}. A closely aligned work function is important in minimizing resistive losses and enhancing the movement of charge carriers within the solar cell [45]. Consequently, this alignment can result in a higher fill factor (FF) and increased power output. Careful selection of the metal used can optimize the FF(%), V_{oc}, and J_{sc}, mutually leading to enhanced inclusive PCE. Notably, efficiency has risen from 1.68 to 22.69% as the MWF ranges from 4.65 to 5.9 eV.

3.7. Impact of Cadmium-Free Buffer Layer

Cadmium-free photovoltaic cell structure and simulations offer an advanced and ecologically friendly method of utilizing solar energy [46]. In the present study, we substitute the Cds buffer layer with ZnSe, In_2S_3, and SnS_2 to improve thin-film photovoltaic modules' efficiency by using CIGS as an absorber material and the parameters outlined in Table.3 simulations were conducted, and results are depicted in Figure 13, with a summary of photovoltaic parameters in Table 5. Notably, the V_{oc} remains consistent across all buffer layers within the range of 0.7048 to 0.7050 V. However, J_{sc} shows a few variations with ZnSe, SnS_2, and In_2S_3 buffer layers approximately to 35.931, 35.92, and 35.959 mA/cm^2, respectively, because the In_2S_3 buffer layer has a wider bandgap, allowing more photons to reach the absorber, and offers better band alignment, reducing recombination losses and enhancing charge carrier collection. Fill factor analysis revealed SnS_2 exhibiting the highest value at 83.04%, while ZnSe displayed fill factors of 82.80, closely followed by CdS at 82.80%, and In_2S_3 showed an 83.00% value. CdS exhibited efficiency at 20.98%, ZnSe at 20.98%, In_2S_3 at 21.04%, and SnS_2 at 21.02%. These results indicate that cadmium-free buffer layers, specifically SnS_2 and $In2S_3$, perform comparably with CdS-based layers regarding fill factor. Whereas In_2S_3 still holds an efficiency advantage over CDs, alternatives demonstrate comparable high voltage, competitive fill factors, and J_{sc} values. The performance of ZnSe, In_2S_3, and SnS_2 as buffer layers compared to CdS can be attributed to their bandgaps, lattice matching, interface properties, and electronic characteristics, which collectively influence their effectiveness in enhancing the performance of thin-film solar cells. This is important for applications where environmental or toxicity concerns are a

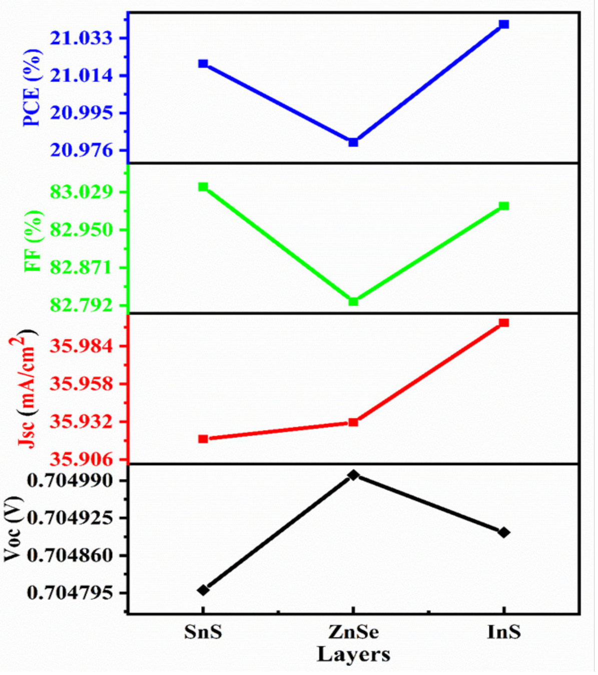

Fig. 13. Impact of different buffer layers on the cell's performance.

Table 5. Different buffer layers' impact performance.

S. No.	Buffer layer	V_{oc} (V)	J_{sc} (mA/cm^2)	FF (%)	PCE (%)
1	CdS	0.705	35.93141	82.8	20.98
2	ZnSe	0.705	35.93147	82.8	20.98
3	SnS_2	0.7048	35.92011	83.04	21.02
4	In_2S_3	0.7049	35.959757	83	21.04

priority. These alternatives show promise, offering similar or even better performance while avoiding toxic cadmium [47]. Figure 14 shows the impact of the buffer layer on Q.E%.

3.8. Impact of Different HTLs

To mitigate the limitations associated with expensive metals such as Se and Pt, a different layer referred to as the HTL is introduced between the absorber layer and the back contact. The HTL, typically a heavily doped p-type layer, serves to moderate the coalescing of minority carriers at the back contact [48, 49]. It is important to ensure the appropriate alignment of energy levels between the HTL material and the valence band of the absorber layer to facilitate effective hole removal. This alignment decreases the energy barrier for the whole movement, thus aiding in their movement across the interface HTL and absorber. Furthermore, factors such as refractive index and transparency are crucial considerations for the HTL. Transparency of the HTL permits incident light to enter and grasp the CIGS layer, while an optimal refractive index assists in minimizing optical losses and enhancing light trapping. Hence, HTL materials with a bandgap energy exceeding that of the absorber material are typically selected. For instance, in the present investigation, CuI and Spiro-MeOTAD were employed as HTL to evaluate their impact on the efficiency, and their bandgap values are 3.1 eV and 3.0 eV, respectively.

When employing HTL materials in thin-film solar cells to assess their impact on performance, observed changes in FF, PCE, J_{sc}, and V_{oc} can be attributed to several factors, and their J-V curve is presented in Figure 15. The decrease in FF and PCE from 82.8 to 71.63% and 20.98 to 19.32%, respectively, may result from increased resistive losses within the device or poor charge carrier collection efficiency due to inferior interface properties between the HTL and the absorber layer. Conversely, the increase in J_{sc} and V_{oc} from 35.93 to 36.20 mA/cm^2 and 0.705 to 0.7451 V, respectively, suggests improved charge carrier generation and extraction, possibly due to better alignment of energy levels between the absorber layer and HTL, leading to reduced energy barriers for carrier transport and enhanced device performance. These

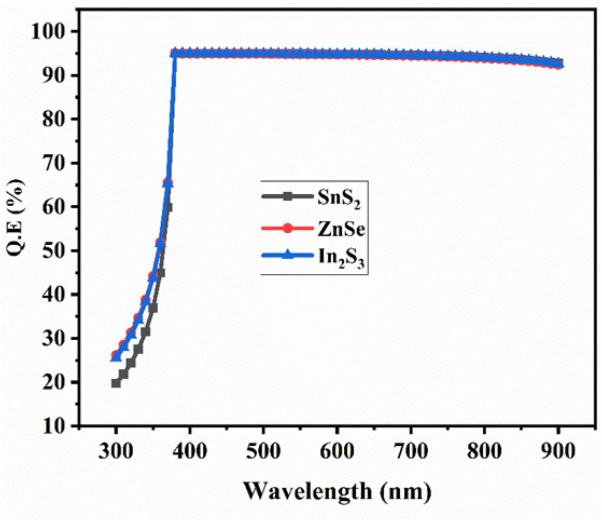

Fig. 14. Buffer layer impact on Q.E%.

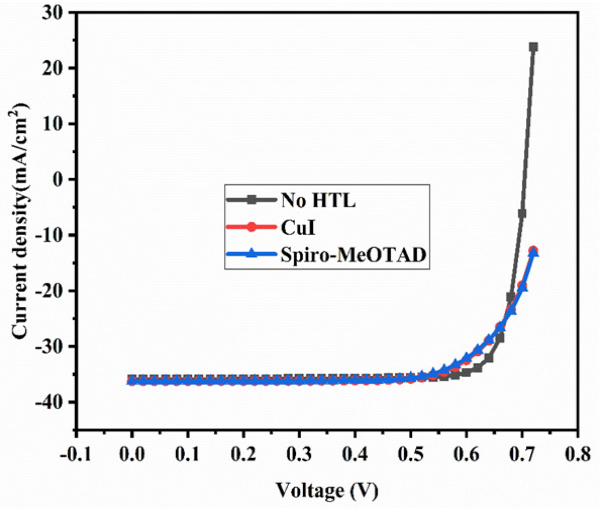

Fig. 15. Impact of different HTL on J-V curve.

outcomes underscore the intricate interplay between material properties, interface characteristics, and device architecture in determining the efficiency of thin-film solar cells employing CuI and Spiro-MeOTAD as HTL materials. Table 6 provides a summary of photovoltaic parameters for all cases. Therefore, precisely designed HTL layers are pivotal in optimizing thin-film solar cells' efficiency and dependability, making them a promising technology for sustainable energy production [50, 51].

Table 6. Performance comparisons between with and without HTL.

S. No.	Structure	V_{oc} (V)	J_{sc} (mA/cm^2)	FF (%)	PCE (%)
1	Without-HTL	0.705	35.93141	82.8	20.98
2	CuI	0.7451	36.20737	72.36	19.52
3	Spiro	0.7451	36.206	71.63	19.32

3.9. Simulation Optimization

In optimizing the solar cell structure, extensive analyses were performed on several key parameters to enhance its performance. Among these factors, the thickness of the absorber material and the work function of the metal, for instance, selenium (5.9 eV), are of significant importance. By carefully adjusting the thickness of the absorber layer, which in this case was 4.0 micrometers, significant improvements in the cell's efficacy and overall performance were achieved. These efforts have achieved a remarkable efficiency of 22.23% from 20.98% and show the importance of precise engineering at the material and structural levels, showcasing how targeted adjustments in these specific parameters can lead to substantial enhancements in solar cell efficiency. This optimization strategy emphasizes enhancing the solar cell's energy conversion efficiency while reducing material consumption and expenses. This ultimately aids in the progression of sustainable energy technologies.

4. CONCLUSIONS

This research has provided valuable insights into critical factors that influence solar cell efficiency based on CIGS technology. The study has underscored the intricate interplay of these variables in determining cell performance by systematically investigating the impact of absorber layer thickness, carrier concentration, buffer layers, HTLs, and back contact parameters. The optimization of absorber thickness demonstrated a crucial role in enhancing light absorption efficiency and charge carrier mobility while fine-tuning carrier concentration balanced carrier movement and recombination to achieve optimal performance. The work function of back contact metal was identified as a significant determinant of photovoltaic parameters, while temperature control strategies were highlighted as essential for reliable, highly efficient performance. The significant role of HTLs in mitigating recombination losses and enhancing charge collection was explored, with notable efficiency reductions observed when substituting CdS with alternative HTLs such as CuI (19.52%) and Spiro-MeOTAD (19.32%). A promising pathway toward environmentally friendly solar cells was emphasized by using In_2S_3 as a cadmium-free buffer layer, achieving an impressive efficiency of 22.23% after optimization. These findings reinforce the potential of CIGS technology as a cost-effective and sustainable energy solution capable of addressing the growing demand for renewable energy sources. The study highlights the importance of careful design and parameter optimization and lays a strong foundation for future advancement in CIGS-based solar cells. Continued research in developing cadmium-free designs and refining fabrication techniques will be instrumental in overcoming the remaining challenges. These efforts promise to improve further the efficiency, scalability, and environmental sustainability of CIGS solar cells, thus advancing the global transition toward cleaner and more reliable energy systems.

5. CONFLICT OF INTEREST

The authors have no conflict of interest to disclose.

6. REFERENCES

1. F. Qin, Y. Zhang, K. Naseem, Z. Chen, G. Suo, W. Hayat, and S.H.S. Gardezi. Assessment of the importance and catalytic role of chromium oxide and chromium carbide for hydrogen generation via hydrolysis of magnesium. *Nanoscale* 16(41): 19518-19528 (2024).
2. F. Qin, K. Naseem, Z. Chen, G. Suo, and A. Tahir. Carbon nano-tube coated with iron carbide catalysis for hydrolysis of magnesium to generate hydrogen. *International Journal of Hydrogen Energy* 83:

1359-1369 (2024).

3. K. Naseem, H. Zhong, W. Jiang, M. Liu, C. Lang, K. Chen, L. Ouyang, and J. Huang. A reusable dual functional Mo_2C catalyst for rapid hydrogen evolution by Mg hydrolysis. *Journal of Materials Chemistry A* 11(36): 19328-19337 (2023).
4. E. Kabir, P. Kumar, S. Kumar, A.A. Adelodun, and K.-H. Kim. Solar energy: Potential and future prospects. Renewable and Sustainable. *Energy Reviews* 82: 894-900 (2018).
5. S. Moujoud, B. Hartiti, S. Touhtouh, F. Belhora, and A. Hajjaji. Optimizing Sb_2Se_3 thin-film solar cells: A comprehensive simulation study of multiple influential factors. *Optik* 303: 171723 (2024).
6. O.J. Olujobi, U.E. Okorie, E.S. Olarinde, and A.D. Aina-Pelemo. Legal responses to energy security and sustainability in Nigeria's power sector amidst fossil fuel disruptions and low carbon energy transition. *Heliyon* 9: e17912 (2023).
7. A.A. Hussien, A.A. Salem, S.W. Sharshir, and T. Nabil. Performance Assessment of an Automated Hybrid Solar Desalination System Powered by Solar PV and Wind Turbine: Experimental Investigation. *SSRN 4766771* (2024). https://papers.ssrn.com/sol3/papers.cfm?abstract_id=4766771
8. Y. Kim, M. Shin, M. Lee, and Y. Kang. Hot-spot generation model using electrical and thermal equivalent circuits for a copper indium gallium selenide photovoltaic module. *Solar Energy* 216: 377-385 (2021).
9. S.R. Fatemi Shariat Panahi, A. Abbasi, V. Ghods, and M. Amirahmadi. Analysis and improvement of CIGS solar cell efficiency using multiple absorber substances simultaneously. *Journal of Materials Science*: *Materials in Electronics* 31: 11527-11537 (2020).
10. L. Lin and N.M. Ravindra. CIGS and perovskite solar cells–an overview. *Emerging Materials Research* 9: 812-824 (2020).
11. H.I. Abdalmageed, M. Fedawy, and M.H. Aly. Effect of absorber layer bandgap of CIGS-based solar cell with (CdS/ZnS) buffer layer. *Journal of Physics: Conference Series* 2128: 012009 (2021).
12. M. Islam, T. Ahmed, S.U.D. Shamim, A.A. Piya, and A. Basak. Thickness dependent numerical investigations of lead-free perovskite/CIGS bilayer solar cell using SCAPS-1D. *Chemistry of Inorganic Materials* 2: 100034 (2024).
13. A.N. Das, P.K. Paul, M.H. Jewel, A.A. Mamun, K.H. Akhand, and S.A. Chowdhury. Analytical Modeling and Performance analysis of Copper-Indium-Gallium-Di Selenide-Based (CIGS) Solar Cell by SCAPS-1D. *7th International Conference on Development in Renewable Energy Technology (ICDRET)* pp. 1-6 (2024).
14. B.F. Gonçalves, S. Sadewasser, L.M. Salonen, S. Lanceros-Méndez, and Y.V. Kolen'ko. Merging solution processing and printing for sustainable fabrication of Cu (In, Ga) Se_2 photovoltaics. *Chemical Engineering Journal* 442: 136188 (2022).
15. M. Burgelman, K. Decock, S. Khelifi, and A. Abass. Advanced electrical simulation of thin film solar cells. *Thin Solid Films* 535: 296-301 (2013).
16. M.F. Hossain, A. Ghosh, M.A.A. Mamun, A.A. Miazee, H. Al-lohedan, R.J. Ramalingam, M.F. Islam Buian, S.R.I. Karim, M.Y. Ali, and M. Sundararajan. Design and simulation numerically with performance enhancement of extremely efficient Sb_2Se_3-Based solar cell with V_2O_5 as the hole transport layer, using SCAPS-1D simulation program. *Optics Communications* 559: 130410 (2024).
17. E. Danladi, P.M. Gyuk, N.N. Tasie, A.C. Egbugha, D. Behera, I. Hossain, I.M. Bagudo, M.L. Madugu, and J.T. Ikyumbur. Impact of hole transport material on perovskite solar cells with different metal electrode: a SCAPS-1D simulation insight. *Heliyon* 9: e14326 (2023).
18. M.Z. Muzakkar, N.A. Busri, A.A. Umar, L.O.A. Salim, M. Maulidiyah, and M. Nurdin. Enhanced Performance of Perovskite Solar Cells with Tungsten-Doped SnO_2 as an Electron Transport Material. *Journal of Inorganic and Organometallic Polymers and Materials* 35: 1475-1483 (2025).
19. A.R. Smith, M. Ghamari, S. Velusamy, and S. Sundaram. Thin-Film Technologies for Sustainable Building-Integrated Photovoltaics. *Energies* 17(24): 6363 (2024).
20. C.J. Petti, M.M. Hilali, and G. Prabhu. Thin Films in Photovoltaics. In: Handbook of Thin Film Deposition: Techniques, Processes, and Technologies. K. Seshan (Ed.). *Elsevier* pp. 313-359 (2012).
21. A. ul Rehman, T. Munir, S. Afzal, M. Saleem, and I.L. Ikhioya. Enhanced Solar Cell Efficiency with Tin-Based Lead-Free Material (FASnI3) through SCAPS-1D Modeling. *Eurasian Journal of Science and Technology* 4: 258-263 (2024).
22. N. Khoshsirat, N.A.M Yunus, M.N. Hamidon, S. Shafie, and N. Amin. Analysis of absorber and buffer layer band gap grading on CIGS thin film solar cell performance using SCAPS. *Pertanika Journal of Science and Technology* 23(2): 241-250 (2015).
23. M.K. Hossain, M.K.A. Mohammed, R. Pandey,

A.A. Arnab, M.H.K. Rubel, K.M. Hossain, M.H. Ali, M.F. Rahman, H. Bencherif, J.V. Madan, M.R. Islam, D.P. Samajdar, and S. Bhattarai. Numerical analysis in DFT and SCAPS-1D on the influence of different charge transport layers of CsPbBr3 perovskite solar cells. *Energy & Fuels* 37: 6078–6098 (2023).

24. A.K. Chaudhary, S. Verma, and R.K. Chauhan. Thermal and power performance optimization of cost-effective solar cells using eco-friendly perovskite materials. *Physica Scripta* 99: 025512 (2024).
25. Z. Qiu, Y. Li, X. Long, H. Tian, Y. Pu, B. Lv, J. Wei, Q. Dai, and W. Wang. Built-in electric field induced efficient interfacial charge separation via the intimate interface of CdS-based all-sulfide binary heterojunction for enhanced photoelectrochemical performance. *Journal of Alloys and Compounds* 976: 173188 (2024).
26. M.F. Rahman, M. Chowdhury, L. Marasamy, M.K.A. Mohammed, M.D. Haque, S.R.A. Ahmed, A. Irfan, A.R. Chaudhry, and S. Goumri-Said. Improving the Efficiency of a CIGS Solar Cell to Above 31% with Sb_2S_3 as a New BSF: A Numerical Simulation Approach by SCAPS-1D. *RSC Advances* 14(3): 1924-1938 (2024).
27. S.H. Zyoud, A.H. Zyoud, N.M. Ahmed, and A.F.I. Abdelkader. Numerical modelling analysis for carrier concentration level optimization of CdTe heterojunction thin film–based solar cell with different non–toxic metal chalcogenide buffer layers replacements: using SCAPS–1D software. *Crystals* 11: 1454 (2021).
28. T.D. Lee and A.U. Ebong. A review of thin film solar cell technologies and challenges. *Renewable and Sustainable Energy Reviews* 70: 1286-1297 (2017).
29. F. Elhady, T.M. Abdolkader, and M. Fedawy. Simulation of new thin film Zn (O, S)/CIGS solar cell with bandgap grading. *Engineering Research Express* 5: 025027 (2023).
30. M.K. Hossain, G.F.I. Toki, I. Alam, R. Pandey, D.P. Samajdar, M.F. Rahman, M.R. Islam, M.H.K. Rubel, H. Bencherif, J. Madan, and M.K.A. Mohammad Numerical simulation and optimization of a $CsPbI_3$-based perovskite solar cell to enhance the power conversion efficiency. *New Journal of Chemistry* 47: 4801-4817 (2023).
31. A.K. Ogundele and G.T. Mola. Semiconductor quantum dots as a mechanism to enhance charge transfer processes in polymer solar cells. *Chemosphere* 345: 140453 (2023).
32. I. Chabri, Y. Benhouria, A. Oubelkacem, A. Kaiba, I. Essaoudi, and A. Ainane. SCAPS device simulation study of formamidinium Tin-Based perovskite solar cells: Investigating the influence of absorber parameters and transport layers on device performance. *Solar Energy* 262: 111846 (2023).
33. N.A.Z. Abidin, F. Arith, N.S. Noorasid, H. Sarkawi, A.N. Mustafa, N.E. Safie, A.S. Mohd Shah, M.A. Azam, P. Chelvanathan, and N. Amin. Dopant engineering for ZnO electron transport layer towards efficient perovskite solar cells. *RSC Advances* 13: 33797-33819 (2023).
34. K. Liang, L. Huang, T. Wang, C. Wang, Y. Guo, Y. Yue, X. Liu, J. Zhang, Z. Hu, and Y. Zhu. Rational design of formamidine tin-based perovskite solar cell with 30% potential efficiency via 1-D device simulation. *Physical Chemistry Chemical Physics* 25: 9413-9427 (2023).
35. K.D. Jayan. Design and Comparative Performance Analysis of High-Efficiency Lead-Based and Lead-Free Perovskite Solar Cells. *Physica Status Solidi (a)* 219: 2100606 (2022).
36. Y. Ming, H. Wang, W. Cai, and Z. Zang. Mixed-Halide Inorganic Perovskite Solar Cells: Opportunities and Challenges. *Advanced Optical Materials* 11: 2301052 (2023).
37. M. Jihyun, Y. Choi, D. Kim, and T. Park. Beyond Imperfections: Exploring Defects for Breakthroughs in Perovskite Solar Cell Research. *Advanced Energy Materials* 14: 2302659 (2024).
38. A. Rehman, S. Afzal, I. Naeem, D. Bibi, S.G. Sarwar, F. Nabeel, and R.M. Obodo. Performance Optimization of $FASnI_3$ Based Perovskite Solar Cell Through SCAPS-1D Simulation. *Hybrid Advances* 7: 100301 (2024).
39. L.C. Ghosekar and G.C. Patil. Performance analysis and thermal reliability study of multilayer organic solar cells. *IEEE Transactions on Device and Materials Reliability* 19: 572-580 (2019).
40. S. Priyanka and N.M. Ravindra. Temperature dependence of solar cell performance - an analysis. *Solar Energy Materials and Solar Cells* 101: 36-45 (2012).
41. R.L. Milot, G.E. Eperon, H.J. Snaith, M.B. Johnston, and L.M. Herz. Temperature-dependent charge-carrier dynamics in $CH_3NH_3PbI_3$ perovskite thin films. *Advanced Functional Materials* 25: 6218-6227 (2015).
42. J.K. Deepthi and V. Sebastian. Comprehensive device modelling and performance analysis of $MASnI_3$ based perovskite solar cells with diverse ETM, HTM and back metal contacts. *Solar Energy* 217: 40-48 (2021).

43. A. Rehman, M. Iqbal, D. Bibi, F. Muneer, S. Afzal, T. Munir, and M. Bilal. Optimization of Lead-Free Inorganic Perovskite Solar Cells: SCAPS Numerical Simulation Study on $(FA)_2BiCuI_6$ Absorber Layer. *Eurasian Journal of Science and Technology* 4(4): 340-354 (2024).
44. D. Wang, J. Sheng, S. Wu, J. Zhu, S. Chen, P. Gao, and J. Ye. Tuning back contact property via artificial interface dipoles in Si/organic hybrid solar cells. *Applied Physics Letters* 109(4): 043901 (2016).
45. M. Bivour, J. Temmler, F. Zähringer, S. Glunz, and M. Hermle. High work function metal oxides for the hole contact of silicon solar cells. *IEEE 43rd Photovoltaic Specialists Conference (PVSC), Portland, OR, USA* pp. 0215-0220 (2016).
46. T. Ibn-Mohammed, S.C.L. Koh, I.M. Reaney, A. Acquaye, G. Schileo, K.B. Mustapha, and R. Greenough. Perovskite solar cells: An integrated hybrid lifecycle assessment and review in comparison with other photovoltaic technologies. *Renewable and Sustainable Energy Reviews* 80: 1321-1344 (2017).
47. K. Vijayan, S.P. Vijayachamundeeswari, K. Sivaperuman, N. Ahsan, T. Logu, and Y. Okada. A review on advancements, challenges, and prospective of copper and non-copper based thin-film solar cells using facile spray pyrolysis technique. *Solar Energy* 234: 81-102 (2022).
48. F.S. Ahmadpanah, A.A. Orouji, and I. Gharibshahian. Improving the efficiency of CIGS solar cells using an optimized p-type CZTSSe electron reflector layer. *Journal of Materials Science: Materials in Electronics* 32(17): 22535-22547 (2021).
49. I. Gharibshahian, A.A. Orouji, and S. Sharbati. Effectiveness of band discontinuities between CIGS absorber and copper-based hole transport layer in limiting recombination at the back contact. *Materials Today Communications* 33: 104220 (2022).
50. P. Chelvanathan, M.I. Hossain, and N. Amin. Performance analysis of copper–indium–gallium–diselenide (CIGS) solar cells with various buffer layers by SCAPS. *Current Applied Physics* 10(3): S387-S391 (2010).
51. M. Islam, T. Ahmed, S.U.D. Shamim, A.A. Piya, and A. Basak. Thickness dependent numerical investigations of lead-free perovskite/CIGS bilayer solar cell using SCAPS-1D. *Chemistry of Inorganic Materials 2*: 100034 (2024).

Instructions For Authors

Manuscript Writing

The manuscript may contain a Title, Abstract, Keywords, INTRODUCTION, MATERIALS AND METHODS, RESULTS, DISCUSSION (or RESULTS AND DISCUSSION), CONCLUSIONS, ETHICAL STATEMENT (if applicable), ACKNOWLEDGEMENTS, CONFLICT OF INTEREST and REFERENCES, *and any other information that the author(s) may consider necessary*.

Title (Bold and font size 16): The title should be expressive, concise, and informative to the entire readership of the journal. It may include common terms, to make it more identifiable when people search online. Please avoid the use of long pervasive terms and non-standard or obscure abbreviations, acronyms, or symbols.

Abstract (font size 10, max 250 words)**:** Must be self-explanatory**,** stating the rationale, objective(s), methodology, main results, and conclusions of the study. Abbreviations, if used, must be defined on the first mention in the Abstract as well as in the main text. Abstracts of review articles may have a variable format.

Keywords (font size 10)**:** Provide five to eight keywords consisting of words and phrases that are closely associated with the topic depicting the article.

INTRODUCTION (font size 11)**:** Provide a clear and concise statement of the problem, citing relevant recent literature, and objectives of the investigation. Cite references in the text by number in square brackets**,** the reference must be cited in a proper English sentence [1]. or "... as previously described [3, 6–8]". For a single author: Bednorz [2] investigated the environmental pollution ... When there are only two authors: Bednorz and Allan [2] investigated the environmental pollution ... and for three or more authors: Bednorz *et al.* [2] investigated the environmental pollution ..; and list them in the REFERENCES section, in the order of citation in the text.

MATERIALS AND METHODS (font size 11)**:** Provide an adequate account of the procedures or experimental details, including statistical tests (if any), concisely but sufficiently enough to replicate the study. Relevant references to methodology must be cited.

RESULTS (font size 11)**:** Be clear and concise with the help of appropriate Tables, Figures, and other illustrations. Data should not be repeated in Tables and Figures but must be supported with statistics. The data presented in Tables and Figures must be elaborated in the main text.

DISCUSSION (font size 11)**:** Provide interpretation of the RESULTS in the light of previous relevant studies, citing published references.

CONCLUSIONS (font size 11)**:** Briefly state the implication of your study findings, and carefully address the study questions. Confine your conclusions according to the objectives of your study and the aspects covered in the abstract. Discuss both positive and negative findings.

ETHICAL STATEMENT (font size 10)**:** The statement of ethical approval by an appropriate ethics committee or review board must be included in the manuscript (if applicable), as per the Journal's policy.

ACKNOWLEDGEMENTS: (font size 10)**:** In a brief statement, acknowledge the financial support and other assistance.

CONFLICT OF INTEREST (font size 10)**:** State if there is any conflict of interest.

REFERENCES (font size 10)**:** References must be listed in numerical order as listed in the main text. Only published (and accepted for publication) journal articles, books and book chapters, conference proceedings, online reports, a degree thesis, and materials available on the website qualify for REFERENCES.

Declaration: Provide a declaration that: (i) the results are original, (ii) the same material is neither published nor under consideration for publication elsewhere, (iii) approval of all authors has been obtained, and (iv) in case the article is accepted for publication, its copyright will be assigned to the *Pakistan Academy of*

Sciences. Authors must obtain permission to reproduce, where needed, copyrighted material from other sources and ensure that no copyrights are infringed upon.

Manuscript Formatting

Manuscripts must be submitted in Microsoft Word (Latest Version .doc or .docx format); pdf files are not acceptable. Figures can be submitted separately in TIFF, GIF, JPEG, EPS, or PPT. Manuscripts, in *Times New Roman*, 1.15 spaced (but use single-space for Tables, long headings, and long captions of tables and figures). The Manuscript sections must be numbered, i.e., **1. INTRODUCTION, 2. MATERIALS AND METHODS,** and so on… (a) **Title** of the article **(**Capitalize the initial letter of each main word, font-size 16, **bold**), max 160 characters (no abbreviations or acronyms), depicting article's contents; (b) Author's complete name (font size 12, **bold**), and professional affiliation (i.e., each author's Department, Institution, Mailing address, and Email and Contact number, but no position titles) (font size 12); (c) Indicate the corresponding author with *; and (d) **Short running title**, max 50 characters (font size 10).

Headings and Subheadings (font size 11): All flush left

LEVEL-1: **ALL CAPITAL LETTERS; Bold**

Level-2: **Capitalize Each First Letter (**Except prepositions**); Bold**

Level-3: Capitalize the first letter only (Sentence case)***; Bold, Italic***

Level-4: *Run-in head*; *Italics*, *in the normal paragraph position. Capitalize the first letter only and end in a colon (i.e.,* ***:****)*

A list of REFERENCES must be prepared as under:

a. Journal Articles *(Name of journals must be stated in full)*

1. J. Rashid, A. Ahsan, M. Xu, I. Savina, and F. Rehman. Synthesis of cerium oxide embedded perovskite type bismuth ferrite nanocomposites for sonophotocatalysis of aqueous micropollutant ibuprofen. *RSC Advances* 13(4): 2574-2586 (2023).
2. A. Fayyaz, N. Ali, Z.A. Umar, H. Asghar, M. Waqas, R. Ahmed, R. Ali, and M.A. Baig. CF-LIBS based elemental analysis of Saussurea simpsoniana medicinal plant: a study on roots, seeds, and leaves. *Analytical Sciences* 40(3): 413-427 (2024).
3. W. Bialek and S. Setayeshgar. Cooperative sensitivity and noise in biochemical signaling. *Physical Review Letters* 100: 258–263 (2008).

b. Books

4. W.R. Luellen (Ed.). Fine-Tuning Your Writing. *Wise Owl Publishing Company, Madison, WI, USA* (2001).
5. U. Alon and D.N. Wegner (Eds.). An Introduction to Systems Biology: Design Principles of Biological Circuits. *Chapman & Hall/CRC, Boca Raton, FL, USA* (2006).

c. Book Chapters

6. M.S. Sarnthein, J.E. Smolen, and J.D. Stanford. Basal sauropodomorpha: historical and recent phylogenetic developments. In: The Northern North Atlantic: A Changing Environment. P.R. Schafer and W. Schluter (Eds.). *Springer, Berlin, Germany* pp. 365–410 (2000).
7. S. Brown and L.A. Boxer. Functions of Europhiles. In: Hematology, (4th ed). W.J. Williams, E. Butler, and M.A. Litchman (Eds.). *McGraw Hill, New York, USA* pp. 103–110 (1991).

d. Reports

8. M.D. Sobsey and F.K. Pfaender. Evaluation of the H$_2$S method for Detection of Fecal Contamination of

Drinking Water. Report No.-WHO/SDE/WSH/02.08. *Water Sanitation and Health Programme, WHO, Geneva, Switzerland* (2002).

e. Online References

These should specify the full URL for reference, please check again to confirm that the work you are citing is still accessible:

9. UNESCO. Global Education Monitoring Report 2024/5: Leadership in education−Lead for learning. *United Nations Educational, Scientific and Cultural Organization, Paris, France* (2024). https://digitallibrary.un.org/record/4066661?ln=en&v=pdf

10. L.M. Highland and P. Bobrowsky. The landslide handbook−A guide to understanding landslides. Circular 1325. *US Geological Survey, Reston, Virginia* (2008).

    https://pubs.usgs.gov/circ/1325/pdf/C1325_508.pdf

f. Conference Proceedings

11. M. Khalid, A.B. Majid, F. Mansour, and C.R. Smith. Word Representations with Recursive Neural Networks for Morphology. *27th European Conference on Signal Processing, (2nd - 6th September 2021), Madrid, Spain* (2021).

g. A Degree Thesis

12. M. Afzal. Investigation of structural and magnetic properties of nanometallic Fe-Mn Alloys. Ph.D. Thesis. *Quaid-i-Azam University, Islamabad, Pakistan* (2023).

Tables: Insert all tables as editable text, not as images. Number tables consecutively following their appearance in the text. A concise but self-explanatory heading must be given. Tables should be numbered according to the order of citation (like **Table 1.**, **Table 2.** (font size 10)). *Do not* abbreviate the word "Table" to "Tab.". Round off data to the nearest three significant digits. Provide essential explanatory footnotes, with superscript letters or symbols keyed to the data. Do not use vertical or horizontal lines, except for separating column heads from the data and at the end of the Table.

Figures: In the main text write Figure, not Fig. Figures may be printed in two sizes: column width of 8.0 cm or page width of 16.5 cm; In the Figure caption, number them as **Fig. 1.**, **Fig. 2.** Captions to Figures must be concise but self-explanatory (font size 10). Laser-printed line drawings are acceptable. Do not use lettering smaller than 9 points or unnecessarily large. Photographs must be of high quality. A scale bar should be provided on all photomicrographs. All Figures should have sufficiently high resolution (minimum 300 dpi) to enhance the readability. Figures as separate files in JPG or TIFF format may be provided.

SUBMISSION CHECKLIST

The following list will be useful during the final checking of an article before submission to the journal.

1. Manuscript in MS Word format
2. Cover Letter
3. Novelty Statement
4. Copyright Form
5. Figures in JPG or TIFF format

In case of any difficulty while submitting your manuscript, please get in touch with:

Editor-in-Chief

Pakistan Academy of Sciences
3-Constitution Avenue,
G-5/2, Islamabad, Pakistan
Email: editor@paspk.org
Tel: +92-51-920 7140
Websites: http://www.paspk.org/proceedings/; http://ppaspk.org/

PROCEEDINGS OF THE
PAKISTAN ACADEMY OF SCIENCES: PART A
Physical and Computational Sciences

CONTENTS

Volume 62, No. 1, March 2025

Page

Research Articles

Websites: http://www.paspk.org/proceedings/; http://ppaspk.org

PAKISTAN ACADEMY OF SCIENCES, ISLAMABAD, PAKISTAN

HEC Recognized; Scopus Indexed